Dynamic Inverse Problem Solution Considering Non-Homogeneous Source Distribution with Frequency-Spatio-Temporal Constraints Applied to Brain Activity Reconstruction

Pablo Andrés Muñoz Gutiérrez

Universidad Tecnológica de Pereira
Doctorado en Ingeniería - Línea Automática
Facultad de Ingeniería Eléctrica, Electrónica, Física y Ciencias de la Computación
Pereira, Colombia
2019

Dynamic Inverse Problem Solution Considering Non-Homogeneous Source Distribution with Frequency-Spatio-Temporal Constraints Applied to Brain Activity Reconstruction

Pablo Andrés Muñoz Gutiérrez

Thesis presented as partial requirement for the degree of:
Doctor of Engineering

Advisor:
(Ph.D.) Eduardo Giraldo Suárez

Research area:
Dynamic Inverse problems
Research Group:
Automatic Control

Universidad Tecnológica de Pereira
Doctorado en Ingeniería - Línea Automática
Facultad de Ingeniería Eléctrica, Electrónica, Física y Ciencias de la Computación
Pereira, Colombia
2019

Contents

List of Figures

Introduction

The brain activity reconstruction from electroencephalographic (EEG) signals has been a research field for many years (at least 35 years [1]) and its main goal is to locate the active sources from electric scalp potentials generated by primary and secondary currents inside the brain [1, 2]. Besides, it is characterized by its high temporal resolution and its low spatial resolution.

The electroencephalography has some physical problems which do not allow perfect localization of the sources e.g. the relatively large distance between the sensors over the scalp and the current sources inside the brain, and the low conductivity on the scalp. It also has a math problem which limits the spatial resolution, it is the ill-posed nature of the inverse problem that must be solved [2–5]. Therefore, locating active current sources in the brain from EEG or EEG source localization (ESL) must solve two problems: First, it must predict of scalp potentials from current sources in the brain (forward problem) and second, it must estimate the location of the current sources from scalp potential measurements (inverse problem) [6].

The first problem is solved by adopting a quasistatic approximation to Maxwell's equations, the result is a linear map that relates the brain activity generated by active current sources with an arbitrary location and the signals measured by a set of sensors over the scalp [6–8]. The second problem is termed the *neuroelectric inverse problem* [7], it is an ill-posed and mathematically underdetermined problem because the number of unknown variables (possible active current sources) is greater than the number of known variables (sensors or electrodes) [6, 9]. This problem does not have a unique solution (might have infinite solutions), but it is possible to obtain one solution if suitable conditions are imposed, e.g. suitable probabilistic or computational constraints and temporal independence between scalp measurements and their underlying current sources [8, 10]. The first approaches were proposed over the assumption of temporal independence and the inverse problem was solved at each point of time and to be computed individually (static solution) e.g., Minimum Norm Estimates- MNE (minimizing the total power), LOw Resolution Electrical TomograAphy - LORETA (imposing spatial smoothness) and FOCus Underdetermined System Solution - FOCUSS (favoring focal estimation through spatial sparseness) [7, 8]. Static estimation is computationally convenient, but the solution to the inverse problem could be improved if this one took into account the temporal structure that can be observed in the EEG signals [8]. Considering a dynamical model as a constraint into the solution framework [11] can improve the

solution to the inverse problem too. This dynamical model can be linear and inspired by evidence from previous neurophysiology, neuroanatomy and neuroimaging studies [10] or non-linear from Dynamic Neural Fields (DNF) that incorporate corticothalamic connectivity and thalamic nonlinearity [11, 12]. Another assumption that can be made to improve the solution to the inverse problem is about sparseness, it means that the active current sources are few and scattered in comparison to the large number of potential sources [10]; in this way, in [13], authors introduce a set of time-varying spatial constraints to obtain temporal homogeneity and spatial sparsity into the solution to the inverse problem. In [14], it was used a set of sparsity constrains with appropriated spatio-temporal basis functions to get sparse solutions.

Improving the spatial resolution is the main goal in brain activity reconstruction, but it is not the only problem that must be faced. It is possible to assume that brain activity can be located in specific areas and can vary in time. Therefore, the result is spatial and temporal non-stationary activity. For this end, in [13], it was supposed that brain activity could be represented by small and smooth spatial patches varying over time [15]; then, these temporal and spatial non-stationary dynamics were included on the solution to the inverse problem to improve the accuracy of the brain activity reconstruction [13, 16]. Another way to address the non-stationary features of brain activity is using a sparse set of time-frequency basis functions (atoms) as part of the solution to the inverse problem [14].

Brain activity reconstruction from EEG signals or EEG source localization (ESL) is an open field of study, because despite its high temporal resolution and the improved spatial resolution reached by current approaches, the problem of EEG source localization can be solved with new proposals that can be focused on improving the spatial resolution through new constrains or dynamic models.

There are some open questions: The first question is about the dynamical model; the authors, in [10], used a nearest-neighbor autoregressive model and the authors, in [17], used a multivariate autoregressive (MAR) model as spatio-temporal dynamics, but both models were linear. These works opened the question about the use of non-linear models with long-range connections among sources. Despite, non-linear models were used in [11, 16] and the results were achieved in a homogeneous source space, it means that brain activity evolves over time in a spatially homogeneous way. Therefore, the second question is related with this; almost all approaches mentioned above consider that brain activity evolves over time in a spatially homogeneous way. However in [7], they quote the notion of *functional specialization* for being consistent with the spatially focal solutions. The *functional specialization* states that small regions can be restricted to specialized cortical activities according to specific stimulus attributes or experimental contexts. They introduced dynamical model parameters considering spatially non-homogeneous brain activity, but they looked at each cortical location as one current source that evolved with its dynamics. For the third question, some methods have considered time-frequency representations for tracking non-stationary activity [14] and the goal is to promote spatial sparsity, but they do not analyze the EEG signals by frequency bands. But in [18], the authors used the empirical mode decomposition

(EMD) as a previous signal processing in order to reconstruct the brain activity and they showed that it is possible to separate the signal and the noise in an adaptively way using frequency analysis. Finally, the solutions to the inverse problem based on iterative regularization methods compute the parameters of regularization through Generalized Cross-Validation (GCV) [11, 16] or L-curve [19], they have obtained good results. Another approach used to obtain these hyper-parameters has been the Akaike Bayesian Information Criterion (ABIC) [20]. Also, the methods based on free energy have been used as a cost function to reconstruct the activity of the sources [15, 21]. However, there no exist reports that consider meta-heuristics approaches which can be used to estimate these parameters e.g., evolutive algorithms.

The general question is the following: Is it possible to develop a solution for the neuroelectric inverse problem within a dynamic non-linear model that evolves in a non-homogeneous source space with spatio-temporal constrains and considering frequency bands? and can it reconstruct the brain activity improving the spatial resolution from EEG signals?

Objectives

General Objective

To propose a solution to neuroelectric inverse problem that consider a dynamic temporal evolution model within a non-homogeneous spatial structure with frequency-spatio-temporal constrains to reconstruct the brain activity

Specific Objectives

1. To set up a forward problem based on a dynamic state-space model that can render stable and unstable neural activity in order to simulate brain activity with spatially non-homogeneous zones.

2. To formulate a dynamic inverse problem considering frequency-spatio-temporal constrains and spatially non-homogeneous areas in order to reconstruct the brain activity and to analyze the temporal evolution.

3. To design an algorithm based on evolutionary processes or neural networks to estimate the regularization parameters for large-scale estimation in brain activity reconstruction.

Methodology

To achieve the proposed objectives, this work was developed through the following stages:

1. Brain activity reconstruction is linked to solve the forward problem, therefore it is necessary to know the map which relates the activity generated by an arbitrary distribution of the sources with the signals acquired by a set of sensors located over the scalp. This map and the distribution of sources allow to describe how the EEG signals evolve. Therefore, in this stage different models are analyzed, based on physiological ideas, whose temporal evolution can be represented in a spatially non-homogeneous source distribution. The spatial non-homogeneous distribution is going to be performed under stable conditions (normal EEG signals) and unstable conditions (EEG signals with some neural disorder) generated through the proposed models. Some approaches to EEG source localization will be evaluated under the proposed dynamical structure using synthetic data. These simulations will allow comparison measurements to validate the results and to analyze the proposed model.

2. To solve the neuroelectric inverse problem, different methodologies can be found in the state of the art. This work will be addressed to analyze the approaches based on state space models and regularized algorithms; specifically, those approaches where spatio-temporal constrains are used. Sparsity will be the reference point to compare the proposed method in this work, for this reason some regularized approaches are going to be tested with a l_1 norm-based spatial constraint. Furthermore, this work will take into account a frequency constraint within the solution to the inverse problem, the idea is to look for frequency selectivity as a data-driven alternative which can reflect the inherent fluctuations embedded in the EEG signals.

3. A evolutionary method was assessed to estimate the regularization parameters and improving the computational time of the Generalized Cross-Validation (GCV) method. This work was focused to estimate the hyperparameters or regularization parameters using GCV for large-scale dynamic inverse solutions. The brain activity reconstruction was compared using specifics metrics, e.g. Wasserstein metric for EEG source localization and computational time for processing speed. Additionally, This work proposed a method to choose the frequency bands to improve the EEG source localization (ESL). This method was based on standard entropy for Wavelet packed or spectral entropy for empirical mode decomposition (single and multivariate).

Contributions

The following contributions were developed during this thesis:

- A dynamical model proposed in chapter 2 and published in [22]. This model was based on physiological considerations according to [23] and normal or pathological neural activity could be simulated by using it. The dynamical model was used within the proposed forward problem and it allowed simulating brain activity whose temporal evolution was spatially non-homogeneous in different regions.

- The proposed dynamical model was used to solve the neuroelectric inverse problem with Spatio-Temporal-Frequency constraints. It is described in chapter 4 and part of the results were published in [24, 25]. The brain activity reconstruction was improved, according to the Wasserstein metric, by applying Multivariate Empirical Mode Decomposition (MEMD) as a data-driven method. Therefore, the frequency constraint is another contribution in this work by achieving the brain activity reconstruction in a selective way per frequency bands.

- The estimation of the first parameters was proposed using genetic algorithms (GA), this meta-heuristic method was proposed to modify the Generalized Cross Validation method. This modified GCV method (GCV-GA) allowed to improve the computational cost by estimating the regularization parameters, the accuracy of the results was the same (according to the Wasserstein metric). Additionally, an automatic method was proposed to choose the frequency bands to reconstruct the brain activity, an entropy cost function was used to multi-signal wavelet packed and empirical mode decomposition, and cost function based on the spectral entropy was proposed for the Multivariate Empirical Mode Decomposition. The results achieved to improve the EEG source localization in terms of the Wasserstein Metric and relative error.

Acknowledgments

This work was carried out under the funding of the Departamento Administrativo Nacional de Ciencia, Tecnología e Innovación (Colciencias). Research project: 111077757982 "Sistema de identificación de fuentes epileptogénicas basado en medidas de conectividad funcional usando registros electroencefalográficos e imágenes de resonancia magnética en pacientes con epilepsia refractaria: apoyo a la cirugía resectiva".

Chapter 1

Background

1.1 Brain activity reconstruction: Preliminary

Brain imaging or brain activity reconstruction can be considered a subfield of medical image processing [26]. The main objective is a better understanding the electrophysiological, hemodynamic, metabolic and neurochemical process through functional analysis of images obtained using non-invasive techniques as single photon emission computer tomography (SPECT), positron emission tomography (PET), functional magnetic resonance imaging (fMRI), magnetoencephalography (MEG) or electroencephalography (EEG) [6]. At the end, the normal or pathological brain functionalities will be analyzed by expert medical staff and researchers for neuroscience studies and clinical applications [7, 26, 27]. These techniques for brain imaging can be split in two specific classes: those with high temporal resolution e.g., EEG, MEG and those with high spatial resolution e.g., PET, fMRI [2, 8], however, brain imaging from EEG signals has been the method with the most number the research publications and therefore, this technique has been an active area of interest for decades. This has been possible due to its contributions to studies on brain diseases such as epilepsy. This disease is characterized by the speed with which events are propagated whereby many regions are seen in the images. Besides, epilepsy is the most important and common neurological disorder, at least the 1% of the world populations is suffering [6]. Onwards, this work will only be focused in brain activity reconstruction from EEG signals called EEG source localization.

1.2 EEG source localization

Localization of active sources inside the brain (onwards EEG source localization - ESL) involves two problems, namely: Forward problem and neuroelectric inverse problem.

1.2.1 Forward problem

Forward problem is related to the calculation of the electrical distribution of the potential on the surface of the head (scalp) from current sources in the brain which have a positions, orientations and magnitudes. Besides, head volume with geometry and electrical conductivity is given [3, 6, 28, 29]. By using a quasistatic approximation to Maxwell's equations is possible to obtain a linear map with the relationship between the activity generated by a set of active sources arbitrary located and the signals observed by a set of sensors over the scalp [2, 3, 8].

To solve the forward problem requires a head model either *spherical* or *realistic*. The first one uses some assumptions such as modeling a set of nested concentric homogeneous and isotropic spheres, but the real head is anisotropic, inhomogeneous and not spherical. For this reason the second one used anatomical information from images taken magnetic resonance or X-ray computed tomography and the extracted surfaces are included in numerically methods to calculate the head model [2, 28].

Distributed source models in EEG can use, as candidate sources to explain the measurements on the scalp, an amount that can be of the order of thousands of current dipoles. They can be located in a three-dimensional grid within the brain or over a surface of the cortical mantle, in both cases, obtained from MRIs. Then, using the Maxwell's equations, it is possible to point out of the contribution linearity of each dipole. Finally, the linearity of the forward problem is not an assumption, it is a fact based on fundamental physics of the problem [30, 31].

Therefore, the relationship between the measurements on the scalp and the primary current density generated by the neural activity, can be described by the following equation:

$$\boldsymbol{y} = \boldsymbol{M}\boldsymbol{x} + \boldsymbol{\epsilon} \tag{1.1}$$

The eq. 1.1 is a static version where $\boldsymbol{y} \in \mathbb{R}^{d\times 1}$ denotes d EEG measurements and $\boldsymbol{x} \in \mathbb{R}^{n\times 1}$ denotes the amplitude of n current sources normally oriented within the brain. The matrix $\boldsymbol{M} \in \mathbb{R}^{d\times n}$ is the lead field matrix given by a predefined head model and a specific distribution of electrodes locations, and being $\boldsymbol{\epsilon} \in \mathbb{R}^{d\times 1}$ is the observation noise measured with spatial covariance $\boldsymbol{C}_\epsilon \in \mathbb{R}^{d\times d}$.

1.2.2 Neuroelectric inverse problem

The neuroelectric inverse problem (NIP) is an ill-posed and mathematically underdetermined problem, because it is necessary to choose one solution of an infinite number of possible solutions. In other words, the number of possible sources inside the brain (unknown variables) is greater than the sensors or electrodes on the scalp (known variables) [2, 5, 6, 9, 29]. This situations is possible to solve in different ways. As regards

the EEG inverse problem there are two main approaches to solve the neuroelectric inverse problem [9], namely: Equivalent current dipole (ECD) models or dipole method (Parametric modeling [2]), and distributed source models (DIS) or distributed linear solution or imaging methods (non-parametric modeling [2]). The first one does an approximation of the actual current distribution, from a small and focal set of current dipoles with unknown locations, amplitudes and orientations. On the other hand, the assumption is that the recorded activity is the result of taking into account all possible sources simultaneously [2, 3, 6, 8, 9, 28, 29], and these dipoles sources are distributed in the whole brain volume or cortical surface with a fixed locations and orientations. In this work, the solution to the inverse problem will be addressed to the non-parametric approach or DIS.

Beamforming approach. This approach is representative of the parametric models to EEG source localization. A beamformer performs spatial filtering on data from a sensor array to discriminate between signals arriving from a location of interest and those originating elsewhere.

Linearly constrained minimum variance (LCMV) beamforming provides an adaptive alternative in which the limited degrees of freedom are used to place nulls in the response at positions corresponding to interfering sources, i.e., neural sources at locations other than r_q. This nulling is achieved by simply minimizing the output power of the beamformer subject to a unity gain constraint at the desired location r_q [2, 32].

To improve the spatial resolution and being able to have an unique solution, some solutions of the inverse problem have assumed temporal independence between the underlying sources and the measurements on the scalp. Besides, they have imposed convenient computational and probabilistic prior constraints as part of these solutions [7, 8]. Some of these solutions will be described below:

Spatial constraints for solution to the inverse problem

There are solutions to the inverse problem that can be considered relevant reference within the background, they have been used as a comparative reference and nowadays, they still remain. For this reason is important to know their solution structures. As mentioned above, it is necessary to restrict the space solution through specific constraint that can be onto the current sources [29].

Minimum Norm Estimate **(MNE)**.

This method looks for a solution with minimum power and was proposed in [1, 33] as follows:

$$\widehat{\boldsymbol{x}} = \underset{\boldsymbol{x}}{\operatorname{argmin}}\{\|\boldsymbol{y} - \boldsymbol{M}\boldsymbol{x}\|^2 + \boldsymbol{\lambda}^2\|\boldsymbol{x}\|^2\} \tag{1.2}$$

The typical cost function showed in eq. 1.2 is a Tikhonov-Phillips regularized functional and $\boldsymbol{\lambda}$ is a regularization parameter. The solution can be estimated as follows [5, 9, 33, 34]:

$$\widehat{\boldsymbol{x}} = (\boldsymbol{M}^\top \boldsymbol{M} + \boldsymbol{\lambda}^2 \boldsymbol{I}_n)\boldsymbol{M}^\top \boldsymbol{y} \tag{1.3}$$

Weighted Minimum Norm Estimates - **WMNE**.

The tendency of *MNE* is to favour those weak and surface sources. Therefore, weighted minimum norm estimate (*WMNE*) algorithm was proposed to compensate this problem [9]. The regularized functional is the following [29, 35]:

$$\widehat{\boldsymbol{x}} = \underset{\boldsymbol{x}}{\operatorname{argmin}}\{ \quad \|\boldsymbol{y} - \boldsymbol{M}\boldsymbol{x}\|_2^2 + \boldsymbol{\lambda}^2 \|\boldsymbol{W}\boldsymbol{x}\|^2\} \tag{1.4}$$

The $\boldsymbol{W}$ is a weighting matrix, it is obtained from:

$$\boldsymbol{W} = \Omega \otimes \boldsymbol{I}_3 \tag{1.5}$$

The eq. (1.5) is according to [9], another way for $\boldsymbol{W}$ could be [36]:

$$\boldsymbol{W} = ||\boldsymbol{M}_i||_2 \tag{1.6}$$

where different assumptions, about $\boldsymbol{W} \in \mathbb{R}^{n \times n}$, could be done in two different ways :

LOw REsolution TomograAphy - ***LORETA***

When $\boldsymbol{W}$ is considered as $\boldsymbol{W} = \boldsymbol{L}^\top \boldsymbol{L}$ where $\boldsymbol{L} \in \mathbb{R}^{n \times n}$ is termed **Laplacian** matrix and it can be seen in [20, 37] for more details. LORETA seeks to obtain the solution with the maximum spatial smoothness. In this case the eq. 1.4 can be rewritten, considering the defined $\boldsymbol{W}$ before and considering measurement noise ϵ according to eq. 1.1:

$$\widehat{\boldsymbol{x}} = \underset{\boldsymbol{x}}{\operatorname{argmin}}\{\|\boldsymbol{y} - \boldsymbol{M}\boldsymbol{x}\|_{C_\epsilon}^2 + \boldsymbol{\lambda}^2 \|\boldsymbol{L}^\top \boldsymbol{L}\boldsymbol{x}\|^2\} \tag{1.7}$$

being the solution as follows:

$$\widehat{\boldsymbol{x}} = (\boldsymbol{M}^\top \boldsymbol{C}_\epsilon^{-1} \boldsymbol{M} + \boldsymbol{\lambda}^2 \boldsymbol{L}^\top \boldsymbol{L})\boldsymbol{M}^\top \boldsymbol{C}_\epsilon^{-1} \boldsymbol{y} \tag{1.8}$$

Sparseness constraints for focused inverse solutions

There is an accepted neurophysiological concept which is related with the functional specialization of small brain areas. It means that some specific stimulus attributes or experimental contexts are restricted to small regions in the brain. Therefore, some methods have addressed their solutions to spatially focal estimations. Particularly, sparseness constraints can improve better results when they are used in brain activities evoked by external stimuli (visual, auditory or somatosensory) [7]. In this part, some methods will be mentioned without making a detailed description of them.

The sparseness constraints lead to spatially focal solutions and they can be within the recursive weighted methods where the $\boldsymbol{W}$ described before is a diagonal matrix that can be interpreted as the equal size of contribution to measurements from all sources (FOCal Underdetermined System Solution - FOCUSS) [6, 29, 38] or within norm regularization methods as Selective Norm Minimum (SMN) where the minimization problem is made using linear programming and based on $\boldsymbol{L}_1$-norm constraint [8].

Nowadays, sparsity is a important topic to improve the inverse solutions, because the activity generated by some sources can be sparse compared with the large number of possible current dipoles [10].

Spatio-temporal constraints for solution to the inverse problem

Computing the solution of the inverse problem, individually at each point in time can be convenient under the assumption of temporal independence and many methodologies have showed suitable approximations. Nevertheless, these methods are ignoring the temporal structure that can be regarded in EEG recordings and which could used to improve the inverse solutions [8].

Some methods for ESL have incorporated temporal smoothness constraints as part of a general Bayesian framework. Arbitrary prior distribution for dipole sources in space and time are specified by these approaches, sometimes in terms of basis functions which can limit or separate in space and time the interactions in order to reach simplified estimation algorithms [15, 39–41].

Multiple sparse priors - ***MSP***

The proposed Bayesian framework with this method is based on hierarchical or empirical Bayes to brain activity reconstruction from EEG signals. The main idea in this method is obviated priors with a specific form or with spacial structure; instead of this, MSP automatically selects multiple cortical sources with a compact support which are specified in terms of empirical priors [15]. Besides, the solution to the inverse problem allows sparse or distributed solutions, according to the data.

In this method, the forward model from eq. (1.1) is considered as a general linear model (GLM). Under Gaussian assumptions the solution of the GLM can be expressed as follows:

$$\widehat{x} = E[p(\boldsymbol{x} \mid \boldsymbol{y})] \quad \propto \quad \min_{\boldsymbol{y}} \quad p(\boldsymbol{y} \mid \boldsymbol{x}) p_0(\boldsymbol{x}) \tag{1.9}$$

where the likelihood is $p(\boldsymbol{y} \mid \boldsymbol{x}) = \mathcal{N}(\boldsymbol{y}; \boldsymbol{J}\boldsymbol{x}, \Sigma_\epsilon)$, with $\boldsymbol{J} \approx \boldsymbol{M}^{-1}$. Besides, the prior source probability distribution is $p_0(\boldsymbol{x}) = \mathcal{N}(\boldsymbol{x}; 0, \boldsymbol{Q})$. If $\boldsymbol{x}$ and $\boldsymbol{\epsilon}$ are assumed a priori as a Gaussian processes with a zero mean and covariances $\boldsymbol{Q}$ and $\boldsymbol{\Sigma}_\epsilon$ respectively; and $\mathcal{N}(\cdot)$ is the multi normal probability density function.

According with [9] the eq. (1.9) can be minimized to get the following estimation:

$$\widehat{\boldsymbol{x}} = \boldsymbol{Q}\boldsymbol{M}^{\top}(\boldsymbol{\Sigma}_{\epsilon} + \boldsymbol{M}\boldsymbol{Q}\boldsymbol{M}^{\top})^{-1}\boldsymbol{y} \tag{1.10}$$

This static solution could be extended to dynamic activity using temporal projectors proposed in [39, 41].

MSP is a algorithm based on empirical Bayes and it divides the smoother associated to the prior source covariance matrix, into a set of N_q diagonal components $C = \{C_1, \ldots, C_{N_q}\}$ [21]. These components are weighted by the algorithm and ensuing the sensor covariance $\boldsymbol{Q}$ is estimated under the assumption that each component describes covariance of the connections among patch of cortex.

$$\boldsymbol{Q} = \sum_{i=1}^{N_q} e^{\lambda_i} C_i$$

In absence of prior information as a fMRI, the components can be generated with Green's function. With the aim to estimate the hyperparameter set that determines the best covariance weight, it must maximize the termed free energy as follows:

$$F = -\frac{T}{2} tr(\boldsymbol{\Delta}^{-1}\boldsymbol{C}) - \frac{T}{2}\ln|\boldsymbol{\Delta}| - \frac{CT}{2}\ln 2\Pi - \frac{1}{2}(\boldsymbol{\mu}-\boldsymbol{\eta})^{\top}\Omega^{-1}(\boldsymbol{\mu}-\boldsymbol{\eta}) + \frac{1}{2}\ln|\Upsilon\Omega^{-1}| \tag{1.11}$$

where $\boldsymbol{\Delta} \in \Re^{d\times d}$ is a estimated model covariance, computed as $\boldsymbol{\Delta} = \boldsymbol{M}\boldsymbol{Q}\boldsymbol{M}^{\top} + \boldsymbol{\Sigma}_{\epsilon}$; $\boldsymbol{C} \in \Re^{d\times d}$ is the measured data covariance, and $\boldsymbol{\mu}, \boldsymbol{\eta} \in \Re^{N_q\times 1}$ are the vector of prior and posterior covariance of the hyperparameters.

On the other hand, some methods have been used state-space models as dynamical model for the current sources [20, 35, 37]. In this dynamic context is allowed that the sources change during the measurement process; therefore, the neuroelectric inverse problem can be solved every moment of time. It is important taking into account that the static problem or instantaneous inverse problem is solved at specific instant of time, whereas in the dynamical problem the generators have some imposed dynamic; hence, the observations depend on this dynamic and therefore the solutions too. Without dynamics, the dynamical inverse problem can be a generalization of the instantaneous inverse problem [29].

The dynamical version of the static forward problem described in eq. 1.1 is the following:

$$\boldsymbol{y}_k = \boldsymbol{M}\boldsymbol{x}_k + \boldsymbol{\epsilon}_k \tag{1.12a}$$

$$\boldsymbol{x}_k = \boldsymbol{f}\left(\boldsymbol{x}_{k-1}, \ldots, \boldsymbol{x}_{k-m}\right) + \boldsymbol{\eta}_k \tag{1.12b}$$

where $\boldsymbol{k} = 1, 2, \ldots, \boldsymbol{T}$ being $\boldsymbol{k}$ the current sample and $\boldsymbol{T}$ the total number of samples. In eq. 1.12b $\boldsymbol{f} : \mathbb{R}^n \longrightarrow \mathbb{R}^n$ is a linear o non-linear vector function of order m that models

the dynamics of the neural activity and being $\boldsymbol{\eta}_k \in \mathbb{R}^{n\times 1}$ a zero mean uncorrelated Gaussian noise with structure covariance matrix $\boldsymbol{C}_{\boldsymbol{\eta}} \in \mathbb{R}^{n\times n}$. The dimensions of others variables in eq. 1.12 remain the same as those of the eq.1.1[16].

Dynamical inverse solutions: Iterative Regularized Algorithm - IRA

The following equation was the first approximation where a temporal constraint was involved:

$$\widehat{\boldsymbol{x}}_k = \underset{\boldsymbol{x}_k}{argmin}\{\|\boldsymbol{y}_k - \boldsymbol{M}\boldsymbol{x}_k\|^2 + \boldsymbol{\lambda}\|\boldsymbol{L}\boldsymbol{x}_k\|_1^2 + \boldsymbol{\lambda}\|\boldsymbol{L}(\boldsymbol{x}_k - \boldsymbol{x}_{k-1})\|_2^2\} \tag{1.13}$$

Being $\boldsymbol{y}_k \in \mathbb{R}^{d\times 1}$ the d EEG measurements and $\widehat{\boldsymbol{x}}_k \in \mathbb{R}^{n\times 1}$ the n potentials sources within the brain. Besides, being $\boldsymbol{M} \in \mathbb{R}^{d\times n}$ the lead field matrix given by a predefined head model and a specific distribution of electrode locations, and $\boldsymbol{L} \in \mathbb{R}^{n\times n}$ is termed Laplacian matrix containing the spatial interactions among sources [37].

This approach has evolved and it can be described through a state-space representation similar to the eq.1.12. However, the next state-space model is general dynamical representation:

$$\boldsymbol{y}_k = \boldsymbol{M}\boldsymbol{x}_k + \boldsymbol{\epsilon}_k \tag{1.14a}$$

$$\boldsymbol{x}_k = \boldsymbol{f}\left(\boldsymbol{x}_{k-1}, \ldots, \boldsymbol{x}_{k-m}, \boldsymbol{\omega}_k\right) + \boldsymbol{\eta}_k \tag{1.14b}$$

$$\boldsymbol{\omega}_k = \boldsymbol{g}(\boldsymbol{\omega}_{k-1}) + \boldsymbol{\nu}_k \tag{1.14c}$$

where the vector $\boldsymbol{\omega} \in \mathbb{R}^{p\times 1}$ holds the parameters of the function $\boldsymbol{f}$ and that can model some external influence on the brain and the covariance matrix $\boldsymbol{C}_{\boldsymbol{\eta}}$ is defined by $\boldsymbol{\tau}^2(\boldsymbol{L}^\top\boldsymbol{L})^{-1}$ [16, 37].

The EEG source localization formulates by a state-space model, it is a natural way to combine spatial and temporal constraints for its solution. In this structure, the measurement process is represented by the observation equation, and the state equation is represented by the spatio-temporal dynamics of the sources [7]. From proposed methods by [20, 37] until nowadays, the structure is the same, but, depending on the analyst, who can choose the most suitable dynamical model e.g., linear, non-linear or varying in the time [12, 16].

Another advantage of this representation is being able to adapt within a Kalman Filter's structure or within iterative regularized structure (Iterative Regularization Algorithm - IRA).

The following functional is proposed by [11] and it is solved using IRA:

$$\begin{aligned}\boldsymbol{\Phi}(\boldsymbol{x}_k, \boldsymbol{\omega}_k, \boldsymbol{\lambda}, \boldsymbol{\gamma}) = &\|\boldsymbol{P}(\boldsymbol{y}_k - \boldsymbol{M}\boldsymbol{x}_k)\|^2 \\ &+ \boldsymbol{\lambda}\|\boldsymbol{Q}(\boldsymbol{x}_k - \boldsymbol{f}(\widehat{\boldsymbol{x}}_k, \ldots, \widehat{\boldsymbol{x}}_{k-m}, \boldsymbol{\omega}_k))\|^2 \\ &+ \boldsymbol{\gamma}\|\boldsymbol{R}(\boldsymbol{\omega}_k - \boldsymbol{g}(\widehat{\boldsymbol{\omega}}_{k-1}))\|^2\end{aligned} \tag{1.15}$$

where $\boldsymbol{\lambda} \in \mathbb{R}^+$ and $\boldsymbol{\gamma} \in \mathbb{R}^+$ are the regularization parameters that control the minimization process. Weight Matrices $\boldsymbol{P} \in \mathbb{R}^{d\times d}$, $\boldsymbol{Q} \in \mathbb{R}^{n\times n}$ and $\boldsymbol{R} \in \mathbb{R}^{p\times p}$ are related to the noise covariance matrices of the measurements, states and parameter equations, respectively. The covariance matrix of the scalp measures

The multivariate optimization task described by eq. 1.15 must be solved in a iterative way, for one variable at a time, while the another must remain fixed, as follows:

Being estimated states $\widehat{\boldsymbol{x}}_k$ known:

$$\widehat{\boldsymbol{\omega}}_k = (\boldsymbol{G}_k^\top \boldsymbol{\Lambda}^{-1}\boldsymbol{G}_k + \boldsymbol{\Gamma}^{-1})^{-1}(\boldsymbol{G}_k^\top \boldsymbol{\Lambda}^{-1}\widehat{\boldsymbol{x}}_k + \boldsymbol{\Gamma}^{-1}\boldsymbol{g}(\boldsymbol{\omega}_{k-1})) \tag{1.16}$$

and, being estimated parameters $\widehat{\boldsymbol{\omega}}_k$ known:

$$\widehat{\boldsymbol{x}}_k = (\boldsymbol{I}_n + \boldsymbol{\Lambda}\boldsymbol{M}^\top(\boldsymbol{M}\boldsymbol{\Lambda}\boldsymbol{M}^\top + \boldsymbol{\Sigma})^{-1}\boldsymbol{M})(\boldsymbol{\Lambda}\boldsymbol{M}^\top\boldsymbol{\Sigma}^{-1}\boldsymbol{y}_k + \boldsymbol{f}(\widehat{\boldsymbol{x}}_k, \ldots, \widehat{\boldsymbol{x}}_{k-m}, \boldsymbol{\omega}_k)) \tag{1.17}$$

where $\boldsymbol{\Sigma} = (\boldsymbol{P}^\top\boldsymbol{P})^{-1}$, $\boldsymbol{\Sigma} \in \mathbb{R}^{d\times d}$ is the covariance matrix of the scalp measurements, $\boldsymbol{\Lambda} = (\boldsymbol{Q}^\top\boldsymbol{Q})^{-1}/\boldsymbol{\lambda}$, $\boldsymbol{\Lambda} \in \mathbb{R}^{n\times n}$ is the state covariance matrix and $\boldsymbol{\Gamma} = (\boldsymbol{R}^\top\boldsymbol{R})^{-1}/\boldsymbol{\gamma}$, $\boldsymbol{\Gamma} \in \mathbb{R}^{p\times}$ is the parameter noise covariance matrix. Besides, the matrix $\boldsymbol{G}_k$ is built with the previous estimate states as follows:

$$\boldsymbol{G}_k = \begin{bmatrix}\widehat{\boldsymbol{x}}_{k-1} & \widehat{\boldsymbol{x}}_{k-1}^{\circ 2} & \widehat{\boldsymbol{x}}_{k-1}^{\circ 3} & \widehat{\boldsymbol{x}}_{k-2} & \widehat{\boldsymbol{x}}_{k-\boldsymbol{\tau}}\end{bmatrix} \tag{1.18}$$

This work compared two dynamical models, linear and non-linear models. First, non-linear model will be described and called Dynamic Neural Fields (DNF). DNF models the state evolution of current density dynamics by incorporating corticothalamic connectivity and thalamic non-linearity [11, 16, 23]:

$$\boldsymbol{f}(\boldsymbol{x}_{k-1}, \ldots, \boldsymbol{x}_{k-2}) = \boldsymbol{A}_1\boldsymbol{x}_{k-1} + \boldsymbol{A}_2\boldsymbol{x}_{k-1}^{\circ 2} + \boldsymbol{A}_3\boldsymbol{x}_{k-1}^{\circ 3} + \boldsymbol{A}_4\boldsymbol{x}_{k-2} + \boldsymbol{A}_5\boldsymbol{x}_{k-1} \tag{1.19}$$

with $\boldsymbol{A}_1 = \boldsymbol{a}_1\boldsymbol{I}_n + \boldsymbol{b}_1\boldsymbol{L}$, $\boldsymbol{A}_2 = \boldsymbol{a}_2\boldsymbol{I}_n$, $\boldsymbol{A}_3 = \boldsymbol{a}_3\boldsymbol{I}_n$, $\boldsymbol{A}_4 = \boldsymbol{a}_4\boldsymbol{I}_n$ and $\boldsymbol{A}_5 = \boldsymbol{a}_5\boldsymbol{I}_n$, $\boldsymbol{I}_n \in \mathbb{R}^{n\times n}$ is the identity matrix, $\boldsymbol{L} \in \mathbb{R}^{n\times n}$ is the spatial Laplacian matrix to hold spatial interactions among current sources and $\boldsymbol{\tau} \in \mathbb{R}^+$ is a delayed feedback.

Chapter 2

Dynamic Electroencephalographic modeling

2.1 Introduction

The forward model is the first problem which must be taken into account by proposing a solution for the neuroelectric inverse problem. This part is necessary to know the activity inside the brain, this activity is obtained from a set of neural current sources that allow computing the scalp potentials and external fields. Usually, the temporal evolution of this activity is considered spatially homogeneous; that is,the temporal evolution of the normal activity (stable activity) or the pathological activity (unstable activity) is the same throughout the brain.

According to some works, there is a notion of functional specialization which has been accepted because this is consistent with those spatially focal solutions. This notion states that specialized cortical activities can be restricted to small regions according to specific stimulus attributes or experimental contexts [7]. Spatially focal solutions are associated to sparseness constraints which provide a good match to evoked brain activities. Therefore, if it is wanted to find spatially focal currents, it is necessary to consider temporal constraints, but taking into account that temporal evolution is spatially non-homogeneous.

The contribution of this work is a dynamical model whose temporal evolution is spatially non-homogeneous, this means that the activity is not the same in all areas of the brain. Therefore, the proposed model considers that each area in the brain evolves with its individual dynamic.

2.2 EEG generation: Homogeneous and Non-homogeneous forward problem

The problem of EEG source localization (ESL) can be formulated through a state-space model, this structure allows to combine spatial and temporal constraints in a natural way. In this framework the observation equation will represent the measurement process whereas the state equation will represent the spatio-temporal dynamics of the current sources [7, 20, 32, 37, 41].

2.2.1 State-Space Modeling

State-space models have been proposed and they have considered two equations to represent the spatio-temporal constraints upon them. The first one allows to observe the electric fields from unobserved currents (observation equation) and the second equation describes the temporal evolution of the currents (state equation) [5].

Observation equation. The observed electric fields or EEG signals are represented by $\boldsymbol{y}_k \in \mathbb{R}^{d\times 1}$ where d is the number of electrodes on the scalp, the amplitude of n current sources $\boldsymbol{x}_k \in \mathbb{R}^{n\times 1}$. $\boldsymbol{M} \in \mathbb{R}^{d\times n}$ is called the lead field matrix which relates the EEG with the neural activity at each source [5, 16].

$$\boldsymbol{y}_k = \boldsymbol{M}\boldsymbol{x}_k + \boldsymbol{\epsilon}_k \tag{2.1}$$

The subscript k is the sample associated to the time instant $t_k = kh$ which represents the $k-$th sample of the EEG recording, where $k = 1, ..., N$, being N the total number of samples, and h the sample time. ε_k is an additive uncorrelated Gaussian noise with covariance a C_ε and zero mean.

State-Equation. To model the temporal evolution of a current sources was used a physiologically non-linear model proposed by [23]. They presented a non-linear continuum model which considers a neural activity propagation as follows:

$$\frac{d\boldsymbol{v}}{dt} = \begin{bmatrix} 0 & 1 \\ \gamma^2 c_1 & -2\gamma \end{bmatrix} \boldsymbol{v}(t) + \begin{bmatrix} 0 & 0 \\ \gamma^2 c_2 & 0 \end{bmatrix} \boldsymbol{v}(t-t_0) + \begin{bmatrix} 0 & 0 \\ \gamma^2 c_3 & 0 \end{bmatrix} \boldsymbol{v}^2(t) + \begin{bmatrix} 0 & 0 \\ \gamma^2 c_4 & 0 \end{bmatrix} \boldsymbol{v}^3(t) + \begin{bmatrix} 0 \\ \gamma^2 \eta \end{bmatrix} \tag{2.2}$$

where the constant c_1 represents the instantaneous feedback due to nearby neurons, c_2 the delayed feedback via an extra-cortical loop with t_0 as the time delay of this feedback, γ is a characteristic decay rate of the field activity $\boldsymbol{x}(t)$ and η is a random white noise and it is considered as an external stimulus to perturb the brain states [23]. The variable $\boldsymbol{v}(t)$ is defined like:

$$\boldsymbol{v}(t) = \begin{bmatrix} \boldsymbol{x}(t) \\ \frac{d\boldsymbol{x}(t)}{dt} \end{bmatrix} \tag{2.3}$$

Discrete physiologically non-linear model can be computed applying the Taylor's approach forward differences for the derivative term in the eq. (2.2), and following the procedure presented in [42] is possible to obtain the following model of the activity $\boldsymbol{x}_k$ in terms of the kth sample.

$$\boldsymbol{x}_k = a_1\boldsymbol{x}_{k-1} + a_2\boldsymbol{x}_{k-1}^{\circ 2} + a_3\boldsymbol{x}_{k-1}^{\circ 3} + a_4\boldsymbol{x}_{k-2} + a_5\boldsymbol{x}_{k-\tau} \tag{2.4}$$

being the terms $\boldsymbol{x}_{k-1}^{\circ 2}$ and $\boldsymbol{x}_{k-1}^{\circ 3}$ represent the corresponding Hadamard power of $\boldsymbol{x}_{k-2}$ the parameters of the model $a_1 \dots a_5$ can be found through the equations presented in the discrete model in [42]. The variable $\boldsymbol{\tau}$ represent the discrete version of the delayed feedback time t_0.

The discrete non-linear model presented by (2.4) can be consider as a *state equation* which models the temporal evolution of a current sources as follows:

$$\boldsymbol{x}_k = \boldsymbol{f}\left(\boldsymbol{x}_{k-1}, \boldsymbol{x}_{k-2}, \boldsymbol{x}_{k-\tau}\right) + \boldsymbol{\eta}_k \tag{2.5}$$

2.2.2 Homogeneous forward problem

In the eq. (2.5), $\boldsymbol{f} \in \mathbb{R}^{n\times 1}$ is a non-linear time-varying vector function that incorporates the corticothalamic connectivity and thalamic nonlinearity at each source as follows [11, 16, 23]:

$$\begin{aligned} \boldsymbol{f}\left(\boldsymbol{x}_{k-1}, \boldsymbol{x}_{k-2}, \boldsymbol{x}_{k-\tau}\right) = {} & \boldsymbol{A}_1\boldsymbol{x}_{k-1} + \boldsymbol{A}_2\boldsymbol{x}_{k-1}^{\circ 2} \\ & + \boldsymbol{A}_3\boldsymbol{x}_{k-1}^{\circ 3} + \boldsymbol{A}_4\boldsymbol{x}_{k-2} \\ & + \boldsymbol{A}_5\boldsymbol{x}_{k-\tau} + \boldsymbol{B}_1\boldsymbol{x}_{k-1} \end{aligned} \tag{2.6}$$

considering that the all current sources follow the same temporal evolution over the entire brain, this means that according to eq. (2.5) and eq. 2.6, the activity evolves over time in a spatially homogeneous way. The transition matrices can be defined as $\boldsymbol{A}_i = \operatorname{diag} \boldsymbol{a}_i$, $i = 1, \dots, 5$ where $\boldsymbol{a}_i \in \mathbb{R}$ and with $\boldsymbol{x}_k \in \mathbb{R}^{n\times 1}$ the neural activity at sample k, and where the term $\boldsymbol{x}_k^{\circ 2}$ denotes the Hadamard power, and being $\boldsymbol{\eta}_k \in \mathbb{R}^{n\times 1}$ a zero mean uncorrelated Gaussian noise. It is worth noting that the number of states n is large.

2.2.3 Non-homogeneous forward problem.

The areas in the brain can have different dynamics in different moments of time; hence, the solutions could be addressed to locate spatially focal current sources. These solutions are directly related to the sparseness constraints and they are consistent with the well-accepted notion of *functional specialization* [7].

Usually, the methods based on a state-space model do not locate spatially focal current sources, because those methods assume that the brain activity follows the same temporal evolution over the entire brain [32, 43] or over a given cortical area [16, 20, 37, 44].

The transitions matrices defined in eq. (2.6) can be rewritten as $\boldsymbol{A}_i = a_i \boldsymbol{I}_n$, and the state-equation (eq. (2.5)) spreads the activity over all current sources. However, if different cortical areas are considered and it is assumed that each evolves under its individual temporal dynamic, the state-equation would describe the temporal evolution of cortical areas with different dynamics, these dynamics could be stable or unstable (normal or pathological) activity.

Therefore, this work was looking for to propose spatially non-homogeneous conditions within the dynamic model and being able to generate time-varying EEG signals with normal and pathological time intervals. First, the entire brain was divided into $r \in \Re$ cortical areas where m areas were considered with normal activity (stable activity) and $r - m$ areas were considered with pathological activity (unstable activity). Then, each parameter a_i can be changed in $j = r - m + 1$ different values, one for each pathology plus one value to areas with normal activity. Therefore, the parameters would be rewritten as follows a_i^l, where $i = 1, \ldots, 5$ (number of parameters from temporal model) and $l = 1, \ldots, j$.

The transition matrix $\boldsymbol{A}_i \in \Re^{n \times n}$ can be rewritten as follows:

$$\boldsymbol{A}_i = \begin{bmatrix} \boldsymbol{A}_i^1 & \ddots & \boldsymbol{0} & \ddots & \cdots \\ \vdots & \boldsymbol{A}_i^2 & \ddots & \boldsymbol{0} & \vdots \\ \boldsymbol{0} & \ddots & \ddots & \ddots & \boldsymbol{0} \\ \vdots & \boldsymbol{0} & \ddots & \boldsymbol{A}_i^{(r-1)} & \vdots \\ \cdots & \ddots & \boldsymbol{0} & \ddots & \boldsymbol{A}_i^r \end{bmatrix} = \boldsymbol{S}_1 + \boldsymbol{S}_2 + \cdots + \boldsymbol{S}_{r-1} + \boldsymbol{S}_r$$

$$\boldsymbol{S}_1 = \begin{bmatrix} \boldsymbol{A}_i^1 & \ddots & \boldsymbol{0} & \ddots & \cdots \\ \vdots & \boldsymbol{0} & \ddots & \boldsymbol{0} & \vdots \\ \boldsymbol{0} & \ddots & \ddots & \ddots & \boldsymbol{0} \\ \vdots & \boldsymbol{0} & \ddots & \boldsymbol{0} & \vdots \\ \cdots & \ddots & \boldsymbol{0} & \ddots & \boldsymbol{0} \end{bmatrix}; \boldsymbol{S}_2 = \begin{bmatrix} \boldsymbol{0} & \ddots & \boldsymbol{0} & \ddots & \cdots \\ \vdots & \boldsymbol{A}_i^2 & \ddots & \boldsymbol{0} & \vdots \\ \boldsymbol{0} & \ddots & \ddots & \ddots & \boldsymbol{0} \\ \vdots & \boldsymbol{0} & \ddots & \boldsymbol{0} & \vdots \\ \cdots & \ddots & \boldsymbol{0} & \ddots & \boldsymbol{0} \end{bmatrix}$$

$$\boldsymbol{S}_{r-1} = \begin{bmatrix} \mathbf{0} & \ddots & \mathbf{0} & \ddots & \cdots \\ \vdots & \mathbf{0} & \ddots & \mathbf{0} & \vdots \\ \mathbf{0} & \ddots & \ddots & \ddots & \mathbf{0} \\ \vdots & \mathbf{0} & \ddots & \boldsymbol{A}_i^1 & \vdots \\ \cdots & \ddots & \mathbf{0} & \ddots & \mathbf{0} \end{bmatrix}; \boldsymbol{S}_r = \begin{bmatrix} \mathbf{0} & \ddots & \mathbf{0} & \ddots & \cdots \\ \vdots & \mathbf{0} & \ddots & \mathbf{0} & \vdots \\ \mathbf{0} & \ddots & \ddots & \ddots & \mathbf{0} \\ \vdots & \mathbf{0} & \ddots & \mathbf{0} & \vdots \\ \cdots & \ddots & \mathbf{0} & \ddots & \boldsymbol{A}_i^r \end{bmatrix}$$

where $\boldsymbol{A}_i^r = a_i^l \boldsymbol{I}_{w_l}$. The matrix $\boldsymbol{I}_w \in \Re^{w \times w}$ and w is the size of the cortical area, it can have different sizes, but the following condition must be satisfied $\sum_{g=1}^{r}(w_g) = n$, e.g. if the brain activity is divided in $r = 3$ cortical areas, 1 of them is a pathology (unstable activity) associated to epilepsy, the another 2 cortical areas the activity is normal (stable activity). Therefore, $j = 2$ and the brain activity only has one change of parameters, one cortical area associated to the normal activity a_i^N and one cortical area associated to the pathological activity a_i^P. The temporal evolution o State-equation can be written as follows:

$$\boldsymbol{A}_i = \begin{bmatrix} \boldsymbol{A}_i^N & \mathbf{0} & \mathbf{0} \\ \mathbf{0} & \boldsymbol{A}_i^P & \mathbf{0} \\ \mathbf{0} & \mathbf{0} & \boldsymbol{A}_i^N \end{bmatrix} = \begin{bmatrix} \boldsymbol{A}_i^N & \mathbf{0} & \mathbf{0} \\ \mathbf{0} & \mathbf{0} & \mathbf{0} \\ \mathbf{0} & \mathbf{0} & \mathbf{0} \end{bmatrix} + \begin{bmatrix} \mathbf{0} & \mathbf{0} & \mathbf{0} \\ \mathbf{0} & \boldsymbol{A}_i^P & \mathbf{0} \\ \mathbf{0} & \mathbf{0} & \mathbf{0} \end{bmatrix} + \begin{bmatrix} \mathbf{0} & \mathbf{0} & \mathbf{0} \\ \mathbf{0} & \mathbf{0} & \mathbf{0} \\ \mathbf{0} & \mathbf{0} & \boldsymbol{A}_i^N \end{bmatrix} \tag{2.7}$$

being $\boldsymbol{A}_i^N = a_i^N \boldsymbol{I}_{w_1}$, $\boldsymbol{A}_i^P = a_i^P \boldsymbol{I}_{w_2}$ and the another $\boldsymbol{A}_i^N = a_i^N \boldsymbol{I}_{w_3}$, the parameters for normal activity (stable activity) are the same in all cortical regions with this activity, the difference among normal activity regions is the size of the area. The $\mathbf{0}$ are zero matrices with suitable size. Therefore the eq. (2.7) could be rewritten as follows:

$$\begin{bmatrix} \boldsymbol{A}_i^N & \mathbf{0} & \mathbf{0} \\ \mathbf{0} & \boldsymbol{A}_i^P & \mathbf{0} \\ \mathbf{0} & \mathbf{0} & \boldsymbol{A}_i^N \end{bmatrix} = \begin{bmatrix} \boldsymbol{A}_i^N & \mathbf{0} & \mathbf{0} \\ \mathbf{0} & \mathbf{0} & \mathbf{0} \\ \mathbf{0} & \mathbf{0} & \boldsymbol{A}_i^N \end{bmatrix} + \begin{bmatrix} \mathbf{0} & \mathbf{0} & \mathbf{0} \\ \mathbf{0} & \boldsymbol{A}_i^P & \mathbf{0} \\ \mathbf{0} & \mathbf{0} & \mathbf{0} \end{bmatrix} = \boldsymbol{A}\boldsymbol{n}_i + \boldsymbol{A}\boldsymbol{p}_i \tag{2.8}$$

The proposed model is the following:

$$\begin{aligned} \boldsymbol{f}\left(\boldsymbol{x}_{k-1}, \boldsymbol{x}_{k-2}, \boldsymbol{x}_{k-\tau}\right) = {} & \boldsymbol{A}\boldsymbol{n}_1 \boldsymbol{x}_{k-1} + \boldsymbol{A}\boldsymbol{p}_1 \boldsymbol{x}_{k-1} \\ & + \boldsymbol{A}_2 \boldsymbol{x}_{k-1}^{\circ 2} + \boldsymbol{A}_3 \boldsymbol{x}_{k-1}^{\circ 3} \\ & + \boldsymbol{A}\boldsymbol{n}_4 \boldsymbol{x}_{k-2} + \boldsymbol{A}\boldsymbol{p}_4 \boldsymbol{x}_{k-2} \\ & + \boldsymbol{A}_5 \boldsymbol{x}_{k-\tau} + \boldsymbol{B}_1 \boldsymbol{x}_{k-1} \end{aligned} \tag{2.9}$$

The zones can be active in the same time k or they can be activated, one by one, in different time intervals. The following experimental framework was done to show this model of temporal evolution.

2.2.4 Experimental framework.

The authors in [23] proposed the values to get the discrete values for the eq. (2.6). The discrete values used to simulate normal activity in the eq. 2.6 were $\tau = 20$, $a_1 = 1.0628$, $a_2 = 0.000143$, $a_3 = -0.000286$, $a_4 = -0.42857$, $a_5 = 0.008$, $b_1 = -0.12$ y $\|\boldsymbol{\eta}_k\| \leq 0.05$. Epileptic seizure can be simulated using eq. 2.6 by modifying the values of a_1 from 1.0628 to $a_1 = 1.3$, while $a_4 =$ from -0.428 to $a_4 = -1$ over the entire diagonal or in homogeneous conditions [11, 16].

The EEG measurements $\boldsymbol{y}_k$ were obtained by using eq. (2.1), the current source density $\boldsymbol{x}_x$ was multiplied by the lead field matrix $\boldsymbol{M}$ and $\boldsymbol{\epsilon}_k$ is to get the following testing value of SNR, in ths case $10db$. The head structure used to solve the inverse problem had $d = 120$ electrodes and $n = 8196$ dipole sources.

Forward model simulation

As it was mentioned before, the dynamic model eq. 2.6 can change the normal to pathological activity (epileptic seizure) by modifying the values of a_1 from 1.0628 to $a_1 = 1.3$, and $a_4 =$ from -0.428 to $a_4 = -1$ whereby the following results will be described considering these changes in specific instants of time.

1. Simulation of one active source. In Fig. 2.1 is showed the simulation of normal and generalized activity from $0s$ to $0.5s$, from $0.5s$ to $1s$ can be seen pathological activity generated. This activity is generated by one active source and its neighbors. On the right side, it can be seen the averaged brain activity during all the time and the location to the active sources. The simulations in two different instants of time are showed too. At $t = 300ms$ is showed the normal activity (on the top left) and at $t = 800ms$ is showed the epileptic seizure (on the top right).

2. Simulation of two active sources. The simulations was made during $1.5s$ and the time interval was split in three time ranges. In the First one was simulated normal and generalized activity (from $0s$ to $0.5s$), in the second interval of the time was activated the first source (from $0.5s$ to $1s$) and the third range was activated the second source (from $1s$ to $1.5s$). In Fig. 2.2 can be seen the generated EEG signal (center in the figure), brain activity averaged over time (on the left side), normal and generalized brain activity at $t = 300ms$ (on the top left), brain activity calculated at $t = 800ms$ for the first active source (on the top right) and brain activity calculated at $t = 1300ms$ for the second active source (on the right side)

3. Simulation of three active sources. The simulations was made during $2s$ and the time interval was split in 4 time ranges. In the first one was simulated normal and generalized activity (from $0s$ to $0.5s$), in the second interval of time was activated the first source (from $0.5s$ to $1s$) and in the third range was activated the third source (from $1.5s$ from $2s$). In Fig. 2.3 can be seen the generated EEG signal (center in the figure), brain activity averaged over time (on the left side), normal and generalized brain activity at $t = 300ms$ (on the top left), brain

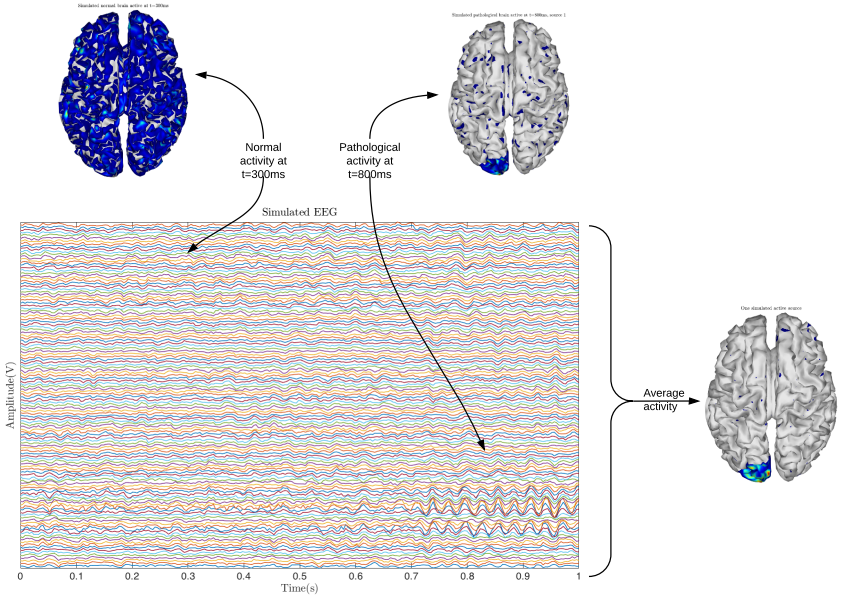

Figure 2.1: Simulated brain activity for one active source.

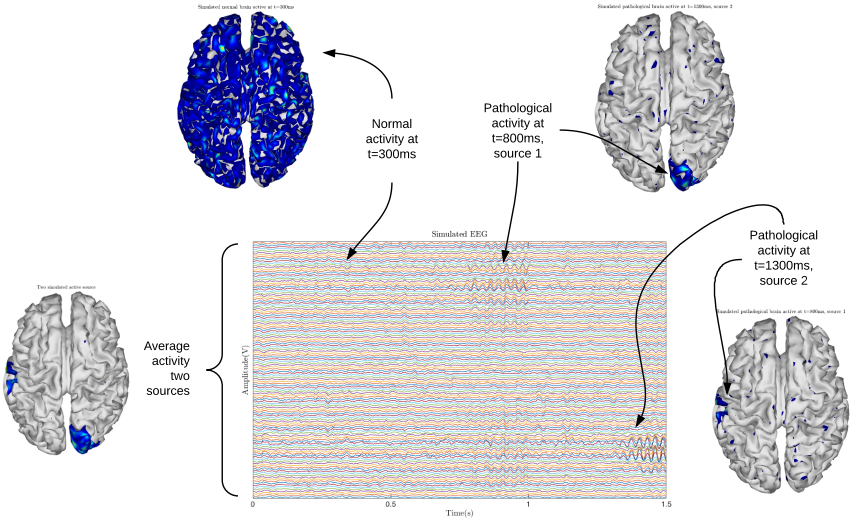

Figure 2.2: Simulated brain activity for two active sources.

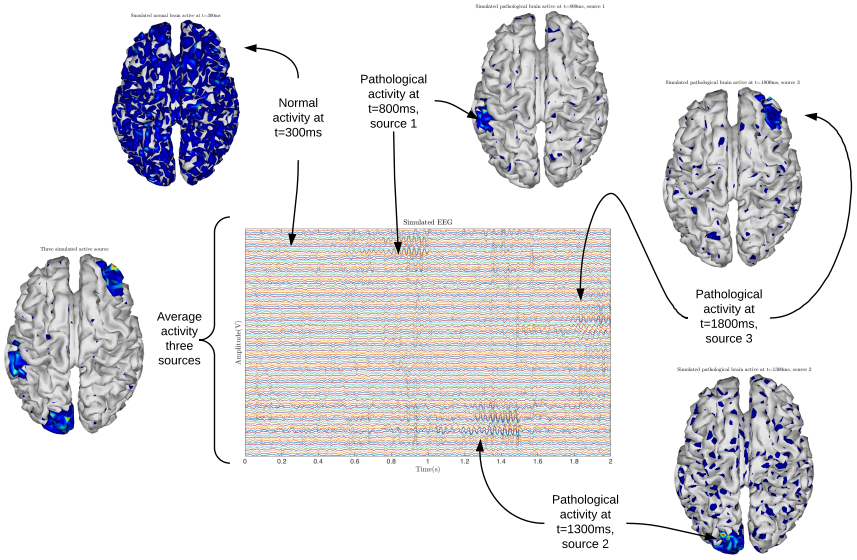

Figure 2.3: Simulated brain activity for three active sources.

activity calculated at $t = 800ms$ for the first active source (on the top right), brain activity calculated at $t = 1300ms$ for the second active source (on the top right side) and finally, the brain activity calculated at $t = 1800ms$ for the third active source (on the bottom right side).

ESL with non-homogeneous activity and reduced source space

In this experiment is used the same dynamical model described by eq. (2.5), but the source space is reduced as follows:

$$\boldsymbol{x}_k = \boldsymbol{\Phi}_s \boldsymbol{c}_k, \tag{2.10}$$

where the vector $\boldsymbol{c}_k \in \mathbb{R}^{s\times 1}$ weights the matrix of spatial coefficients, noted as $\boldsymbol{\Phi}_s \in \mathbb{R}^{n\times s}$. Considering the spatial basis (see (2.10)) the following model is obtained:

$$\boldsymbol{y}_k = \boldsymbol{M}\boldsymbol{\Phi}_s \boldsymbol{c}_k + \boldsymbol{\epsilon}_k, \tag{2.11}$$
$$\boldsymbol{c}_k = \boldsymbol{f}\left(\boldsymbol{c}_{k-1}, \boldsymbol{c}_{k-2}, \boldsymbol{c}_{k-\tau}, \boldsymbol{w}_k\right) + \boldsymbol{\eta}_k, \tag{2.12}$$

A discrete state space representation based on the structure of Eq. (2.13) and Eq. (2.11) is proposed for describing the non-homogeneous activity into the brain. The proposed model assumes that each zone evolves industryependently from others, and its dynamical behavior can be defined as time-varying. These features allow that the proposed model describes adequately normal and pathological non-homogeneous activity, even

for localized epilepsy events. This model can be defined as follows:

$$\begin{aligned} \boldsymbol{f}\left(\boldsymbol{c}_{k-1}, \boldsymbol{c}_{k-2}, \boldsymbol{c}_{k-\tau}, \boldsymbol{w}_k\right) = \boldsymbol{A}_1\boldsymbol{c}_{k-1} + \boldsymbol{A}_2\boldsymbol{c}_{k-2} \\ + \boldsymbol{A}_3\boldsymbol{c}_{k-\tau} + \boldsymbol{A}_4\boldsymbol{c}_{k-1}^2 + \boldsymbol{A}_5\boldsymbol{c}_{k-1}^3, \end{aligned} \tag{2.13}$$

being $\boldsymbol{A}_1 = \operatorname{diag}(\boldsymbol{a}_1)$, $\boldsymbol{A}_2 = \operatorname{diag}(\boldsymbol{a}_2)$, $\boldsymbol{A}_3 = \operatorname{diag}(\boldsymbol{a}_3)$, $\boldsymbol{A}_4 = \operatorname{diag}(\boldsymbol{a}_4)$ and $\boldsymbol{A}_5 = \operatorname{diag}(\boldsymbol{a}_5)$, where $\boldsymbol{A}_i \in \mathbb{R}^{s\times s}$ and $\boldsymbol{a}_i \in \mathbb{R}^{s\times 1}$ are the parameters matrices which described the dynamics of the model. The vector function $\boldsymbol{f}$ is time varying since $\boldsymbol{w}_k \in \mathbb{R}^{p\times 1}$ can change at each sample k. The set of parameters associated with the dynamics of (2.13) is $\boldsymbol{w}_k$ with $p = 5s$ defined as

$$\boldsymbol{w}_k^\mathsf{T} = \begin{bmatrix} \boldsymbol{a}_1^\mathsf{T} & \boldsymbol{a}_2^\mathsf{T} & \boldsymbol{a}_3^\mathsf{T} & \boldsymbol{a}_4^\mathsf{T} & \boldsymbol{a}_5^\mathsf{T} \end{bmatrix}. \tag{2.14}$$

This model involves high complexity and flexibility which allows to describe any behavior of the brain.

The simulated EEG $\boldsymbol{y}_k$ is obtained from $\boldsymbol{x}_k$ using $\boldsymbol{y}_k = \boldsymbol{M}\boldsymbol{x}_k + \boldsymbol{\epsilon}_k$, where $\boldsymbol{\epsilon}_k$ is set to achieve the Signal-to-Noise Ratio (SNR) equals 7 dB. The resulting EEG signal can be seen in Fig. 2.4.

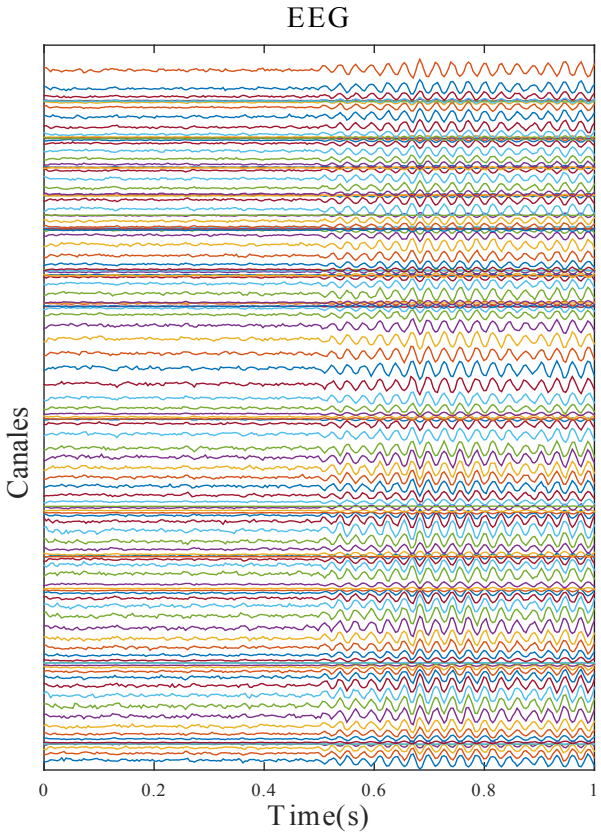

Figure 2.4: Homogeneous EEG simulation

The epileptic seizure is simulated at sample $k = 125$ ($t = 0.5\,s$) by modifying the values of a_1 from 1.0628 to 1.3, while a_2 from -0.428 to -1, but this values were fixed over 5

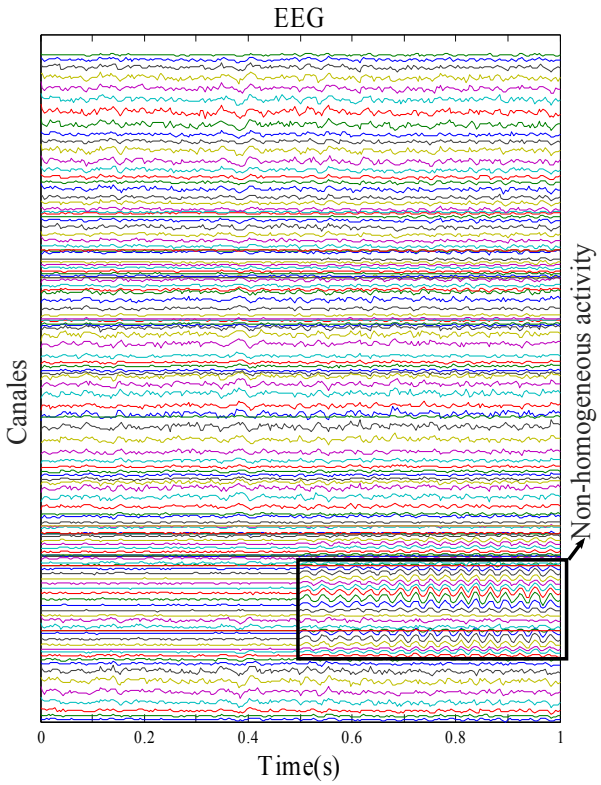

Figure 2.5: Non-homogeneous EEG simulation

regions c_k to activate a group the zones in the brain. The resulting EEG with SNR of 7 dB is showed in Fig. 2.5.

Estimation of the model parameters

With the purpose of observing the evolution in time of the parameters of both homogeneous and non-homogeneous activity models, a least square multivariable method was implemented according to [45]. This let us estimate the values of the parameters a_1 and a_2 through the temporal values obtained for the different regions c_k. Fig. 2.6 shows the parameters a_1 and a_2 or the case of homogeneous activity and we can observe how the parameters reveal a trend until 0.5s; however at the time that the instability the simulates epilepsy is introduced, these values tend to adopt the values of the instability.

For the analysis of the non-homogeneous activity, it was necessary to divide the estimation of the parameters into two parts. The first involved only the 5 regions in which the instability was applied. Fig. 2.7 shows the estimation of a_1 and a_2 for these regions, and we can observe how the trend of these values adopts the new values established to simulate epilepsy in half of the time.

On the other hand, Fig 2.8 reveals the estimated values for a_1 and a_2 in the rest of the regions, and we can observe how the values of a_1 and a_2 remain within some constant values.

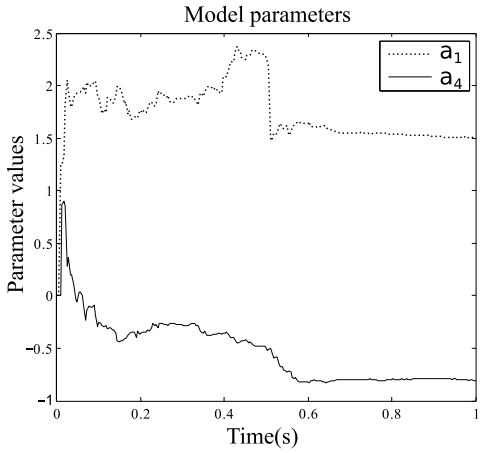

Figure 2.6: Model Parameters estimated for Homogeneous Activity

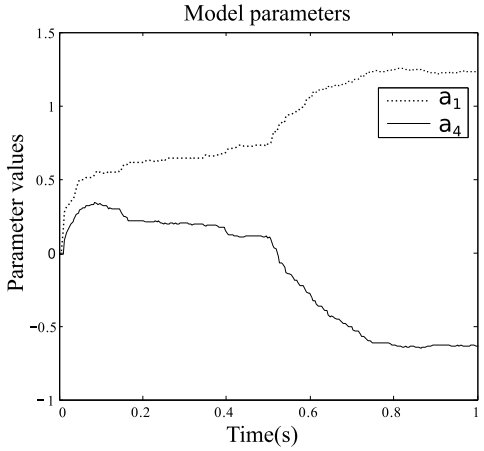

Figure 2.7: Model Parameters estimated at a Non-Homogeneous activity zone

ESL considering large scale nonlinear dynamical model:Non-homogeneous activity and ensemble Kalman Filter for state estimation

The structure used to solve the inverse problem in this case is described in Appendix. A. The model parameters were fixed and the state were estimated by using the ensemble filter Kalman (EnFK). The proposed experimental framework was the same at the one used previously and some results were the following:

The Fig. 2.9 and 2.10 show the results by estimating the location of one and three active current sources. At the top-left of the each Fig. can be seen the simulated EEG (ground truth) and the top-right is showed the location of these sources.

At the bottom-left can be seen the reconstructed activity and the temporal evolution of the estimated EEG: at the bottom-right is showed the estimation of the location for the sources.

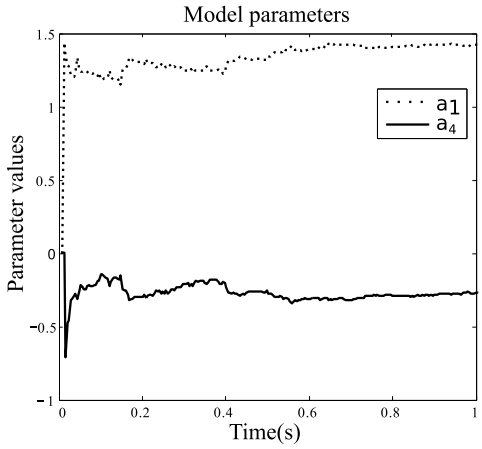

Figure 2.8: Model Parameters estimated at a Homogeneous activity zone

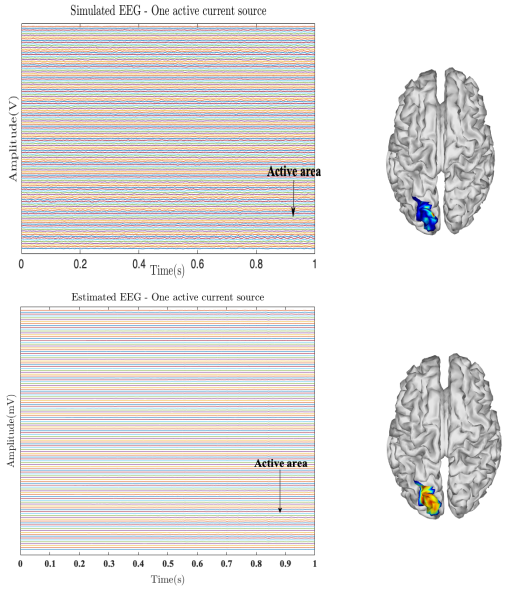

Figure 2.9: Simulation and estimation of one active source using EnKF.

2.3 Discussion

In this work was possible to establish that we may observe the brain activity generated in a specific zone by using the EEG signals obtained for the proposed model. A dynamic forward model was proposed considering a group of cortical regions with temporal evolution spatially non-homogeneous. This is a first step to analyze the focused behavior of the current sources and their temporal evolution in a specific region; usually, the main assumption is that all current sources follow the same temporal evolution over the entire brain or over a specific cortical area [7]. That is to say, brain activity follows the same temporal evolution in the whole brain or in cortical regions, this is that the activity evolves over time in spatially homogeneous way.

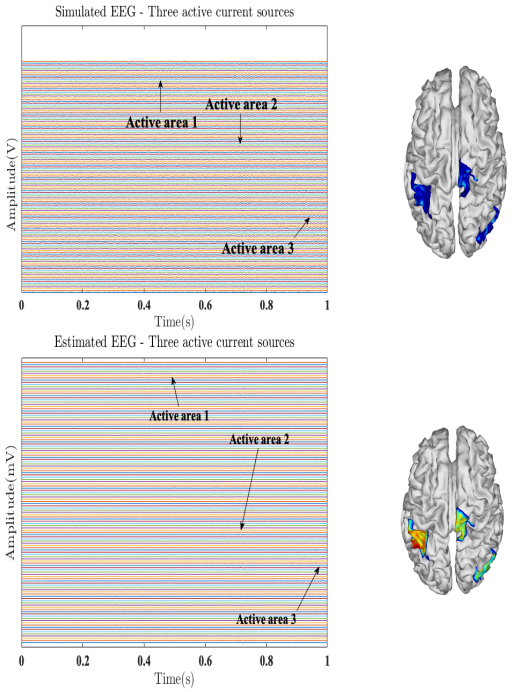

Figure 2.10: Simulation and estimation of three active sources using EnKF.

This dynamic forward model can be useful to generate focused simulations in different regions of the brain. Additionally, this will be of great use to evaluate approaches that solve the neuromagnetic inverse problem applied to the location of current sources or neural activity reconstruction.

Chapter 3

Dynamic inverse problem with frequency-spatio-temporal constraints

3.1 Introduction

The neuromagnetic inverse problem is known to be an ill-posed problem when talking about the brain activity reconstruction from EEG signals. It is characterized for having a number of known variables smaller than the number of unknown variables. For this reason, this problem can have infinitive solutions. At least for thirty years, different methods have been proposed to get an approximate unique solution. Spatial and temporal constraints have been proposed to improve the active sources localization. Nowadays, the solutions have also been addressed to concepts such as dynamics, sparsity and spatial source covariance estimation. Although these methods improve the active sources localization, these solutions have been within a spatially homogeneous framework, some works have considered that each current source evolves under its individual temporal dynamics [7], but it is necessary to estimate both the dynamics parameters and intensities of current sources to reconstruct the spatially focal current from data, this problem has many degrees of freedom and a high computational cost. Besides, frequency constraints have not been proposed directly, some works have used time-frequency transforms that allow to take in account non-stationary features of the brain activity [14]; but, some studies have showed how some diseases, cognitive processes or evoked responses could be centered in a specific frequency bands.

This chapter presents an approximate solution to reconstruct the brain activity, the method was based on a dynamic model (non linear model) with a spatio-temporal constraints in a state-space model. To reach a focused solutions, the method considers a spatialy non-homogeneous temporal evolution and according to some studies that have considered the brain activity for frequency bands, a frequency constraint was taken in

account to restrict the solution.

3.2 Frequency-Spatio-temporal constraints

Taking into account the dynamical forward model described above, the inverse problem solution to estimate the neural activity $\boldsymbol{x}_k$ could be obtained as follows:

$$\widehat{\boldsymbol{x}}_k = \underset{\boldsymbol{x}_k}{\operatorname{argmin}}\{\|\boldsymbol{y}_k - \boldsymbol{M}\boldsymbol{x}_k\|_2^2\} \tag{3.1}$$

This optimization framework can be constrained in different ways, one of them is using temporal constraints which force the solution to the inverse problem to be smooth in time. The estimated brain activity is reached as follows:

$$\widehat{\boldsymbol{x}}_k = \underset{\boldsymbol{x}_k}{\operatorname{argmin}}\{\|\boldsymbol{y}_k - \boldsymbol{M}\boldsymbol{x}_k\|_2^2 + \lambda \|\boldsymbol{x}_k - \widehat{\boldsymbol{x}}_k\|_2^2\} \tag{3.2}$$

being $\widehat{\boldsymbol{x}}_k$ the nonlinear estimation by using Eq. (2.9) as follows:

$$\begin{aligned}\widehat{\boldsymbol{x}}_k = \boldsymbol{f}\left(\widehat{\boldsymbol{x}}_{k-1}, \widehat{\boldsymbol{x}}_{k-2}, \widehat{\boldsymbol{x}}_{k-\tau}\right) = {} & \boldsymbol{A}\boldsymbol{n}_1\widehat{\boldsymbol{x}}_{k-1} + \boldsymbol{A}\boldsymbol{p}_1\widehat{\boldsymbol{x}}_{k-1} \\ & + \boldsymbol{A}_2\widehat{\boldsymbol{x}}_{k-1}^{\circ 2} + \boldsymbol{A}_3\widehat{\boldsymbol{x}}_{k-1}^{\circ 3} \\ & + \boldsymbol{A}\boldsymbol{n}_4\widehat{\boldsymbol{x}}_{k-2} + \boldsymbol{A}\boldsymbol{p}_4\widehat{\boldsymbol{x}}_{k-2} \\ & + \boldsymbol{A}_5\widehat{\boldsymbol{x}}_{k-\tau} + \boldsymbol{B}_1\widehat{\boldsymbol{x}}_{k-1}\end{aligned}$$

Besides, if it is wanted that the solution to the inverse problem being forced to have minimum energy or focal and sparse, it can be included a spatial constraint with a l_2 or l_1 norm. For those cases, the inverse problem with spatio-temporal constraints is defined by:

$$\widehat{\boldsymbol{x}}_k = \underset{\boldsymbol{x}_k}{\operatorname{argmin}}\{\|\boldsymbol{y}_k - \boldsymbol{M}\boldsymbol{x}_k\|_2^2 + \gamma \|\boldsymbol{x}_k\|_l^l + \lambda \|\boldsymbol{x}_k - \widehat{\boldsymbol{x}}_k\|_2^2\} \tag{3.3}$$

being $l = 1$ for norm l_1 or $l = 2$ for norm l_2.

The optimization methods described above have achieved good spatial results by locating active sources in the brain, but they do not take in account the non-stationary features of the brain activity [11, 12, 16, 46]. The method proposed in this work incorporates a discrete non-linear model (eq. (2.5)) to achieve that the dynamical

behavior evolves independently for each source and variant in time. Additionally, it was incorporated a spatially non-homogeneous temporal evolution to get a spatially focused solutions (eq. (2.9)). Therefore, the proposed method allows finding a focal solutions and at the same time the non-stationary activity in the brain is described by the dynamical model assessed in each iteration.

Now, frequency assumptions have been the subject in some researches, because some brain diseases or cognitive processes could be associated with some frequency [47–50]. In this case, data-driven methods can be considered to process the signals and through a feature extraction stage, looking for those frequency features associated with a specific brain activity. Hence, this work proposes a two stage optimization:

1. A frequency constraint applied over $\boldsymbol{y}_k$.
2. A spatio-temporal constraint applied over each frequency sub-space.

The minimization function is the following:

$$\widehat{\tilde{\boldsymbol{x}}}_k = \underset{\tilde{\boldsymbol{x}}_k}{\operatorname{argmin}}\{\|\tilde{\boldsymbol{y}}_k - \boldsymbol{M}\tilde{\boldsymbol{x}}_k\|_2^2 + \lambda \|\tilde{\boldsymbol{x}}_k\|_2^2 + \gamma \left\|\tilde{\boldsymbol{x}}_k - \widehat{\tilde{\boldsymbol{x}}}_k\right\|_2^2\} \tag{3.4}$$

being $\tilde{\boldsymbol{y}}_k$ the signal $\boldsymbol{y}_k$ resulting of the optimization process related to the frequency constraint where the entropy is used for selection of frequency bands, and $\tilde{\boldsymbol{x}}_k$ the estimated activity constrained in frequency.

$$\tilde{\boldsymbol{y}}(t_k) = \sum_{i \in O} \boldsymbol{\alpha}_i(t_k) \tag{3.5}$$

being $\boldsymbol{\alpha}_i(t_k)$ the projection in a frequency band.

In terms of the MSP solution of (3.6), the following estimation equation can be obtained:

$$\widehat{\tilde{\boldsymbol{x}}}_k = \boldsymbol{Q}\boldsymbol{M}^\top(\boldsymbol{\Sigma}_\epsilon + \boldsymbol{M}\boldsymbol{Q}\boldsymbol{M}^\top)^{-1}\tilde{\boldsymbol{y}}_k \tag{3.6}$$

Two proposed approaches are presented for frequency bands selection:

- Multi-signal Wavelet-packets (MWP)
- Empirical Mode Decomposition (EMD) and Multivariate Empirical Mode Decomposition (MEMD)

3.3 Brain activity reconstruction using Wavelets Packets

3.3.1 Forward problem for EEG generation

Consider the forward problem for iterative EEG generation described in eq. (2.1), where $\boldsymbol{y}_k$ is the EEG and $\boldsymbol{x}_k$ is the source activity at time sample k. This EEG generation can also be represented as:

$$\boldsymbol{Y} = \boldsymbol{M}\boldsymbol{X} + \boldsymbol{\Upsilon} \tag{3.7}$$

where $\boldsymbol{Y}$ is a subspace of the corresponding $\boldsymbol{y}_k$ segment of EEG, $\boldsymbol{X}$ is the subspace of the corresponding $\boldsymbol{x}_k$ segment of neural activity and $\boldsymbol{\Upsilon}$ is the subspace of the corresponding $\boldsymbol{\upsilon}_k$ (measurement noise Gaussian with mean zero and known covariance) for $k = 1, \ldots, N$.

3.3.2 Multi-signal Wavelet Packet

Multi-signal Wavelet Packet (MWP) decomposition was used to project the EEG matrix $\boldsymbol{Y}$ in several sub-spaces $V_{(j,i)}$, being $j = 0, \ldots, J$ the number of decomposition levels, and $i = 0, \ldots, 2^j - 1$ the number of sub-bands of each level, which satisfies that: $V_{(j,i)} = V_{(j+1,2^i)} \oplus V_{(j+1,2^i+1)}$. The approximated reconstruction of the signal can be achieved using the best tree criteria with a reduced number of subspaces. These subspaces can be chosen by any cost function, for example an entropy based cost function. Also an approximated reconstruction can be obtained based on the amount of retained energy, as following:

$$\widehat{\boldsymbol{Y}} \approx \sum_{j \in E} \tilde{\boldsymbol{Y}}_j \tag{3.8}$$

being E the subset of subspaces which retained energy is over a threshold, and being $\tilde{\boldsymbol{Y}}_j$ the $j - th$ subspace projected in the same space of $\boldsymbol{Y}$.

Also, a subspace representation of the (3.7) can be defined as follows:

$$\boldsymbol{Y}_j = \boldsymbol{M}\boldsymbol{X}_j + \boldsymbol{\Upsilon}_j \tag{3.9}$$

which means that each j projection of the $\boldsymbol{Y}$ can be related directly to a projected activity $\boldsymbol{X}_j$, where:

$$\boldsymbol{X} = \sum_{j=0}^{J} \tilde{\boldsymbol{X}}_j \tag{3.10}$$

It can be seen that the subspace $\boldsymbol{X}_j$ must be projected into the original subspace $j = 0$ ($\tilde{\boldsymbol{X}}_j$), as mentioned in (3.8). Also, an approximated reconstruction can be obtained based on the amount of retained energy of each subspace as follows

$$\widehat{\boldsymbol{X}} = \sum_{j \in E} \tilde{\boldsymbol{X}}_j \tag{3.11}$$

being $\tilde{X}_j$ the projection of neural activity in the j-th subspace, and $\widehat{\boldsymbol{X}}$ the approximated reconstruction of neural activity. Two possibilities for analysis of neural activity: the first one is the brain mapping obtained in $\widehat{\boldsymbol{X}}$ where the proposed method includes a combination of the relevant information on several subspaces according to an entropy based cost function. The second one is the brain mapping obtained in $\tilde{\boldsymbol{X}}_j$ where the proposed method splits the information of each sub-band. Therefore, an analysis by relevant sub-bands or by a combination of relevant sub-bands can be performed.

3.3.3 Inverse subspace problem

By considering (3.9), the solution a inverse problem based on a subspace description of the EEG, can be obtained as follows:

$$\underset{\boldsymbol{X}_j}{\text{minimize}} \quad \|\boldsymbol{Y}_j - \boldsymbol{M}\boldsymbol{X}_j\|_2^2 \tag{3.12a}$$

$$\text{subject to} \quad \|\boldsymbol{X}_j\|_1^1 \tag{3.12b}$$

$$\left\|\boldsymbol{X}_j - \widehat{\boldsymbol{X}}_j\right\|_2^2 \tag{3.12c}$$

where the solution is the reconstructed activity $\widehat{\boldsymbol{X}}_j$. It can be seen that the optimization problem (3.12) is solved for each subspace. Since this is a multi-signal multilevel decomposition, it can be seen that $\boldsymbol{Y}_j$ holds the same number of channels (rows) for each level that the original EEG $\boldsymbol{Y}$, but the number of columns (time samples) is down-sampled by a factor of 2^j according to the depth of decomposition. Therefore, the reconstructed activity $\widehat{\boldsymbol{X}}_j$ holds the same properties of $\boldsymbol{Y}_j$, which means that the number of sources is hold, but the time resolution is down-sampled.

3.3.4 Experimental framework

Two methods for brain activity reconstruction are compared in this work, Multiple Sparse Priors (MSP) [15] and IRA-L1 [16], the performance is compared with MWP

decomposition using the best tree and without MWP decomposition. The results are analyzed for both simulated and real EEG signals.

1. **Simulated active sources**. An analysis of the subspace mapping is performed with simulated EEG signals by considering the underlying neural activity known and by selecting, randomly, the location of the active sources in the brain. Two considerations for underlying activity dynamics as follows:

   (a) *Database 1.* According to [51], two sources in the range of 8 to 13Hz were randomly located in the brain as alpha oscillations and with activity $\boldsymbol{X}$ sampled to 100Hz. Besides, independent brain noise time series were generated and randomly located at 500 locations whose main feature was 1 / f-shaped (pink noise) power and random phase spectra. These noise sources were distributed from the entire cortical surface and the EEG signals and the EEG signal $\boldsymbol{y}_k$ was generated by multiplying the neural activity $\boldsymbol{x}_k$ with the leadfield matrix $\boldsymbol{M}$ as described in eq. (3.7). The signal-to-noise (SNR) parameter is drawn uniformly from the interval $[0.1, 0.9]$.

   (b) *Database 2.* Three sources were activated according to the following expression: $x_i(t_k) = \exp\left(-\frac{1}{2}\left(\frac{t_k - c_i}{\sigma}\right)\right)^2 \sin\left(2\pi f_i t_k\right)$, being c_i the center of the windowed signal in seconds, and f_i the frequency of the signal, with $i = 1, \ldots, 3$. The c_i and f_i were selected in the following ranges $c_i : [0.5, 1.5]$ seconds and randomly in $f_i : [1, 20]$ Hz. In order to measure the performance of the method for several randomly selected source positions and robustness, 300 trials (60 for each SNR) with SNRs (0, 5, 10, 15 and 20dB) [16]. As described in eq. 3.7, the EEG was generated by multiplying $\boldsymbol{X}$ by the lead field matrix $\boldsymbol{M}$.

   The lead-field matrix used to generate the EEG signals for both databases is obtained from the so-called New York Head model as used in [51]. This head model combines a highly detailed magnetic resonance (MR) image of the average adult human head with state-of-the-art finite element electrical modeling. The model holds $n = 2004$ sources and $d = 108$ electrodes.

2. **Real EEG signals**. The methods IRA-L1 and MSP with and without the MWP decompositions are evaluated using real EEG signals, where the ground truth is assumed relying upon multi-modal solutions. The paradigm has been set up by [52], where eighteen healthy young adults (eight female) were drawn from the MRC Cognition and Brain Sciences unit Volunteer Panel. In this paradigm were used 300 different faces (150 were from famous people and 150 were from unfamiliar (previously unseen) people) and 150 different scrambled faces. The faces or scramble faces were presented in a repeated way or after a lag of 5-15 intervening items. Finally, ERP of 15 subjects are selected for each one of the 3 stimulus and it is important that each subject has his own forward model (lead-field matrix).

3.3.5 Performance measure

To measure the performance of the proposed algorithms (IRA-L1 [16] and MSP [15]) used was the Wasserstein metric, also termed the Earth Mover's Distance (EMD). The EMD is a measurement of the amount of energy required to move the estimated brain mapping solution to the original simulated neural activity [16].

3.3.6 Results

The temporal (left) and frequency (right) dynamics of the simulated sources on the Database 1 are showed in fig. 3.1. It can be seen that the source activity is mainly concentrated in the range of 8 to 13Hz. It means that the relevant information should be able to localize the main EEG generators inside such frequency range.

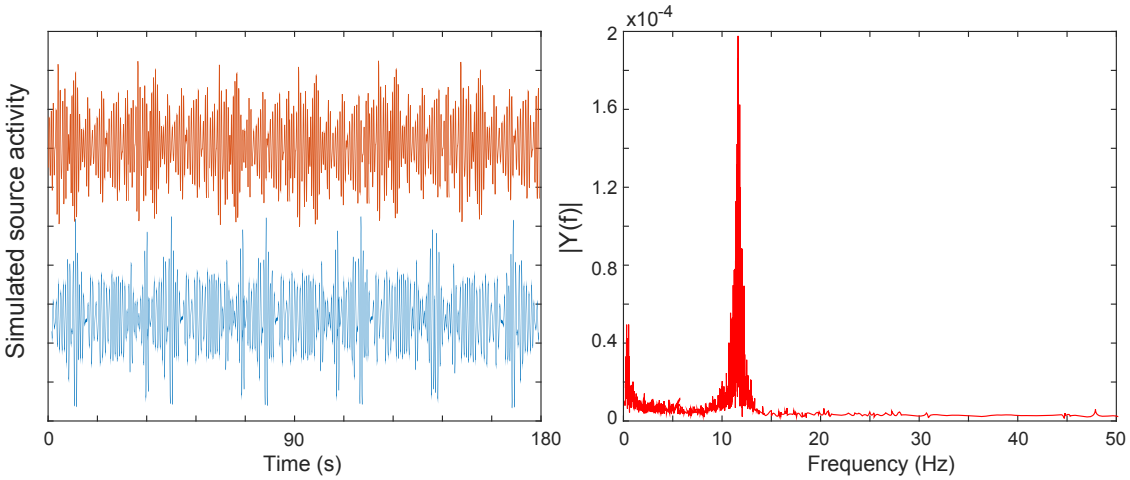

Figure 3.1: Simulated EEG for two sources according to the Database 1

The MWP decomposition, for the database above mentioned is showed in fig. 3.2. It should be highlighted that almost 90% of the EEG total energy is retained in subspaces $\boldsymbol{V}_{(4,2)}$ and $\boldsymbol{V}_{(4,3)}$, these subspaces (6.25 and 12.5 Hz) are within the frequency range of the activity simulated. Therefore, the EEG recording $\boldsymbol{Y}$ is projected into several sub-spaces $\boldsymbol{V}_(j,i)$, being $j = 0, \cdots, J$ the number of decomposition levels, and $i = 0, \cdots, 2^j - 1$ the number of sub-bands for each level. As a result, we obtained that the EEG recording can be decomposed into the following subspaces: $V_{(0,0)} = V_{(1,1)} \oplus V_{(2,1)} \oplus V_{(3,0)} \oplus V_{(4,2)} \oplus V_{(4,3)}$.

The fig. 3.3 shows an example of three simulated non-stationary sources and the obtained EEG for the second database. In this case, the sources were centered in the following frequencies: $4Hz$ (red), $10Hz$ (blue), and $16Hz$ (orange).

More than 90% of the total EEG energy was covered for the sub-spaces $\boldsymbol{V}_{(4,1)}$, $\boldsymbol{V}_{(4,2)}$, and $\boldsymbol{V}_{(4,6)}$ with central frequencies of 6.25, 9.375, and 18.75 Hz (3.4) after the sig-

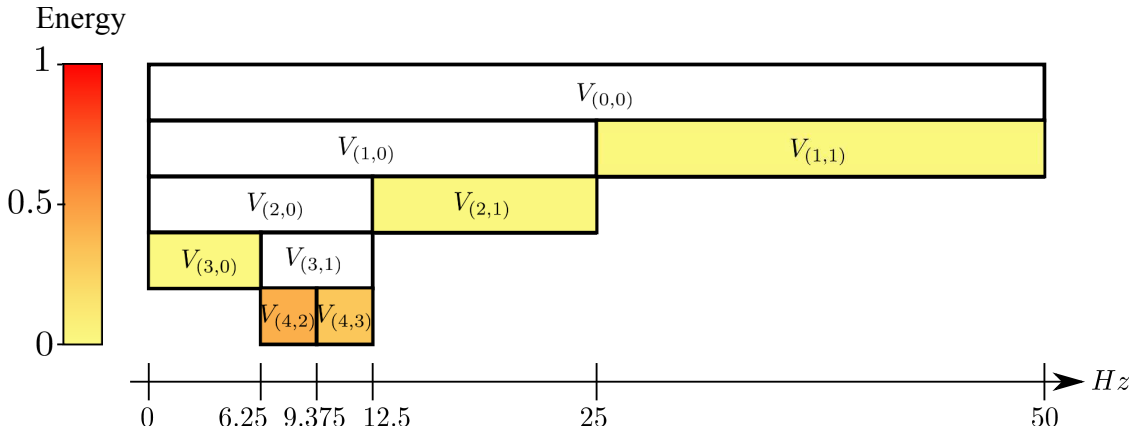

Figure 3.2: Best tree selection by using Shannon entropy from MFB decomposition

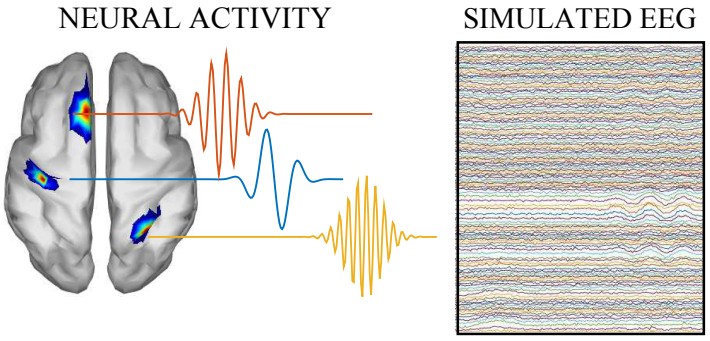

Figure 3.3: EEG and three active sources randomly located with different frequencies.

nal was decomposed by using MWP. It must be remarked that the obtained results of each subspace directly correspond to each simulated active source. Therefore, the proposed method is able to optimally estimate the frequency bands of interest, under non-stationary conditions.

In fig. 3.5 can be seen the Wasserstein metric mean and standard deviation after 60 repetitions at each SNR level for the proposed algorithm with the database 2. The locations and the central frequency are randomly selected for each repetition. The best neural activity reconstruction were reached by applying the methods with the MWP decomposition step. It must be highlighted that the results with IRA-L1-MWP overcomes the remaining comparison methods (case with non-stationary sources). IRA-L1-MWP deals with the data non-stationarity in two different ways: i) by splitting the time-varying EEG spectrum into several sub-spaces using the MWP step, and ii) by imposing smooth temporal transitions within the estimated sources, yielding an improved non-stationary source reconstruction.

For real EEG database, the ground truth used as estimated reference activity was EEG and MEG multimodal data. The neural activity was estimated for each of the three stimulus conditions, namely, faces, famous faces, and scrambled faces; and for each methods to the averaged ERP time series of each subject. Therefore, with these estimations was possible to calculate the Wasserstein metric between the ground truth

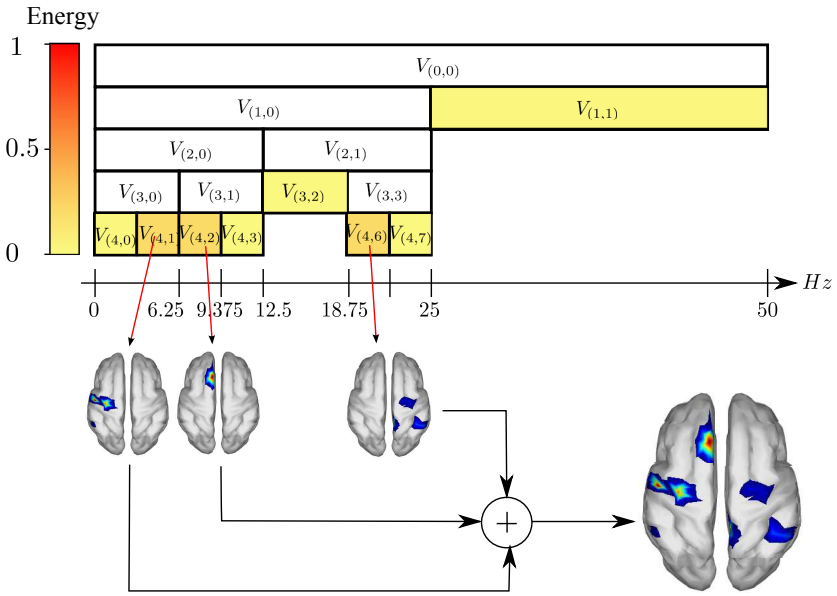

Figure 3.4: MFB decomposition for three sources

and the active sources with each activity estimation algorithm. The Fig. 3.6 shows the Wasserstein metric mean and standard deviation for the 15 subjects under each stimulus condition and, the best results (the lower Wasserstein metric) were obtained by the methods with the MWP step, hence, it means closer reconstruction to the ground truth. Furthermore, as ERPs comprise non-stationary brain activity, IRA-L1-MWP achieves the best performance.

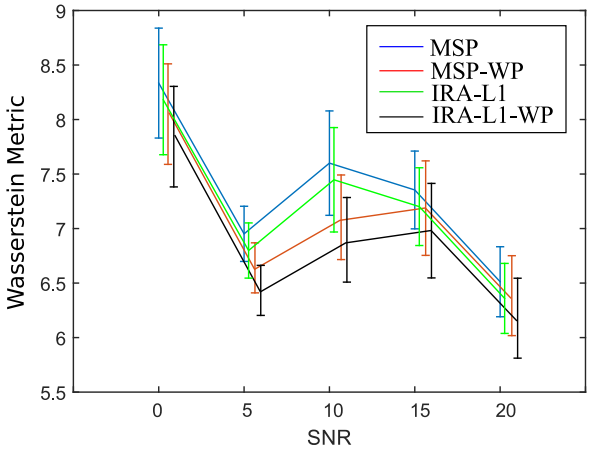

Figure 3.5: Setup 2 EMD (Wassertein metric) comparison for 60 repetitions of three randomly located sources at each SNR level

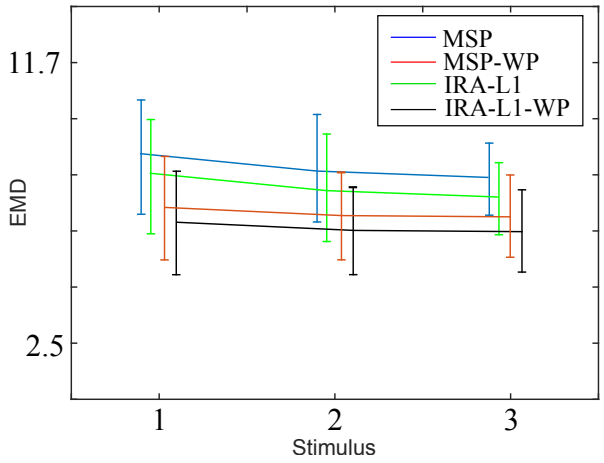

Figure 3.6: EMD (Wassertein) measure assuming multimodal solution as the ground truth.

3.4 Brain activity reconstruction using Empirical Mode Decomposition (EMD)

Empirical Mode Decomposition has been proposed as an adaptive time-frequency data analysis method in [53]. EMD does not require any restrictive assumption on the underlying model of the process/system under analysis and it is able to handle both non-linear and non-stationary signals. However, the algorithm has showed to have some limitations in identifying closely spaced spectral tones and components appearing intermittently in the signal ([54]). The aim of the EMD method is to decompose the nonlinear and non-stationary signal $y(t_k)$ into a sum of intrinsic mode functions (IMFs) that satisfies two conditions ([55]):

1. Symmetric upper/lower envelopes (zero mean).
2. The numbers of zero-crossing and extrema that are either equal or differ by exactly one.

The EMD algorithm for the signal $y(t_k)$ can be summarized as follows and it can be seen in fig. 3.7 [56] :

1. Identify all extrema (maxima and minima) in $y(t_k)$.
2. Interpolate between minima and maxima, generating the envelopes $e_l(t_k)$ and $e_m(t_k)$.
3. Determine the local mean as $m(t) = (e_l(t_k) + e_m(t_k))/2$.
4. Obtain the residue $r(t_k) = y(t_k) - m(t_k)$

5. Decide whether $r(t_k)$ is an IMF or not based on the two basic conditions for IMFs mentioned above.

6. Repeat step 1 to 4 until $r(t_k)$ will be monotonic.

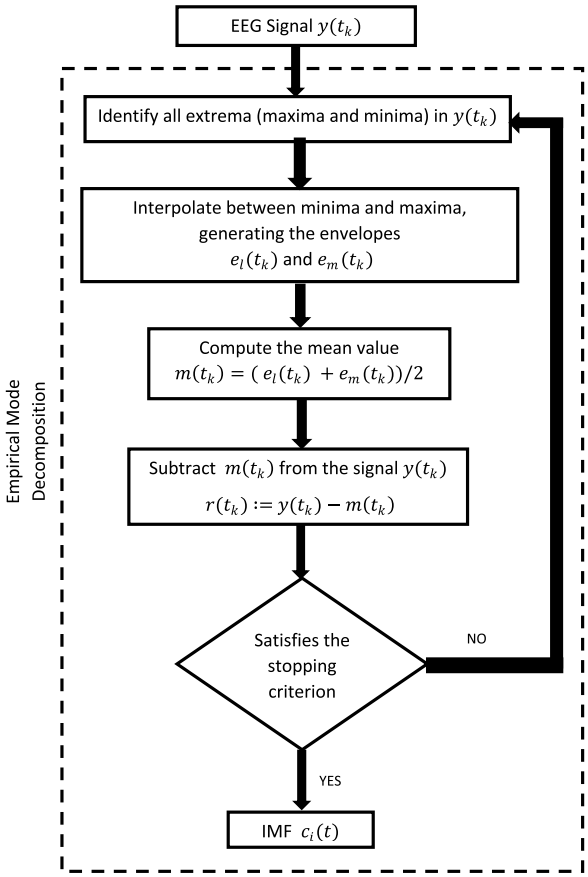

Figure 3.7: Flowchart indicating the various stages of the EMD method

Empirical Mode Decomposition is applied over $\boldsymbol{y}(t_k)$ to obtain $\boldsymbol{\alpha}_i(t_k)$ being i the intrinsic mode function (IMF), and

$$\boldsymbol{y}(t_k) = \sum_{i=1}^{N} \boldsymbol{\alpha}_i(t_k) + \boldsymbol{r}(t_k) \tag{3.13}$$

where N is the number of IMFs and $\boldsymbol{r}(t_k)$ a residual. Recently, some optimization techniques have been proposed to improve the performance of the EMD [57, 58].

Having obtained the intrinsic mode function components, we can apply the Hilbert transform to each component, and compute the instantaneous frequency according to Eq. (3.14).

$$f_i(t) \triangleq \frac{1}{2\pi} \cdot \frac{d\theta_i(t)}{dt}, \tag{3.14}$$

where $\theta_i(t)$ is the instantaneous phase of each IMF calculated from the analytical signal associated [59]. Finally, the instantaneous frequency can be observed in the Hilbert Spectrum.

The EMD method is limited by the *Mode Mixing* problem. This problem arises when EMD is applied to a signal that exhibits intermittency and/or involves components with spectral proximity [60, 61] and [62]. In a report of [63], a rigorous mathematical analysis shows how EMD behaves in the case of a composite two-component signal, explaining the roots of one type of mode-mixing problem, spectral proximity mode mixing. This study identified the frequency-amplitude region within good separation can be achieved with EMD and the region where mode mixing occurs. However, a solution that offers good IMF separation has not been available for signal components that reside within the same octave. [62] recently proposed a masking signal-based method to separate spectral components that reside within the same octave. In contrast to the guidelines presented in [61] for selecting the amplitude and frequency of the masking signal, precise amplitudes and frequencies are defined by the boundary map presented in [62] to reverse a mode-mixing condition.

On part of this work was addressed the influence of the mode-mixing problem on the detection of signal sources from various regions in the brain using information from EEG, decomposed with EMD. After analyzing simulated and real brain signals, it detected two types of concurrent mode mixing: one caused by the presence of signal components residing within the same octave (spectral proximity mode mixing) and the other by the presence of intermittency. EMD and EMD with masking have different scopes and capabilities. The ensemble empirical mode decomposition (EEMD) method was designed to separate components that are mixed due to the presence of intermittency in the signal, which is the root cause of the "split-mode mixing" problem [60]. The EEMD method cannot separate signals that reside within the same octave (spectral proximity mode mixing). Therefore, it was analyzed the brain activity reconstruction using variants of EMD to process the EEG signals.

The simulated neural activity with its temporal and spatial evolution is showed Fig. 3.8a, the simulated EEG for an SNR of 10dB is showed in Fig. 3.8b. The IMFs obtained for one of the 30 channels with the EMD proposed in [53], the masking signal from [61] and the EEMD proposed in [60] are showed in Fig. 3.8c, 3.8d and 3.8e respectively.

The EMD in Fig. 3.8c has a clear mode mixing. Simple inspection of the instantaneous frequency reveals two frequency components (8Hz at $t = 2$s, and 10Hz at $t = 3$s) in the first IMF. The other two IMFs show the 4 Hz source at $t = 1$s but in general they provide limited information as the instantaneous frequency is strongly fluctuating. Using the masking signal, in Fig. 3.8d is possible to distinguish more clearly the three different frequencies that appear in the first IMF (4, 8 and 10Hz). Parts of the 4Hz source at $t = 1$s appears also in IMF2 and IMF3. Although the mode mixing persists, it is possible to clearly identify in the first IMF the instant in which each component appears. When the EEMD is applied for decomposition, it is possible to observe that all the information of interest is contained in the second and third IMFs (Fig. 3.8e)

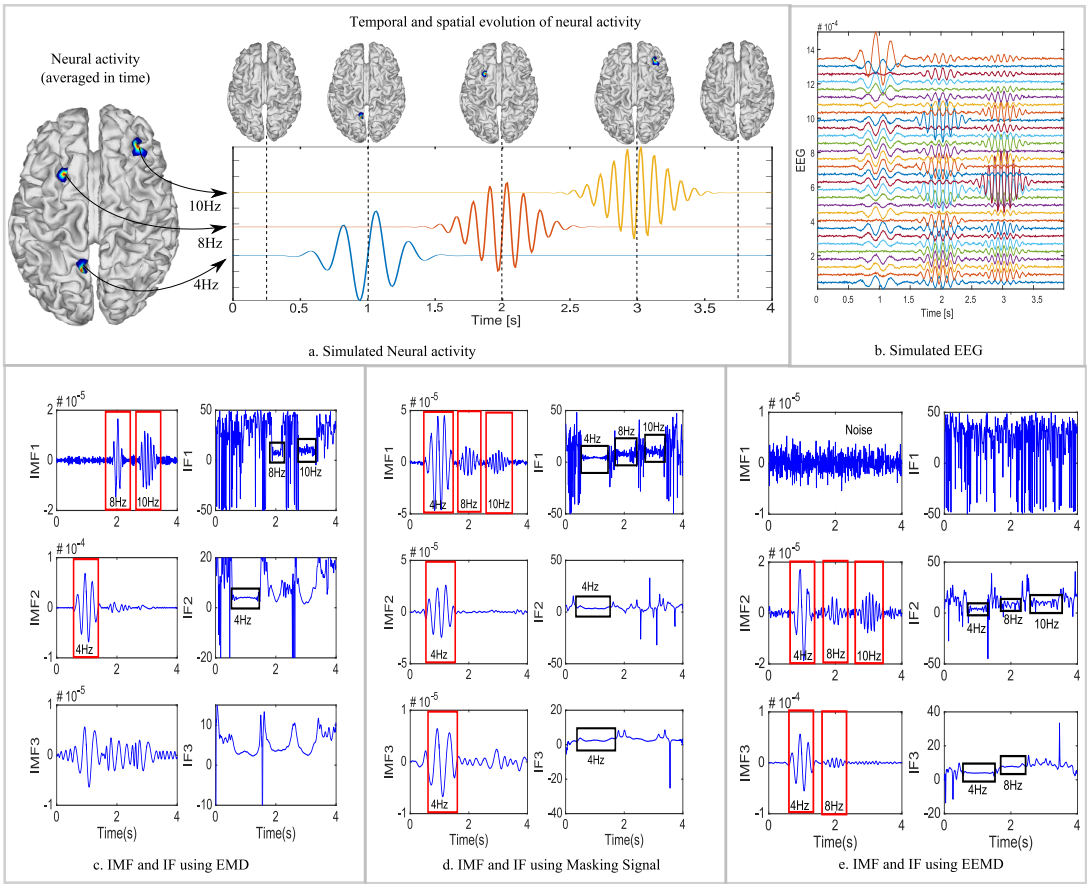

Figure 3.8: EMD

while the additive noise appears in the first IMF.

In Fig. 3.9 the temporal and spatial evolution of brain activity (during five time instants) and its average over time are showed for the following cases: ground truth, MSP, MSP with EMD, MSP with Masking Signal and MSP with EEMD. In addition, the reconstruction performance in terms of the Wasserstein metric is showed in Fig. 3.9f. Fig. 3.9a shows the spatial and temporal evolution of ground truth neural activity and its average over time, where the windowed activity of the source at 4 Hz appears at time $t = 1$ second, and the windowed activity of the sources at 8 Hz and 10 Hz appears at $t = 2$ seconds and $t = 3$ seconds respectively. The full reconstruction of the brain activity using MSP can be seen in the Fig. 3.9b. The partial reconstruction of the brain activity using MSP with EMD from data obtained from IMF 1 (top in the Fig. 3.9c) and IMF 2 (bottom in the Fig. 3.9c) can be seen in the Fig. 3.9c. It is worth noting that the 2 IMFs were obtained after applying EMD to the simulated EEG signals.

In the same way, Fig. 3.9d and Fig. 3.9e, shows the partial brain reconstructions obtained after applying MSP to IMFs obtained from EMD with masking (IMF 1) and EEMD (IMF 2) respectively. The performance of the reconstruction in terms of the Wasserstein metric is presented in Fig. 3.9f. According to the Wasserstein metric, the best approximations were obtained using Masking Signal (Fig. 3.9e) and EEMD

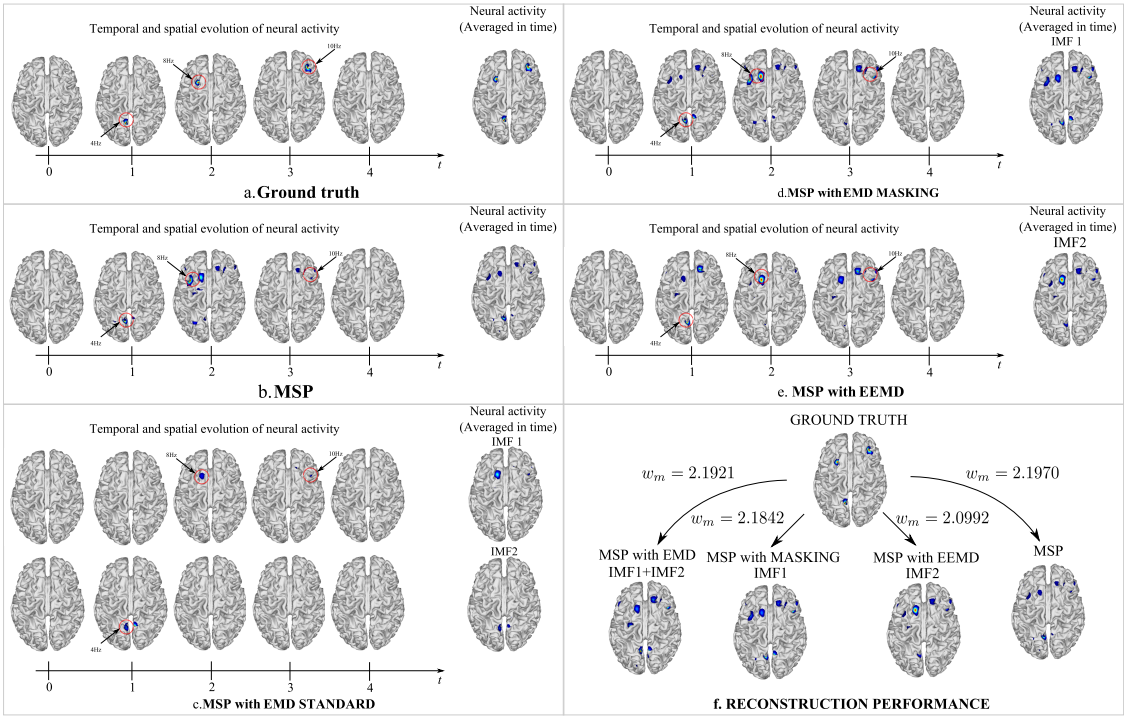

Figure 3.9: EMD

(Fig. 3.9f). In both cases, the three components were identified in different IMFs (IMF 1 for the EMD with masking, and IMF 2 for the EEMD).

It is noticeable that the temporal and spatial evolution of neural activity showed for each discussed model in Fig. 3.9, are consistent with the temporal evolution of the brain activity as well as the temporal behaviour of the IMFs presented in Fig. 3.8.

Multivariate Empirical Mode Decomposition (MEMD) has been reported to handle adequately the mode-mixing problem in multi-channel data analysis and is therefore an ideal candidate for application in multi-channel EEG signal analysis ([55]).

3.5 Brain activity reconstruction using Multivariate Empirical Mode Decomposition

The main purpose of the EMD algorithm is to process the original signal and calculate its local mean. The critical step during this process is to find the local extrema. If it is necessary to process multivariate signals, the first option is to apply EMD to each channel to obtain the IMFs for each one, but multivariate data are characterized by generalized oscillations (joint rotational modes), which must be treated consistently to reach a meaningful estimated T-F [64].

Univariate EMD can be applied channel-wise if the channels are not strongly coupled,

but this approach may hide certain information and has the following limitations [65]:

1. Non-uniform signals: standard EMD can not always guarantee the same number of IMFs for each channel.
2. Scale alignment: it is not possible to guarantee that the corresponding scales have the same modes.
3. To constrain the number of IMFs for every channel could compromise T-F estimation; it is the nature of IMFs to vary in number.

The signal in EMD is the sum between a slow and a fast oscillation, whereas the signal in the MEMD method is the result of the sum of a slow rotation and fast rotation. Therefore, MEMD decomposes the multivariate signal in p-variate signals $s(t)$ as:

$$\boldsymbol{s}(t) = \sum_{m=1}^{M} \boldsymbol{c}_m(t) + \boldsymbol{r}(t) \tag{3.15}$$

in which $\boldsymbol{s}$, $\boldsymbol{c}$, $\boldsymbol{r} \in \mathbb{R}^p$. In this case, the *p-variate IMFs* ($\boldsymbol{c_m}$) are the joint rotational modes and $\boldsymbol{r}$ is the residual.

To analyze a true signal using EMD, it is necessary to compute the local mean by interpolating among local minima and maxima to calculate the mean of the upper and lower envelopes. Nevertheless, the use of *oscillatory modes* for multivariate signals is a confusing concept for the definition of their IMFs, because the local maxima and minima can not be defined directly. The solution has been to propose a method to generate multiple n-dimensional envelopes, which are computed using the projections of the signal over different directions in n-dimensional space. These projections are then averaged to calculate the local mean [64]. Therefore, Multivariate Empirical Mode Decomposition works as follows (MEMD algorithm) [65]:

1. The *V-point* Hammersley sequence is generated for uniformly sampling a p-dimensional sphere.
2. For each vector $\mathbf{x}_{\theta_v}$, projections $q_{\theta_v}(t)$ of the signal $s(t)$ will be calculated with the same orientation, therefore a set of projections $\{q_{\theta_v}(t)\}_{v=1}^{V}$ will give for $v = 1, ..., V$
3. Find the time instants $\{t^i_{\theta_v}\}_{v=1}^{V}$ that correspond to the maxima of the set of projections of signals $\{q_{\theta_v}(t)\}_{v=1}^{V}$.
4. Interpolate $[t^i_{\theta_v}, s(t^i_{\theta_v})]$ to obtain the envelope curves $\{e_{\theta_v}(t)\}_{v=1}^{V}$.
5. the mean of the P multidimensional envelopes is calculated

$$\boldsymbol{m}(t) = \frac{1}{V} \sum_{v=1}^{V} \boldsymbol{e}_{\theta_v}(t) \tag{3.16}$$

6. Extract the "detail" $d(t) = s(t) - m(t)$. If $d(t)$ fulfills the stoppage criterion for a multivariate IMF, apply the above procedure to $s(t) - d(t)$. Otherwise repeat for $d(t)$.

3.5.1 Experimental setup

The solution for the neuromagnetic inverse problem was assessed using EEG signals, by performing simulations with several scenarios for which the brain activity is known. Therefore, it was necessary to use a lead field matrix (head model, preferably a realistic representation) that allows the generation of EEG signals with active sources in predefined or random positions, with specific activity function.

The head model used to generate the synthetic EEG signals can be found in the *Multimodal Face Dataset* at `http://www.fil.ion.ucl.ac.uk/spm/data/mmfaces/` of SPM software. This dataset was obtained using the same paradigm reported in [66] and contains EEG, MEG, and fMRI data for one subject. This paradigm has been used in several studies for source reconstruction and applied to evoked responses ([17, 31, 52, 67–69]). The head model contains a cortical mesh with 8196 vertices as distributed sources and relates them to 128 electrodes. However, the number of channels was reduced to 8, 16 and 32 (Fig. 3.10). This reduction was carried out to analyze the quality of the reconstruction vs the number of measurements.

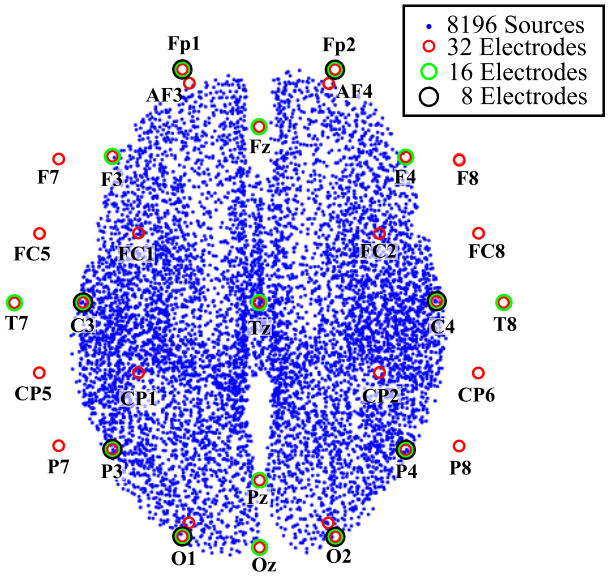

Figure 3.10: Three configurations of electrode positions for EEG measurements

Nine EEG signal configurations were tested with three different numbers of active sources: 1, 3, and 5. For each number of active sources, the synthetic EEG was generated considering 8, 16 or 32 electrodes. One of its goals, was to show that MEMD can reduce the mode-mixing generated in the process of obtaining the IMFs. MEMD allows better selection of the frequencies inside the IMFs. The source activity for 1, 3,

and 5 active sources was thus simulated at various frequencies and in various instants of time and various levels of measurement resolution, i.e. 8, 16, and 32 channels (Fig. 3.10).

1. **Simulated EEG**. The brain activity was simulated for each source using a windowed sinusoidal activity, as follows:

$$x_i(t_k) = e^{-\frac{1}{2}(\frac{t_k - c_i}{\sigma_i})} sin(2\pi f_i t_k) \tag{3.17}$$

The signals were generated in a time interval from 0 to 6s with a sample frequency f_s of $200Hz$. The activity frequencies were selected within the typical ranges for brain frequencies, e.g., *alpha* or *beta* brainwaves, to generate a realistic scenario. In addition, in the cases of three and five active sources, certain sources were located at low brain frequencies, e.g., *theta* or *delta*, to observe the performance of MEMD for several frequency ranges. For the case of one active source, the activity was generated in $t = 1s$, with $f = 10Hz$ and the active source was located as it is seen in the Fig. 3.11a.

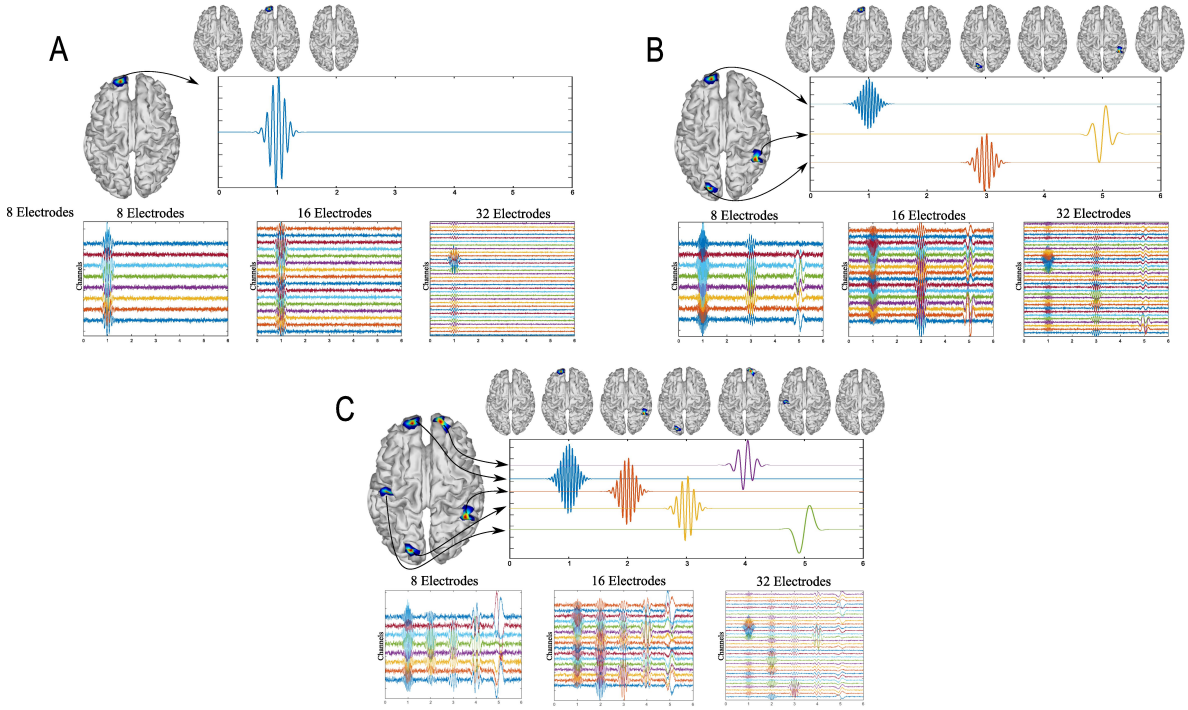

Figure 3.11: Simulated activity for one source **(A)** using 10Hz and 32, 16, or 8 EEG channels. Simulated activity for three sources **(B)** using 4, 12, and 20Hz windowed sinusoidal activity and 32, 16, or 8 EEG channels. Simulated activity for five sources **(C)** using 2, 6, 10, 15, and 20Hz windowed sinusoidal activity and 32, 16, or 8 EEG channels

For three and five active sources, the activities were simulated at different instants of time. For three active sources, the first activity was generated at the source

located at position 4000 at $t = 1s$ at $f = 20Hz$, for the second source, it was located at position 5020 at $t = 3s$ at $f = 12Hz$, and for the third source at position 150 at $t = 5s$ at $f = 4Hz$.

Finally, for five active sources, the signals were generated and centered at times $t = 1, 2, 3, 4$ and 5s, at $f = 20Hz$ at position 4000, $f = 15Hz$ for position 5020, $f = 10Hz$ at position 150, $f = 6Hz$ at position 8100, and $f = 2Hz$ at position 2200 (Fig. 3.11c).

Common evaluation of inverse problem solutions is generally performed using simulated sources for which the underlying activity is known. Here, it was used simultaneous simulated sources with sinusoidal activity to evaluate the performance of MEMD in terms of its ability to separate source activity in the frequency domain. Thus, simulated EEG activity was obtained for 1, 3 and 5 sources that were spatially and temporally located at different points. Source frequencies (f_i) in the range of 2 to 20Hz were tested and the temporal localization of sources was in the range of 1 to 5s. Source reconstruction was performed in two ways: 1) using MSP directly from the synthetic EEG without any pre-processing step, such as the use of raw signals, and 2) using MEMD prior to MSP, in which the main IMFs were selected in a manually way but according to the energy and entropy values.

The simulating procedure started with the generation of each source, using the windowed sinusoidal activity. The active sources were located in predetermined locations, the activity $\boldsymbol{x}(t_k)$ was calculated, and the synthetic EEG was then obtained using eq. (2.1). Then, noise was added to the EEG signal $\boldsymbol{y}(t_k)$, with a signal-to-noise ratio of $SRN = 10$dB. Three configurations were considered for the measurements: 32, 16, or 8 EEG channels. A reduced lead field matrix was used for each synthetic EEG for each number of channels to perform the brain mapping and the source reconstruction was then calculated directly using MSP (raw MSP) and applying MEMD to the electrode space (MEMD-MSP). Finally, the reconstructions were compared to a spatial accuracy measurement by mean of Wasserstein metric (Wm).

3.5.2 Real EEG Signals Database

A multi-subject, multi-modal human neuroimaging dataset was used to evaluate the MEMD method and its application to real EEG signals. The experiment included 16 participants for whom the stimuli consisted of images projected onto a screen [70]. Three types of stimuli were tested: familiar faces (famous), unfamiliar faces (non-famous), and scrambled faces. The study used EEG, MEG, and fMRI to estimate neural activity and its location over the cortical areas of the brain by applying a multi-modal technique reported by [52]. The EEG recordings were taken using 70 AgCl electrodes and a layout according to the 10-10 system. Each subject in the dataset has their own head model and their ground truth activity. The lead field matrix that modeled the head conductivity was made using 8196 distributed sources. The lead field matrix was used to solve the inverse problem and the ground truth activity was used to compare the

solutions obtained with the MEMD method a *priori* information for the MSP and that obtained using the raw EEG data directly for the MSP. The dataset contains the event related potentials (ERPs) of the experiment. The ERPs were considered around 170ms (the N170 component) for the experiments with scrambled and familiar faces. In addition, the number of channels were reduced from 70 to 32, 16, or 8, as for the simulated data, to evaluate the performance of the brain mapping solution with MSP using one or several IMFs from MEMD and compare the results with those for MSP with raw data. The activity was evaluated around the N170 component by establishing a region of interest ROI, as in [52], in the window between 100 and 220ms. The methodology followed for processing the high-density data is presented in Fig. 3.12.

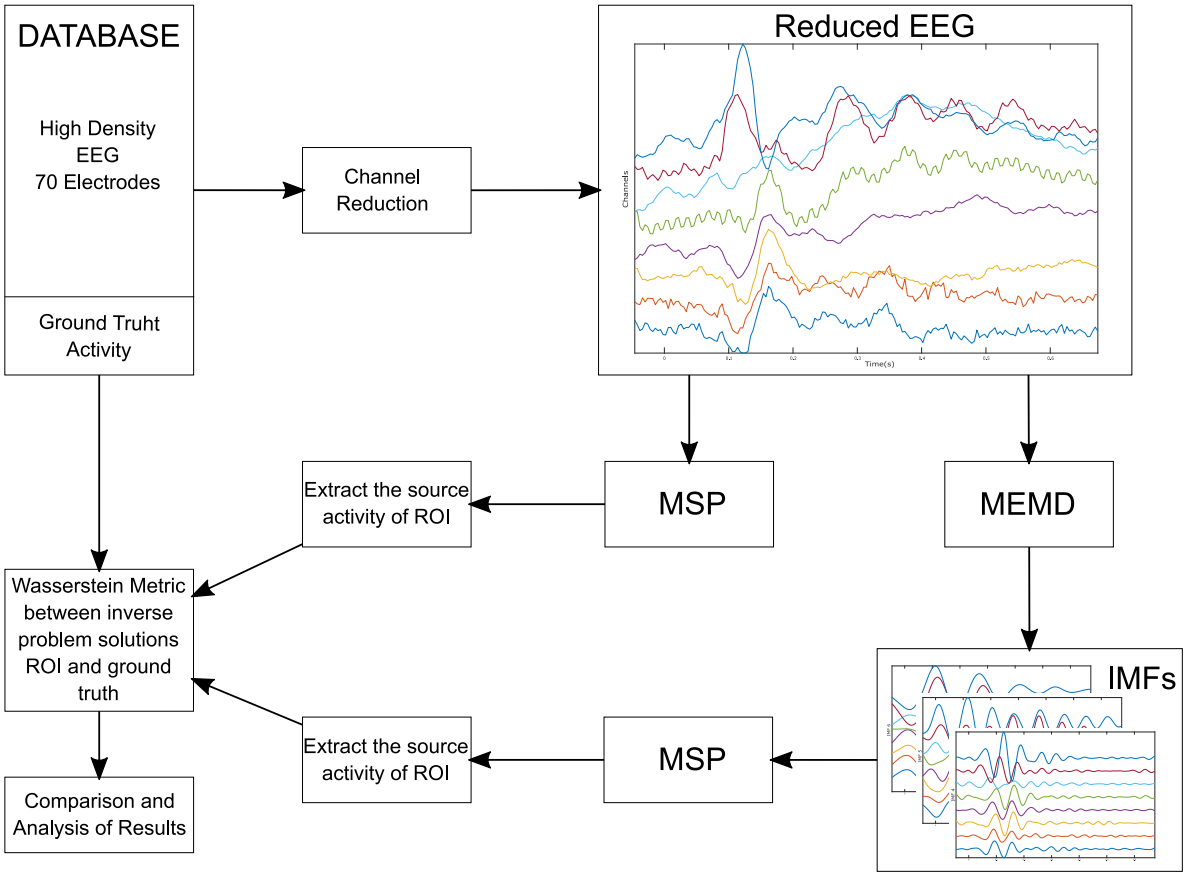

Figure 3.12: Block diagram of the methodology followed for processing the EEG from the database.

Channels were selected from the high-density EEG according to the number of electrodes to be evaluated. The reduced channel data was directly processed by MSP to obtain the so-called raw solution to the inverse problem. In addition, the reduced channel data was also processed using MEMD and one or several IMFs were selected to obtain the solution to the inverse problem with MSP. Finally, we compared both reconstructions of the source activities to the ground truth to evaluate the spatial accuracy of the solution using the Wm. The lead field matrix was reduced according to the position of the electrodes following a similar procedure as that used for the synthetic EEG

signals, the channels were selected to maintain as much as possible their equal spatial distribution over the scalp. The layout of the reduction is showed in Fig.3.13a, 3.13b and 3.13c for 32, 16, and 8 electrodes, respectively. In addition, the 8196 distributed sources of one of the subjects, the reduction of electrodes for 32, 16, and 8 channels, and their positions are showed in Fig.3.13d.

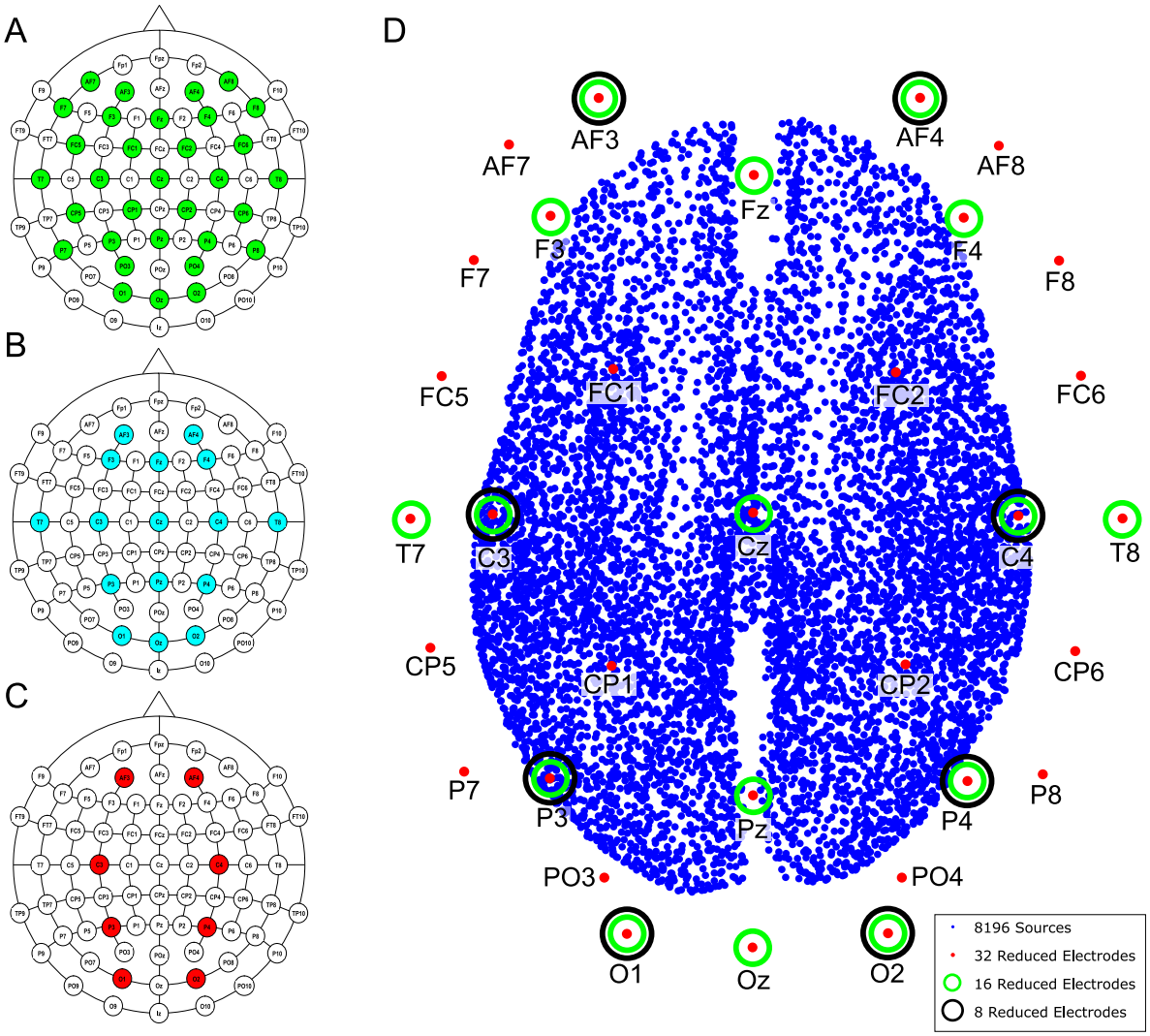

Figure 3.13: Layout according to the 10-10 system for 70 electrodes and the reduction performed for **(A)** 32, **(B)** 16, and **(C)** 8 electrodes.**(D)** Brain model with 8196 distributed sources and the names and positions of electrodes used in the channel reduction.

3.5.3 Accuracy Assessment

The Wm (also known as *Earth-Movers Distance*, [71]) was used as a quality index of the source reconstruction accuracy. This index provides a spatial comparison between

the ground truth and the estimated source activity, for which, Wm$\in \mathbb{R}^+$, and measures the work required to transform the estimated power distribution of sources into the ground truth power distribution by *transporting* the probability of mass ([14]). A lower Wm value represents better spatial accuracy of the source reconstruction. This metric has been used to compare EEG/MEG solution to the inverse problems to obtain a meaningful measure of estimated source distributions ([72]). The mean activity during the complete EEG segment is generally compared to the mean ground truth activity to assess source localization, as the Wm is considered to be a spatial accuray index. In addition to offering a temporal assessment of the reconstructed activity, the solutions were also evaluated using small time windows (time-ROIs). For the synthetic EEGs, the time-ROIs were defined as 250ms before and after the time of maximum activity for each of the simulated sources and for the real dataset assessment, the ROI was defined between 100 and 220ms. In general, the mean activity in the time-ROI was calculated and then compared to the mean activity of the ground truth during the same time-ROI.

3.5.4 Results

1. **Synthetic EEG Data Study.** The EEG signals were generated and processed for the nine aforementioned cases. An example of the application of MEMD for the reconstruction case of one source with 10Hz and 8 EEG channels is showed in Fig. 3.14. Following MEMD, IMF2 showed only noise activity with no identifiable source activity, whereas IMF3 unmixed the source activity, which was clearly identifiable, with no underlying noise. In addition, the reconstruction of the brain activity by MSP without preprocessing using MEMD (raw-MSP), split the source activity into two sources, on which one had an acceptable location. However, the main activity, represented in red, was located not in the preforntal cortex but at a lateral position, far of the original source, explaining the higher Wm (= 6.23) than of the MEMD-MSP reconstruction. In contrast, a Wm value of = 1.26 was obtained using MEMD-MSP and the main activity in the source map was correctly located. Although spurious activity appeared at the same position as that found with raw MSP, its value was attenuated. The appearance of this "ghost" activity may be due to the channel reduction. However, it is remarkable that the value obtained using MEMD-MSP was lower and the main activity clearly identifiable.

   MEMD was able to unmix the frequency activity for one source (Fig.3.14). This effect was also observed for the three and five active sources. The main IMFs decomposed by MEMD over 16 EEG channels, and the resulting brain reconstruction for three sources is showed in Fig.3.15. Decomposition using MEMD clearly split the activity into three IMFs as follows: the activity around 20Hz is showed in IMF2, that around 12Hz in IMF4, and that around 4Hz in IMF6. There was no mode-mixing in the MEMD decomposition. In addition, in the MEMD-MSP achieved a Wm= 10.14, which is substantially less than that achieved using raw MSP (= 15.57) when the neural activity reconstruction averaged over time

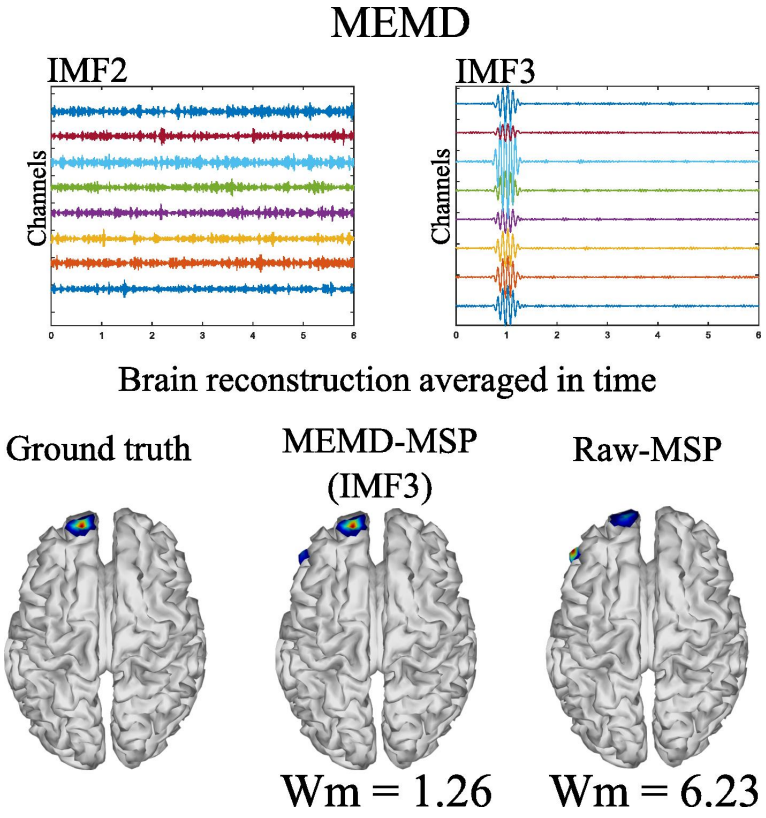

Figure 3.14: MEMD for one source with 10 Hz sinusoidal windowed activity and 8 EEG channels

was analyzed. Moreover, the MEMD-MSP reconstruction correctly identified the position of the three simulated sources, even if some spurious activity also appeared. In contrast, in the raw-MSP reconstruction, the position of the second source, located in the left hemisphere of the visual cortex, was incorrectly assigned and spurious activity appeared in various areas, with even higher intensity than the main source, showed by the higher Wm values obtained.

The spatial and temporal evolution of the neural activity for the ground truth and the reconstructions using MEMD-MSP and raw-MSP are showed in Fig. 3.16 for the three source at times, $t = 1$, $t = 3$, and $t = 5$ for the 16 EEG channels. The neural activity reconstruction obtained by the MEMD-MSP was better than that obtained from the raw data in terms of the Wm for each source. The time evolution of the neural activity for the MEMD was obtained by mixing the resulting brain mapping for IMF2, IMF4, and IMF6 of the MEMD, as the activity corresponding to each source was clearly divided between the selected IMFs (Fig. 3.15).

A similar evaluation of the spatio-temporal evolution to that of Fig. 3.16 is showed in Fig. 3.17, in which five active sources with 32 EEG channels was analyzed. In this analysis, MEMD-MSP outperformed raw-MSP, with the reconstructed neural activity by raw-MSP showing lower spatial has reduced spatial accuracy in almost

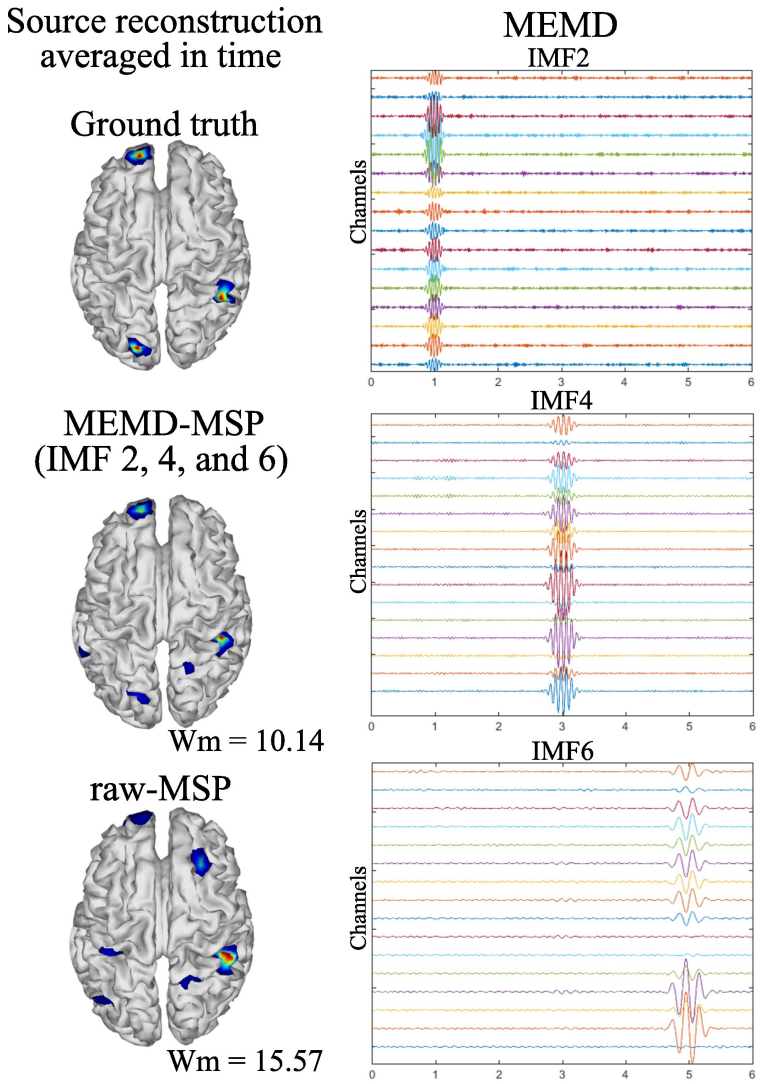

Figure 3.15: Ground truth activity, MEMD-MSP reconstruction, and raw-MSP reconstruction. The sources were simulated at 4, 12 and 20 Hz with a sinusoidal windowed activity and the source reconstruction was performed using 16 EEG channels. For the depicted MEMD-MSP reconstruction, IMFs 2, 4, and 6 (showed at right) were added to rebuild the EEG.

all the sources. Raw-MSP gave a lower Wm value than MEMD-MSP for only the third source at $t = 3$. However, the raw-MSP reconstruction contained several spurious activities for this source. In addition, it is possible to observe the effects of anterior and posterior sources in the other source reconstructions. In contrast, these effects were reduced when MEMD decomposition was applied, for which only attenuated activity from the third source is visible in the fourth reconstructed source. Furthermore, the Wm values were smaller than those for raw-MSP for almost all sources. Such a reduction of spurious activity and the attenuation of effects from other sources appeared when the EEG signals were decomposed into IMFs, and is arguably due to the rejection of noisy information in the IMF

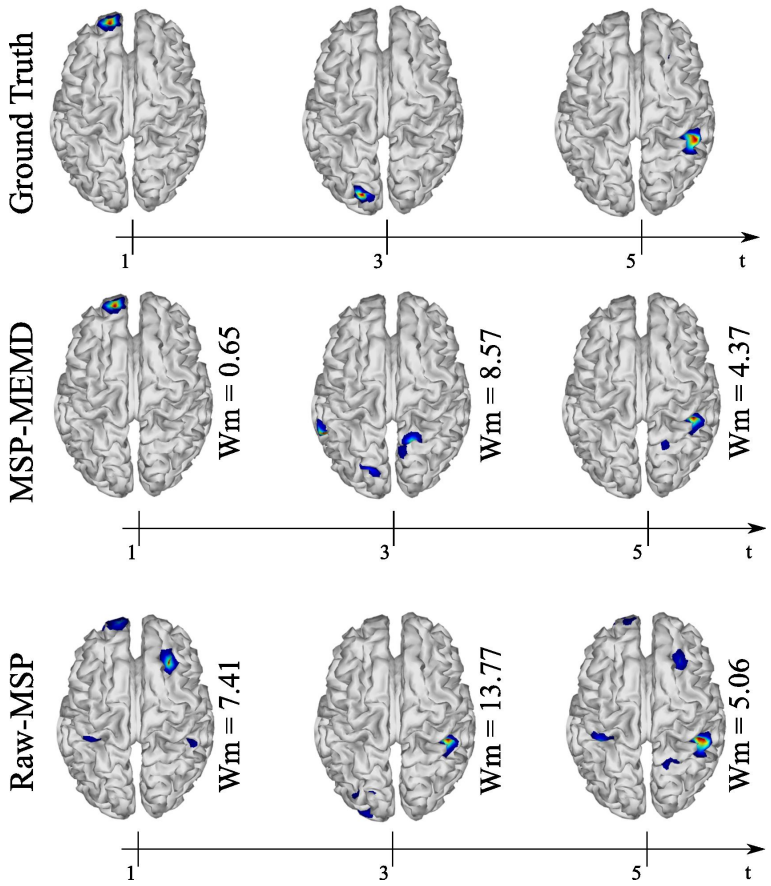

Figure 3.16: Ground truth, MEMD-MSP and raw-MSP neural activity mapping considering the evolution in time for three sources at time $t = 1$, $t = 3$, and $t = 5$ seconds with 16 EEG channels

selection process and the attenuation of mode-mixing effects by MEMD.

The Wm indices were compared between MEMD-MSP and raw-MSP for the mean reconstruction and each source for the source at the times instants $t = 1$, $t = 3$, and $t = 5$ seconds with 32, 16, and 8 electrodes (Fig. 3.18). In general, the effects of channel reduction are visible by the higher inaccuracy of raw-MSP than MEMD-MSP for eight channels. These results suggest that brain reconstruction with MEMD-MSP can still be performed without loss of accuracy by reducing the number of EEG channels by a factor of two. Although the Wm index increases with channel reduction, its slope is small and the reconstruction quality can be considered reasonable. In contrast, the raw-MSP reconstruction showed an exponential increase in the Wm value when electrode reduction was performed. In several cases the inclusion of the MEMD step considerably improves the performance of the brain mapping method, specially with a low number of electrodes. These significant differences (presented in Fig. 3.18) were obtained by performing two-sided pairwise t-tests with an alpha level of $p < 0.05$ using IBM SPSS Statistics for Windows, version 24 (IBM Corp., Armonk, N.Y., USA).

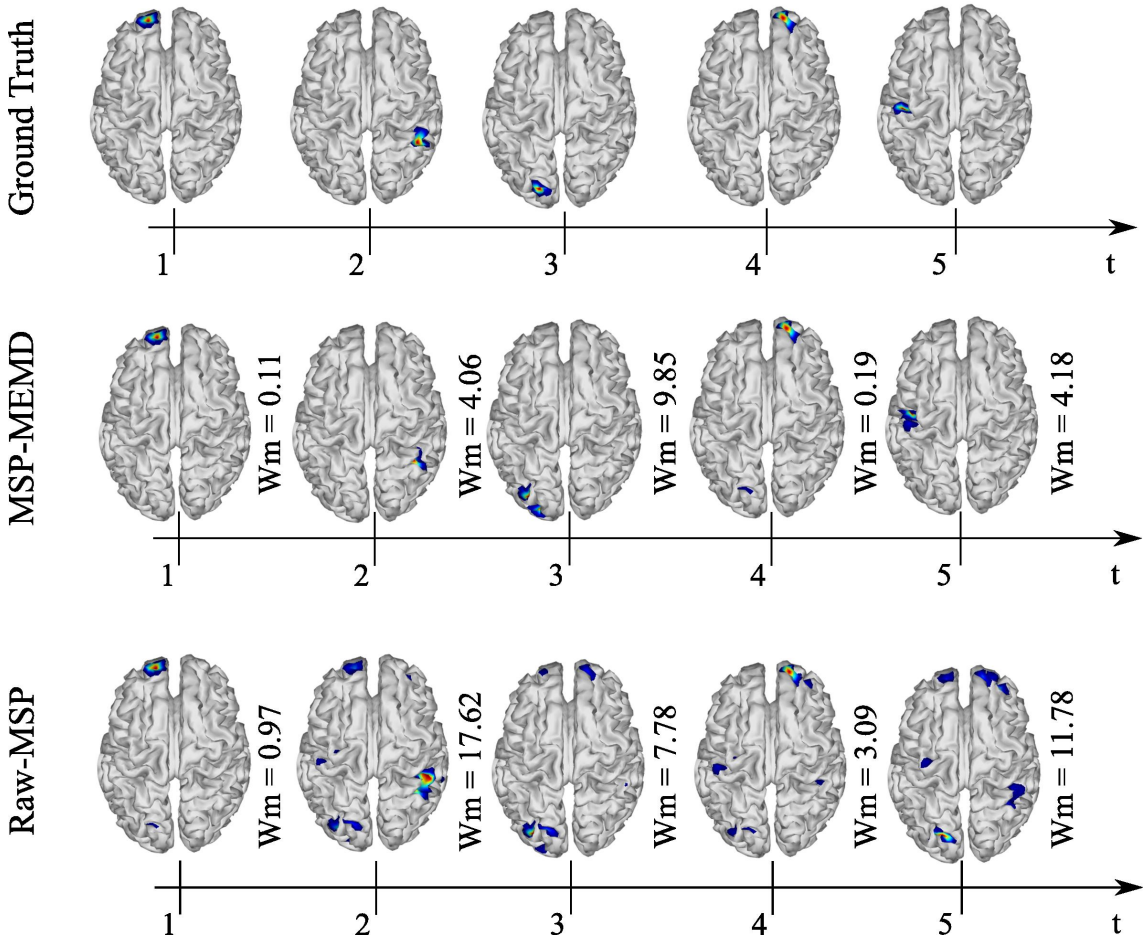

Figure 3.17: Ground truth, MEMD-MSP, and raw-MSP neural activity mapping considering the evolution in time for five sources at time $t = 1$, $t = 2$, $t = 3$, $t = 4$, and $t = 5$ seconds with 32 EEG channels

In general, the results for the synthetic EEG signals suggest that the use of the information extracted by MEMD improves the MSP brain mapping method. In all analyzed cases, MEMD-MSP attenuated the appearance of spurious activity and the joint MEMD-MSP approach retained spatial accuracy during electrode reduction.

2. **Results for the EEG Dataset.**

   The methodology described in Fig.3.12 was applied, and the dataset was processed using MEMD as a pre-processing step, the brain mapping solutions obtained using MSP for MEMD and directly from the ERP data, and the average compared to its own ground truth activity for each subject. A general vision of the results is showed in Fig. 3.19, in which the general mean of the Wm is presented with its standard deviation across all subjects and conditions, comparing raw-MSP and MEMD-MSP with the ground truth activity by the number of electrodes. Electrode reduction directly affected the quality of the source reconstruction, for which the solutions with MEMD-MSP had a lower mean and standard deviation than

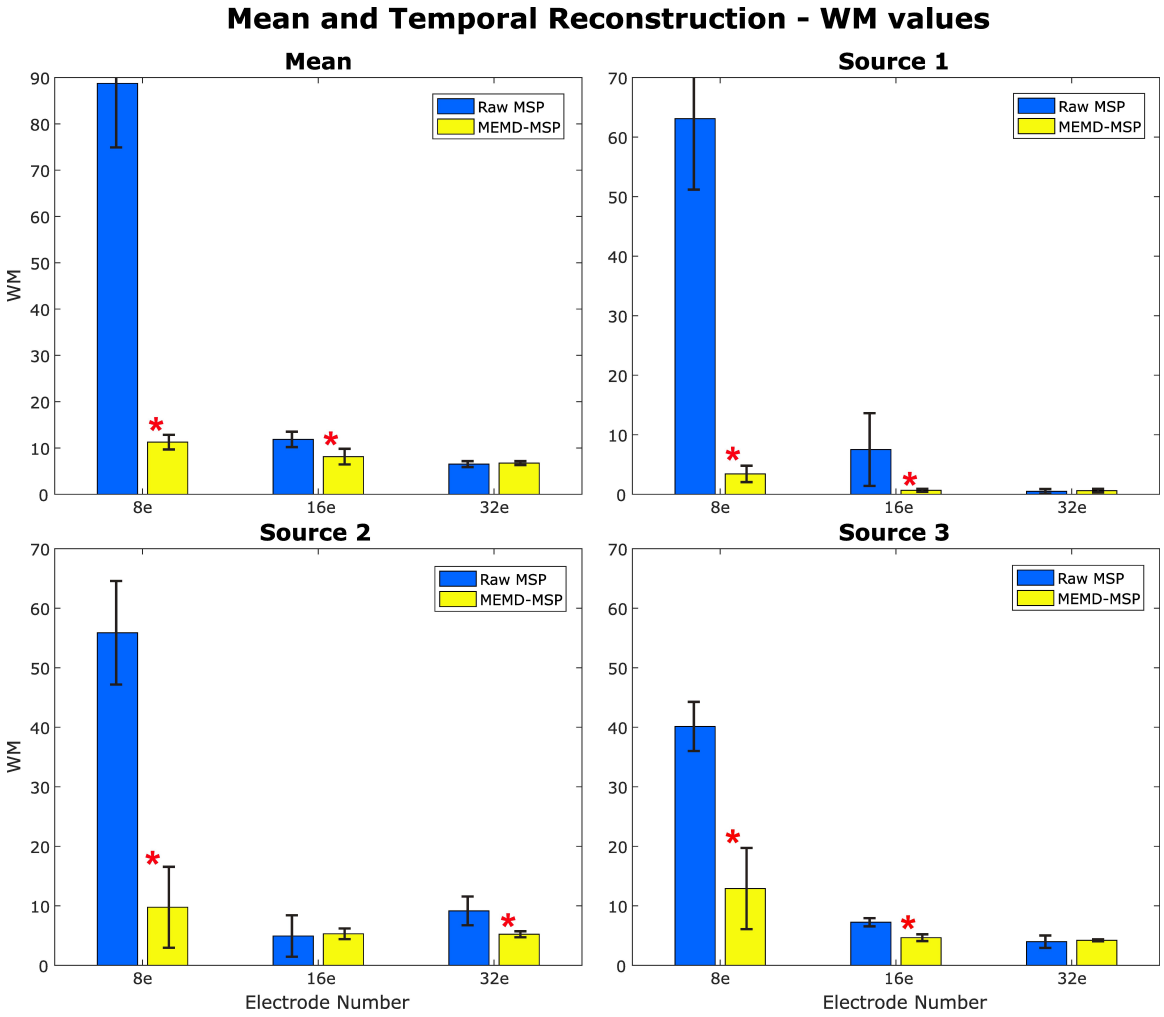

Figure 3.18: Mean Wm and standard deviation of the mean reconstruction (considering all the EEG records) and temporal reconstruction (considering the time ROI) with three numbers of electrodes and three active sources in the brain at times 1s, 3s, and 5s.*Significant improvement for p<0.001.

those with raw-MSP in all the cases. The inaccuracy of raw-MSP increased as the number of electrodes was reduced with a steep slope. In contrast, MEMD-MSP retained a constant quality index when the brain mapping was performed with 32 or 16 electrodes, and increased slightly when eight electrodes were used. However, with eight electrodes, MEMD-MSP reached a Wm value and standard deviation similar to that obtained with raw-MSP with 32 electrodes, for which there was no significant difference between raw-MSP using 32 electrodes and MEMD-MSP using eight electrodes when a two-sided pairwise t-test was applied using an alpha value of $p < 0.05$.

The WM indexes were labeled according to the condition of the EEG signals (familiar or scrambled faces) and the number of electrodes used to perform the solution to the inverse problems to provide another vision of the results (Fig. 3.20).

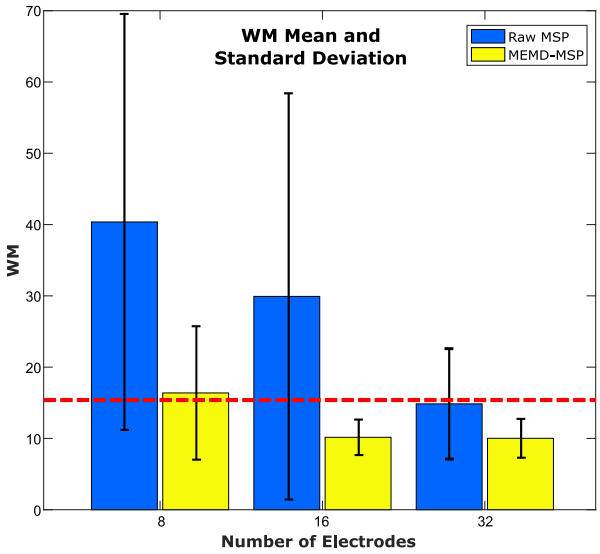

Figure 3.19: Mean Wm and standard deviation according to the number of electrodes for 16 subjects

The mean Wm value was slightly higher for scrambled faces with eight electrodes with MEMD-MSP than that obtained with raw-MSP with 32 electrodes. However, raw-MSP with 32 electrodes obtained a lower Wm value for familiar faces (24.43% less) than MEMD-MSP with eight electrodes. However, MEMD-MSP outperformed raw-MSP in all the cases for comparisons between the same condition and the same number of electrodes.

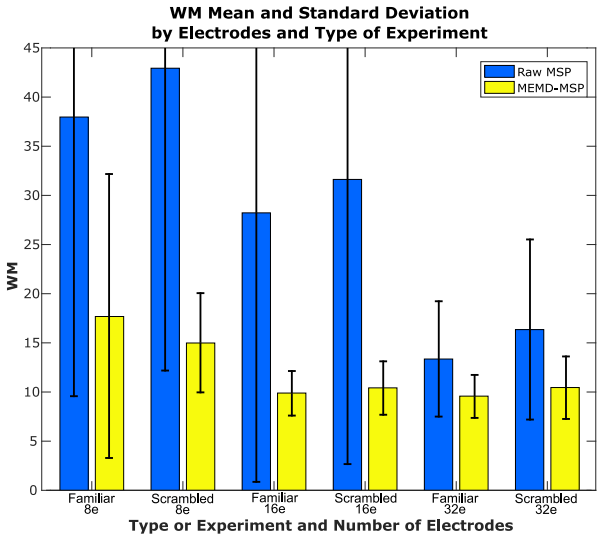

Figure 3.20: Mean Wm and standard deviation according to the type of experiment and number of electrodes

The improvement of the results by applying the MEMD can be explained by the separation of IMFs, as showed in Fig. 3.21, in which, eight electrode EEG signals are presented together with their IMF4 EEG reconstruction obtained by

MEMD. This Fig. 3.21 depicts how the main information of the evoked response is extracted around the established ROI, where the sparse temporal and frequency information provided by the IMF is sufficient to obtain better source localization of the activity than by using all the components of the EEG signal.

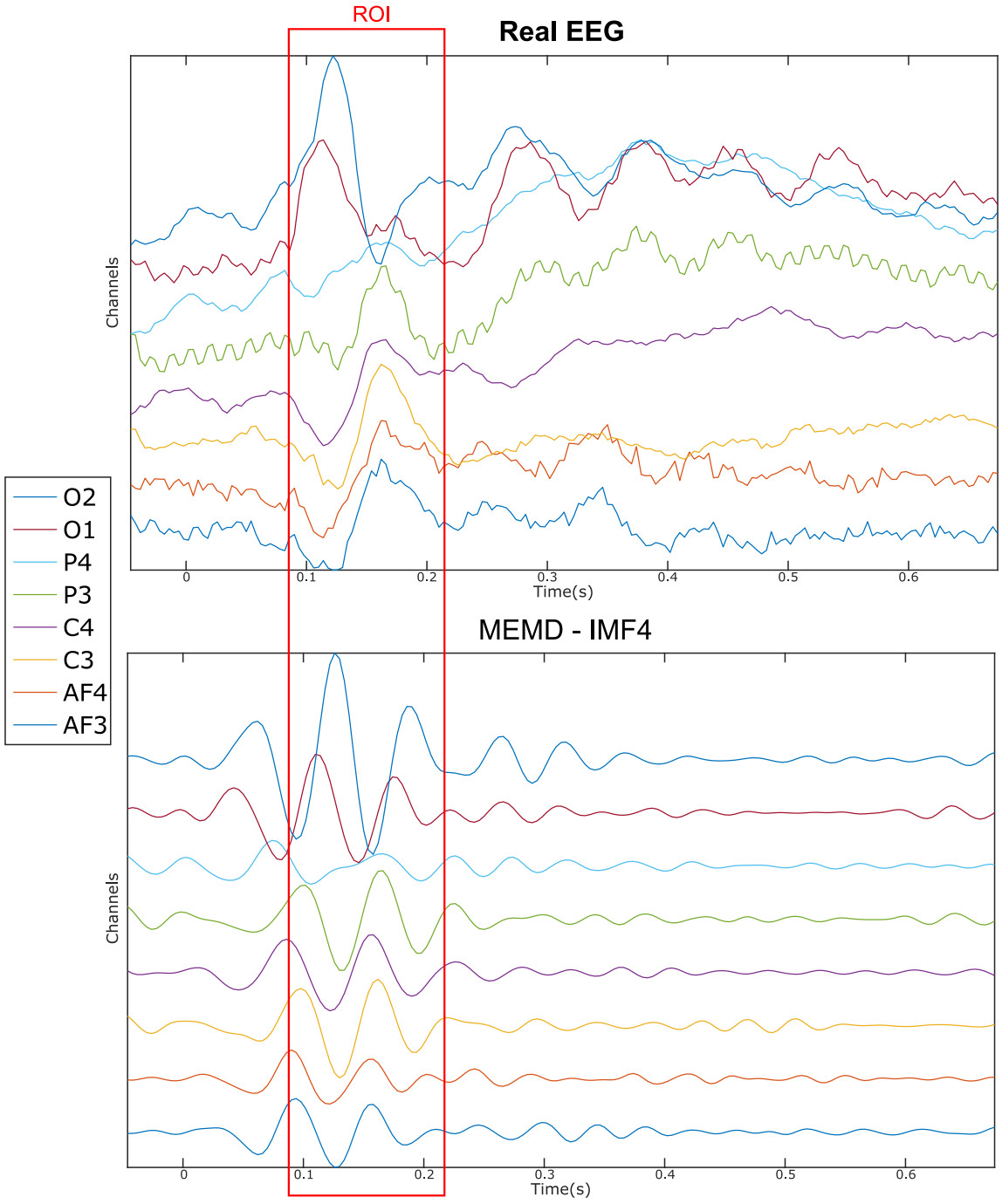

Figure 3.21: Eight-channel real EEG (Top) and the IMF4 component by MEMD (Bottom)

The location of the neural activity in the brain is showed in Fig.3.22. This activity

was found in the visual cortex, by [70] and [52] using a multi-modal technique involving EEG+MEG+fMRI. The figure provides the ground truth activity and the brain mapping reconstruction with 8, 16, and 32 electrodes with raw-MSP and MEMD-MSP.

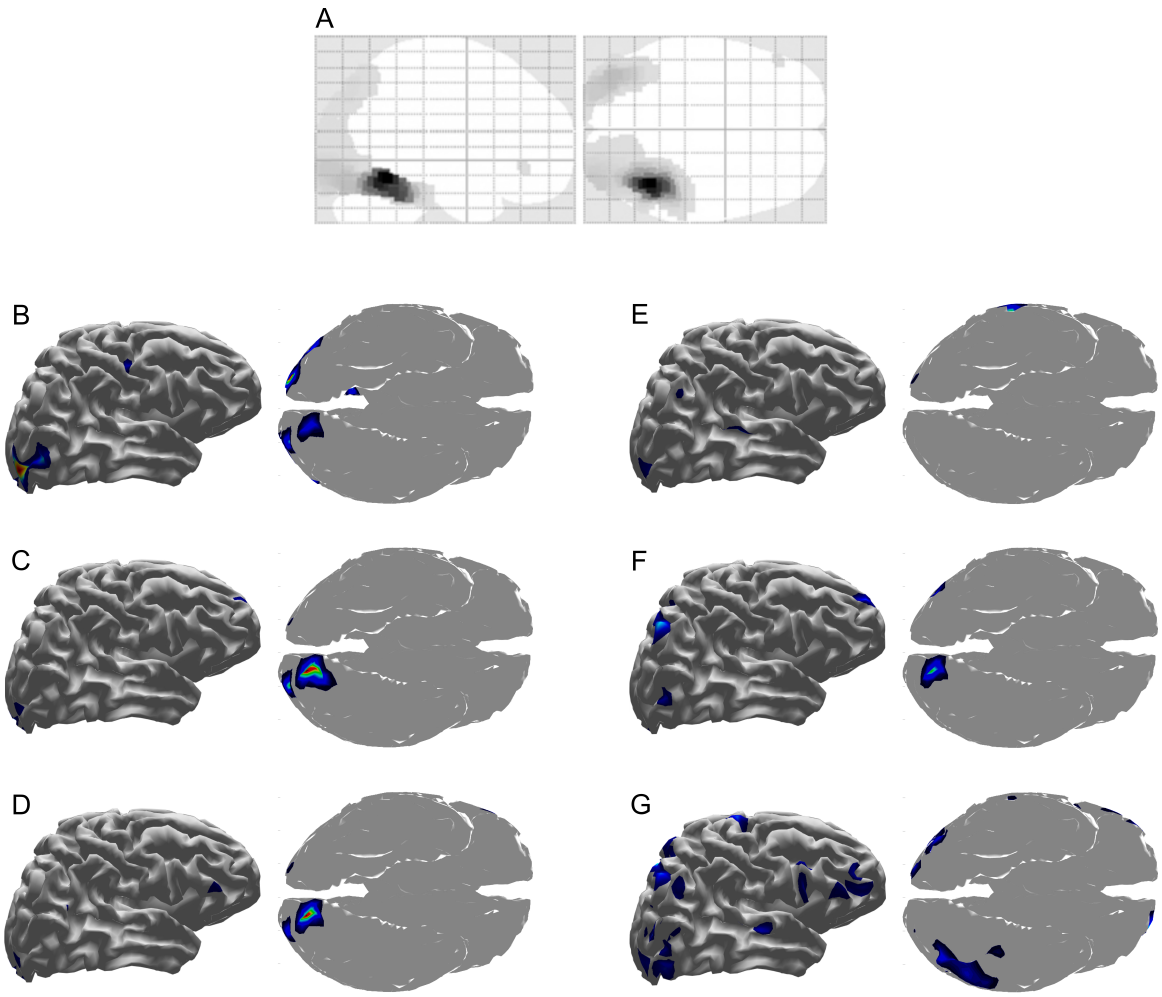

Figure 3.22: Brain activity reconstruction using a multi-modal technique involving EEG+MEG+fMRI. Ground truth activity from [52] **(A)**, brain activity reconstruction using MEMD-MSP with 8 **(B)**, 16 **(C)**, or 32 electrodes **(D)**, and that using raw-MSP with 8 **(E)**, 16 **(F)**, and 32 electrodes**(G)**.

The reconstructions using MEMD-MSP showed a little variation between the different numbers of electrodes involved in source localization (Fig.3.22). In contrast, the localization of the reconstructed sources varied without pre-processing the data in the raw-MSP, according to the number of electrodes. Moreover, these solutions showed activity in different brain areas, whereas the MEMD method focused solely on the visual cortex, which is directly involved during the visual face stimulus. Therefore, the use of certain IMFs provided by MEMD resulted in consistent accurate localization of the neural activity and an attenuation of background activity, represented by the lower Wm values.

3.6 Discussion

- A novel inverse problem solution for EEG source localization is presented. The method is based on a Multi-signal Wavelet Packed (MWP) decomposition with frequency bands selection. This method showed that it can efficiently select the relevant frequency bands where the activity is spatially and temporal located, and hence, the brain activity reconstruction can be done for each frequency band. Besides, the MWP step can be used in applications to choose relevant information by applying the entropy based cost function, and then, this information can be used to rebuild the neural activity located in specific frequency bands.

- The results achieved with Multi-signal Wavelet Packed, according to the Wasserstein metric, were very close for both the multimodal data for real EEG signals and ground truth for simulated signals. But, it is necessary an inverse process to reconstruct the estimated activity, because temporal resolution is lost in the decomposition process. Besides, it is necessary to set an appropriate mother wavelet to the analyzed signal.

- As an alternative, this study showed the combined use of Empirical Mode Decomposition - Multiple Sparse Priors (EMD-MSP) analysis for EEG data to localize sources of neural activity in the brain. The analysis has been performed in two different ways: i) using the raw data of the sources of brain activity, ii) using two EMD variants (EEMD and masking EMD) in addition to the standard EMD. First, in Fig. 3.8 is possible to observe how the signal is decomposed in different IMFs, where in each of them was located the simulated activity. In Fig. 3.8c is showed the IMFs obtained with the standard EMD, in IMF1 is showed the simulated activity at 2s (8Hz) and 3s (10Hz), the simulated activity at 1s (4Hz) is showed in IMF2 an IMF3. Something similar is seen in Fig. 3.8d, these results were obtained with EMD and masking signal. In Fig. 3.8e, the noise is located in the IMF1 and by analyzing this figure, the IMF2 shows the three signals of activity. It is clear the mode mixing problem when EMD is applied before of reconstructing the brain activity. It is worth noting that the brain activity reconstruction with EMD-MSP (only EMD, masking signal and EEMD) is better than MSP over raw-data, according to the Wassertein metric, it can be observed in Fig. 3.9.

- The study showed that the spatio-temporal reconstruction of brain-source activity can be severely affected by the mode-mixing problem when using EMD as a preprocessing tool with MSP to identify the location of brain activity. The three versions of an EMD implemented to cope with the mode-mixing problem and tested them in simulated EEG signals in an attempt to improve brain activity reconstruction when using EMD. The sub-band reconstruction effectively split the brain activity into frequency bands (Fig. 3.8). Visual inspection shows that the noise is adaptively filtered in one IMF (IMF1, as showed in Figure 3.8e), particularly for the EEMD method, improving the neural activity reconstruction,

which is computed using other IMFs (IMF2 and IMF3, as showed in Figure 3.8e).

- It is well known that the brain works at frequencies between 0.5Hz for Delta waves to 45Hz for Gamma waves. The use of time-frequency decomposition methods for EEG signals is generally applied to study brain processes associated with activity at certain frequencies and changes in brain wave oscillations during a number of experimental situations, e.g. ERP studies. EMD is a method that has showed the ability to separate signals using time-frequency decomposition in various contexts. However, EEG signals are challenging due to the frequency proximity of the source activity. Thus EMD solutions are generally hampered by mode-mixing during IMF decomposition. MEMD attenuates such effects when sources exhibit close frequency, as showed by [24].

- The multivariate version of EMD was investigated and combined with the source reconstruction algorithm MSP to evaluate the effects of MEMD as a pre-processing step during the calculation of brain mapping solutions and their performance for three different electrode montages: 32, 16, and 8 channels. The solutions obtained with MEMD-MSP were compared with those obtained by raw-MSP for synthetic EEG signals, for which, three scenarios of source activity were tested: one active source, three active sources, and five active sources, which, were simulated at frequencies from 2 to 20Hz. The solutions were also compared using a real dataset of EEG signals from 16 subjects who participated in a behavioral study of face perception, as reported by [66].

- The use of a pre-processing step with MEMD improves the accuracy of source reconstruction by MSP for all the evaluations. The results for synthetic and real EEG data showed that the quality of the solutions obtained by MEMD-MSP remained stable when 16 or 32 electrodes were used, and decreased slightly only when using eight channels. The reconstructions using MEMD-MSP with eight channels achieved similar values as raw-MSP with 32 channels for simulated sources (Fig.3.18) and for real data (Fig.3.20), for which no significant differences were found between the reconstructions. Moreover, adding the decomposition stage with MEMD and using selected information during the source reconstruction process, clearly makes it feasible to perform this process using low-density EEG, for which the small number of electrodes and sparse information of IMFs from MEMD are sufficient to retain the accuracy of the source reconstruction and reduce the effects of noise in the brain mapping solution.

- It is performed a temporal evaluation focused on ROIs defined by time windows around the appearance of sources in the synthetic EEG signals test and around the evoked activity for the real dataset. Reconstruction with MEMD-MSP generally showed a clear attenuation of the background activity (Fig. 3.15, 3.16, 3.17, and 3.22). This effect can be explained by the frequency decomposition and attenuation of mode-mixing resulting from MEMD, in which the analysis of the frequency information of the EEG channels allows MSP to focus on the source

activity presented in the selected IMFs (Fig. 3.15, and 3.21), resulting in solutions with a lower Wm index for the combination of methods.

Chapter 4

Hyper-parameters selection

4.1 Introduction

The regularized solutions have a strong dependence of the regularization parameters. Therefore, the estimation process for these parameters is important to get an approximate solution from data. In this work, a Tikhonov-Phillips regularized functional was proposed to reconstruct the brain activity using a dynamical model with spatio-temporal constraints (eq. (3.12b)). L-curve and Generalized Cross Validation (GCV) are some of the methods used to estimate the regularization parameters. This work was focused to GCV, in this case to estimate the hyperparameters (regularization parameters) in a multi-variable way.

The first contribution was a comparison between standard GCV and modified GCV. GCV was modified through out of the Genetic Algorithms (GCV-GA), which were used to improve the search mechanism to find the optimal values of the regularization parameters. The Wasserstein metric was very similar among brain activity reconstruction with standard GCV and brain activity reconstruction with GCV-GA, but the computational cost was less for GCV-GA than standard GCV.

Another contribution was the brain activity reconstruction per automatic selection of frequency bands. It was introduced a data driven method to process the EEG signal and using entropy analysis. Three methods were assessed; Multi-signal Wavelet Packed (MWP), Empirical Mode Decomposition (EMD) and Multivariate Empirical Mode Decomposition (MEMD). This kind of constraint could be useful when the brain activity reconstruction is centered in a specific spectral area.

4.2 Spatio-Temporal hyper-parameters

4.2.1 Classical estimation method

The neuromagnetic inverse problem with spatio-temporal constraints is solved using a regularized methods. Usually, these methods must minimize a cost function, as showed in eq. 3.3, which allows getting an approximate location of the active sources. The regularization process strongly depends of the regularization parameters, which directly can affect the quality of the neural activity reconstruction. In the presented methods two parameters have been considered, $\boldsymbol{\gamma}_k$ associated to the spatial constraint and $\boldsymbol{\lambda}_k$ to the temporal constraint. Similar that in [16] a multiparameter generalized cross validation (GCV) can be performed for the regularized observers. The GCV method considers the following cost function defined as $\mathcal{G}(\lambda_k, \gamma_k)$ for find these parameters:

$$\mathcal{G}(\lambda_k, \gamma_k) = \frac{||\boldsymbol{M}\boldsymbol{x}_k(\lambda_k, \gamma_k) - \boldsymbol{y}_k||_2^2}{tr(\boldsymbol{I} - \boldsymbol{M}\boldsymbol{M}^{\dagger}(\lambda_k, \gamma_k))^2} \tag{4.1}$$

being $\boldsymbol{M}^{\dagger}$ the regularized lead field matrix, this matrix is the same for the presented observers and can be computed using the next expression

$$\boldsymbol{M}^{\dagger} = (\boldsymbol{M}^T\boldsymbol{M} + \gamma^2\boldsymbol{I} + \lambda^2\boldsymbol{I})^{-1}\boldsymbol{M}^T \tag{4.2}$$

The optimal values for these hyper-parameters are estimated using a *fminsearchbnd* function of Matlab. This a good optimization function and the results by reconstructing the brain activity have been close to the ground truth.

fminserachbnd is is used exactly like *fminsearch*, except that bounds are applied to the variables. The bounds are applied internally, using a transformation of the variables. *fminsearch* uses the Nelder-Mead simplex algorithm as described in [73].

4.2.2 Proposed optimized method

GCV with genetic algorithm. In this work is proposed a genetic algorithm (GA) to search optimal solution from a random population. It can be applied using the GCV cost function, where through of the following stages: compute and assign the fitness value, selection, crossover, mutation, elitism and new random member, it is possible to find the regularization parameters.

The process to the genetic algorithm using GCV as a cost function (GA-GCV) is showed in Fig. 4.1. The method considers an initial random population with two chromosomes $\boldsymbol{cr} = 2$, corresponding to regularization parameters $\boldsymbol{\lambda}$ and $\boldsymbol{\gamma}$, the population only is created one time at the first sample and has $\boldsymbol{n}$ members. The random value range of the

Figure 4.1: Flow chart of proposed genetic algorithm for regularization parameters selection

chromosomes is determined between zero and the maximum singular value of the matrix $\boldsymbol{M}$. Then, the members are classified by a basic tournament, sorting the population according to the cost function $\mathcal{G}$ of each member, afterwards, a set of parents is founded, this set called $\boldsymbol{P} \in \mathbb{R}^{np \times cr}$ with $\boldsymbol{np}$ members form the union of two subsets $P = P_1 \cup P_2$, the subset $\boldsymbol{P_1} \in \mathbb{R}^{np_1 \times cr}$ contains the best $\boldsymbol{np}_1$ members and the subset $\boldsymbol{P_2} \in \mathbb{R}^{np_2 \times cr}$ contains the worst $\boldsymbol{np}_2$ members. The crossover process, where the children set are formed with chromosomes of different parents according to a randomly sort of the set $\boldsymbol{P}$, and the number of children $\boldsymbol{ns}$ is defined by $\boldsymbol{ns} = (2\boldsymbol{np}) - 2$. After, the first $\boldsymbol{nm}$ members from the set $\boldsymbol{P}$ are chosen to be part of the mutated set $\boldsymbol{MU} \in \mathbb{R}^{nm \times cr}$, where a random chromosome is replaced by a random number with the same criterion of the initial population, the chromosome to change is selected with equal probability between the two chromosomes. Then, the elitism set $\boldsymbol{E} \in \mathbb{R}^{ne \times cr}$ are the best $\boldsymbol{ne}$ parents of the generation. In the last step, a set $\boldsymbol{N} \in \mathbb{R}^{nw \times cr}$ where $\boldsymbol{nw}$ new members are created using the criterion of the initial population. Finally the set of the population for the next generation $\boldsymbol{NP} \in \mathbb{R}^{n \times cr}$ formed by $\boldsymbol{NP} = (\boldsymbol{E} \cup \boldsymbol{S} \cup \boldsymbol{MU} \cup \boldsymbol{N})$.

4.2.3 Experimental Framework

1. **Simulated EEG Data.** The neuronal activity in the brain is simulated using a discrete space state model described in eq. (2.6). The discrete values used

to simulate normal activity were $\tau = 20$, $a_1 = 1.0628$, $a_2 = 0.000143$, $a_3 = -0.000286$, $a_4 = -0.42857$, $a_5 = 0.008$, $b_1 = -0.12$ y $\|\boldsymbol{\eta}_k\| \leq 0.05$. The value of the activity was sampling at $\boldsymbol{F}_s = 250Hz$, the total time simulated is of $t = 1s$ for sample quantity of $N = 250$ samples. The activity is located in a head model (lead field matrix M) which consider 8196 distributed sources in the brain and 128 sensor locations placed by the standard BIOSEMI-128 EEG on the scalp. Afterward, the EEG is calculated using eq. (2.1)[11, 16].

Generalized Cross-Validation (GCV) and Genetic Algorithm GCV (GA-GCV) evaluation over simulated EEG dataset. To estimate the regularization parameters in each sample, two approaches are considered, the standard GCV algorithm based on the $fminsearchbnd$ Matlab^{TM} function and GCV based on genetic algorithm as a method of searching for minima. The parameters used in the GA-GCV are $\boldsymbol{cr} = 2$, $\boldsymbol{np} = 4$, $\boldsymbol{np}_1 = 2$, $\boldsymbol{np}_2 = 2$, $\boldsymbol{ns} = 6$, $\boldsymbol{nm} = 3$ and $\boldsymbol{nw} = 2$. Where the relative error measurement is used to compare the performance of the methods, using the relative error as follow

$$RelE = \frac{||\hat{\boldsymbol{x}}_k - \boldsymbol{x}_k||_2^2}{||\boldsymbol{x}_k||_2^2}. \tag{4.3}$$

In order to analyze the computational time, five simulated EEG were generated with a different duration, $t = 1s$, $t = 2s$, $t = 3s$, $t = 4s$, $t = 5s$ for $N = 250$, $N = 500$, $N = 750$, $N = 1000$ and $N = 1250$ samples respectively. Besides, the relative error was measured to both algorithms in terms of several signal noise ratio (SNR) conditions, 0dB, 5dB and 10dB and, in the same way, two cases were considered, three active sources and five active sources generated with the non-linear model eq.(2.9).

2. **Regularized Observers evaluation over real EEG database.** This test was performed over real EEG signals. The neural activity is assumed relying upon multi-modal solutions according to the real database described in sec. 3.5.2. Besides, the discrete model of parameters of the activity involved in the vector $\boldsymbol{\omega}_k$ to the sample frequency is described in sec. 2.2.4.[52].

4.2.4 Results

In order to analyze the computational time, the hardware and software used for the test are summarized in table 4.1.

The first results with simulated data were about the computational time in the estimation of the regularization parameters. In table 4.2 the comparison between GCV and GA-GCV can be seen and is possible to observe that the GA-GCV method took much less time than the standard GCV.

The real EEG dataset was built with the signals taken to at least 15 subjects, the head model was provided for each of them and their ground truth too (calculated through

Characteristic	Value
Operative system	Windows 7 64-bits
Processor	Intel core i7-6700
Number of cores	2
Speed per core	3.40GHz
RAM	8GB
Graphic card	No
Matlab version	2016bi

Table 4.1: Hardware and software characteristics.

EEG Duration	AG-GCV	Standard GCV
$1s$	$13.4s \pm 0.5s$	$112.9s \pm 1.1s$
$2s$	$26.1s \pm 0.6s$	$231.4s \pm 1.9s$
$3s$	$37.6s \pm 0.7$	$336.1s \pm 2.7s$
$4s$	$49.9s \pm 0.8s$	$450.2s \pm 3.7s$
$5s$	$61.6s \pm 1.2s$	$560.1s \pm 4.6s$

Table 4.2: Comparative analysis of computational time of AG-GCV and standard GCV for several EEG duration.

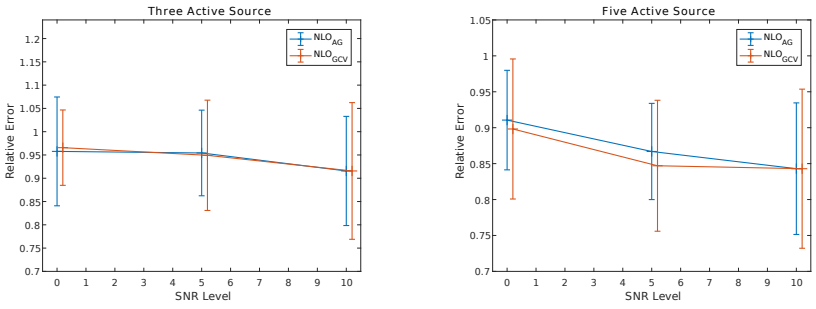

Figure 4.2: Relative error for NLO_{AG} and NLO_{GCV}, with signal-noise ratio of 0dB, 5dB and 10dB for three and five active sources .

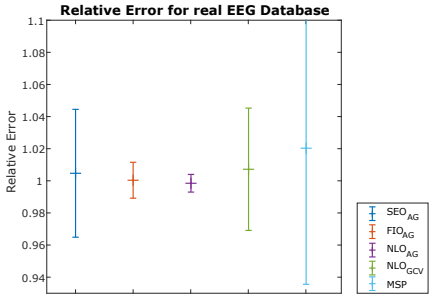

Figure 4.3: Relative error for FIO_{AG}, SEO_{AG},NLO_{AG}, NLO_{GCV} and MSP, with real EEG data.

multimodal technique) [52]. Source activity was estimated for each subject using the proposed methods, and its relative error was calculated using its respective ground truth. In Fig. 4.3 the relative error and standard deviation for each of the methods are showed. The outcomes suggest that the relative error is lower than the other methods in the NLO_{AG} (Non-Linear Observer) described in eq. (2.5) and (2.4) and is also remarkable that the dispersion is lower.

4.3 Frequency hyper-parameter

The frequency constraints are associated to data-driven methods as a Wavelet Transform (WT) or Empirical Mode Decomposition (EMD). These methods seek to decompose the signals according to their modes or frequency components. After this decomposition, every decomposed signal could be analyzed using different strategies as a retained energy o entropy features, which would allow it to choose those more representative components. Hence, this work proposes two automatic options to choose the frequency bands that allow rebuilding the brain activity according to the relevant data.

4.3.1 Best tree selection: Entropy function - MWP

The best tree was automatically calculated in $J = 4$ using the Shannon entropy of each subspace as cost function and the retained energy criterion was set at each subspace such as it does not exceed the 50% of the total signal energy as showed in Fig. 3.2. It could be corroborated that the proposed MWP decomposition has an inherent property of automatic sub-bands selection (see 3.3.6). Therefore, according to the energy and entropy criteria, the brain activity can be reconstructed with the more relevant frequency bands. Once the best tree is estimated, the neural activity estimation is carried out employing solely the selected sub-spaces.

4.3.2 Automatic IMF selection: Entropy Function - EMD

An entropy based cost function is applied over each IMF $\boldsymbol{\alpha}_i(t_k)$ (eq. (3.13)) as follows:

$$e_i = -\sum_k \|\boldsymbol{\alpha}_i(t_k)\|_2^2 \log(\|\boldsymbol{\alpha}_i(t_k)\|_2^2) \tag{4.4}$$

being e_i the entropy of each IMF, and $\boldsymbol{e} = [e_1 \dots e_N]$. In order to reconstruct the EEG signal $\tilde{\boldsymbol{y}}(t_k)$ an automatic selection of the IMFs (IMFs with highest entropy) are applied according to the measured entropy e_i.

$$\tilde{\boldsymbol{y}}(t_k) = \sum_{i \in O} \boldsymbol{\alpha}_i(t_k) \tag{4.5}$$

being O the subset of IMFs whose entropy e_i is over a threshold τ_e computed as follows

$$\tau_e = \frac{\max \boldsymbol{e} - \min \boldsymbol{e}}{2} + \min \boldsymbol{e} \tag{4.6}$$

The proposed methodology is divided in the following tasks, as depicted in Fig. 4.4:

1. EEG acquisition or simulation $\boldsymbol{y}(t_k)$.
2. Apply EMD on the EEG signal.
3. Optimal selection of IMFs using an entropy based cost function.
4. Reconstruction of a signal $\tilde{\boldsymbol{y}}(t_k)$ based on the optimally selected IMFs according to eq. (4.6).
5. Brain mapping of the neural activity based on the reconstructed signal.

- **Experimental setup.** The performance of the aforementioned method is evaluated by using simulated and real EEG signals containing epileptic seizures and it is compared with MWP. Four methods are considered for brain mapping (using multiple sparse prior - MSP) comparison to evaluate the performance of the proposed algorithm:
  1. Brain mapping ($\widehat{\boldsymbol{x}}(t_k)$) using the EEG database $\boldsymbol{y}(t_k)$ without EMD.
  2. Brain mapping ($\widehat{\boldsymbol{x}}_{\boldsymbol{EMD}}(t_k)$) using the reconstructed EEG $\tilde{\boldsymbol{y}}(t_k)$ obtained from EMD standard decomposition and an entropy based IMF selection.

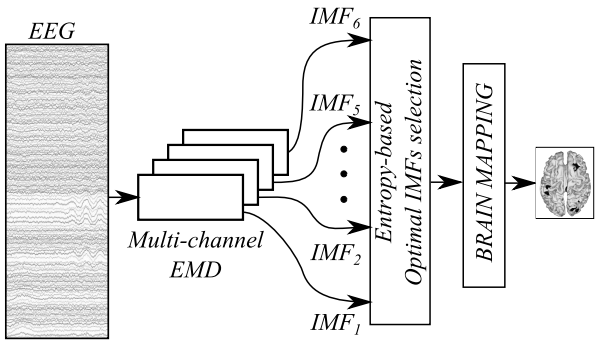

Figure 4.4: Proposed methodology for entropy-based selection of IMFs

3. Brain mapping ($\widehat{\boldsymbol{x}}_{\boldsymbol{W}}(t_k)$) using the reconstructed EEG $\tilde{\boldsymbol{y}}_{\boldsymbol{W}}(t_k)$ obtained from Wavelet Transform using Daubechies wavelet and three decompositions levels, where the level with highest energy is selected for reconstruction of the EEG.
4. Brain mapping ($\widehat{\boldsymbol{x}}_{\boldsymbol{WP}}(t_k)$) using the reconstructed EEG $\tilde{\boldsymbol{y}}_{\boldsymbol{WP}}(t_k)$ obtained from Wavelet Packets decomposition using Daubechies wavelet and three decompositions levels, where the level with highest entropy is selected for reconstruction of the EEG.

A common procedure to evaluate the performance of brain mapping techniques is using simulated EEG signals where the underlying brain activity is known. In this case, a measure of the brain mapping quality can be evaluated with the relative error measure [9] as follows:

$$e_s = \sum_k \frac{\|\widehat{\boldsymbol{x}}(t_k) - \boldsymbol{x}(t_k)\|_2^2}{\|\boldsymbol{x}(t_k)\|_2^2} \tag{4.7}$$

$$e_{EMD} = \sum_k \frac{\|\tilde{\boldsymbol{x}}_{\boldsymbol{EMD}}(t_k) - \boldsymbol{x}(t_k)\|_2^2}{\|\boldsymbol{x}(t_k)\|_2^2} \tag{4.8}$$

$$e_W = \sum_k \frac{\|\tilde{\boldsymbol{x}}_{\boldsymbol{W}}(t_k) - \boldsymbol{x}(t_k)\|_2^2}{\|\boldsymbol{x}(t_k)\|_2^2} \tag{4.9}$$

$$e_{WP} = \sum_k \frac{\|\tilde{\boldsymbol{x}}_{\boldsymbol{WP}}(t_k) - \boldsymbol{x}(t_k)\|_2^2}{\|\boldsymbol{x}(t_k)\|_2^2} \tag{4.10}$$

being e_s the reconstruction error of the brain mapping estimation $\widehat{\boldsymbol{x}}(t_k)$ resulting from $\boldsymbol{y}(t_k)$, e_{EMD} the reconstruction error of the brain mapping estimation $\tilde{\boldsymbol{x}}_{\boldsymbol{EMD}}(t_k)$ resulting from $\boldsymbol{y}(t_k)$, e_W the reconstruction error of the brain mapping estimation $\tilde{\boldsymbol{x}}_{\boldsymbol{W}}(t_k)$ resulting from $\tilde{\boldsymbol{y}}_{\boldsymbol{W}}(t_k)$ and e_{WP} the reconstruction error of the brain mapping estimation $\tilde{\boldsymbol{x}}_{\boldsymbol{WP}}(t_k)$ resulting from $\tilde{\boldsymbol{y}}_{\boldsymbol{WP}}(t_k)$.

1. **Simulated EEG signals.** For the first simulated database (SD-1) a complex nonlinear model of neural activity is used for EEG generation during

an epileptic seizure based on eq. (2.5) and eq. (2.6) [22]. Being $\boldsymbol{A}_1 = a_1\boldsymbol{I}_n$, $\boldsymbol{A}_2 = a_2\boldsymbol{I}_n$, $\boldsymbol{A}_3 = a_3\boldsymbol{I}_n$, $\boldsymbol{A}_4 = a_4\boldsymbol{I}_n$ and $\boldsymbol{A}_5 = a_5\boldsymbol{I}_n$, where $\boldsymbol{I}_n \in \mathbb{R}^{n\times n}$ is an identity matrix and $a_i \in \mathbb{R}$, are the model parameters which describe the dynamics of the brain activity, where $\boldsymbol{c}_{k-1}^{\circ 2}$ denotes the Hadammard Power. The model parameter are set to $\tau = 20$, $a_1 = 1.0628$, $a_2 = -0.42857$, $a_3 = 0.008$, $a_4 = 0.000143$, $a_5 = -0.000286$, and $\|\boldsymbol{\eta}(t_k)\| \leq 0.05$. The epileptic seizure is simulated at time $t_k = 0.5\,s$ by modifying the values of a_1 from 1.0628 to 1.3, while a_2 from -0.428 to -1 over the entire diagonal. The simulated EEG $\boldsymbol{y}(t_k)$ is obtained from $\boldsymbol{x}(t_k)$ using (2.1) where $\boldsymbol{\epsilon}(t_k)$ is set to achieve the Signal-to-Noise Ratios (SNRs) of 0, 5, 10, 15 and 20 dB, the sample rate is 250Hz, and a number of $d = 128$ electrodes and $n = 8196$ sources are considered.

For the second simulated database (SD-2), the epileptic seizure is simulated at time $t_k = 0.5\,s$ by using a sinusoidal signal with frequencies linearly varying in the range of 8 to 12Hz [16]. The simulated EEG $\boldsymbol{y}(t_k)$ is obtained from $\boldsymbol{x}(t_k)$ using (2.1) where $\boldsymbol{\epsilon}(t_k)$ is set to achieve the Signal-to-Noise Ratios (SNRs) of 0, 5, 10, 15 and 20 dB. The sample rate is 500Hz, and a number of $d = 128$ electrodes and $n = 8196$ sources are considered.

2. **Real EEG signals.** The real EEG database (RD) is recorded from two patients, one having frontal and another temporal lobe epilepsy [16]. Data were collected during routine clinical practice (Instituto de Epilepsia y Parkinson del Eje Cafetero from Pereira, Colombia), in an awake resting state. All patients signed the informed consent form before being enrolled into the study, and the process was approved by the ethical committee. A number of $d = 34$ electrodes are placed according to the $10-20$ system and data is sample rate of 1kHz with 16 bits-resolution. For the purpose of analysis, each 1s time series is segmented from the long recording around the beginning of the ictal event, that is at $t = 0.5$ s. It is worth noting that the pre-processing stage to remove noise or artifacts is not considered for the real EEG recordings. The testing head structure assumes $n = 20484$, where all sources are placed on the tessellated cortex surface and are perpendicular to it. For the real database, an additional analysis of epileptic seizure detection is performed based on the Hilbert spectrum.

4.3.2.1 Results

1. **Simulated Database.** An example of the EEG signal for SD-1 for a SNR of 0 dB is showed in Fig. 4.5. The analyzed signals are nonlinear and non-stationary, therefore the EMD is a good alternative to obtain information. An example of the signal in one channel is presented in Fig. 4.6.

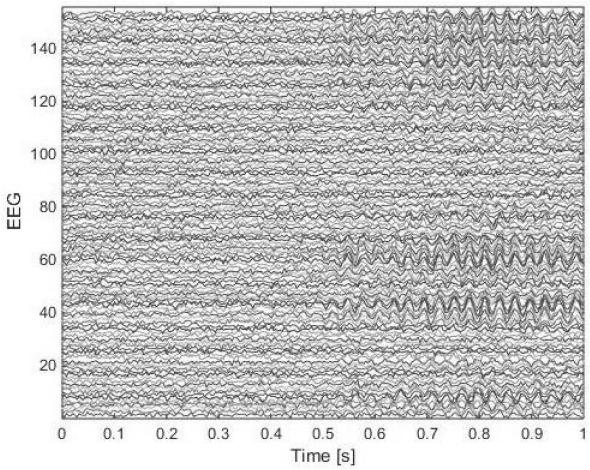

Figure 4.5: Simulated EEG for SD-1

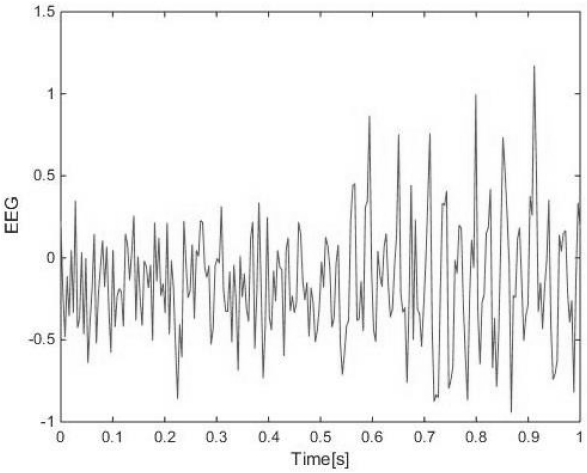

Figure 4.6: Example of one channel of simulated EEG for SD-1

After analyzing the database with the EMD, we obtained 6 IMFs per channel. In the IMF 2 in Fig. 4.7, it is possible to observe two remarked areas that show how different frequencies (different oscillations) appear in the same IMF. In these IMFs the mode mixing problem is evident [63]. An example of the retained energy and entropy for each IMF is presented in Fig. 4.8. In this example, the threshold is $\tau_e = 1930.9$ and then the EEG signal is reconstructed by using the IMF_1 and IMF_2.

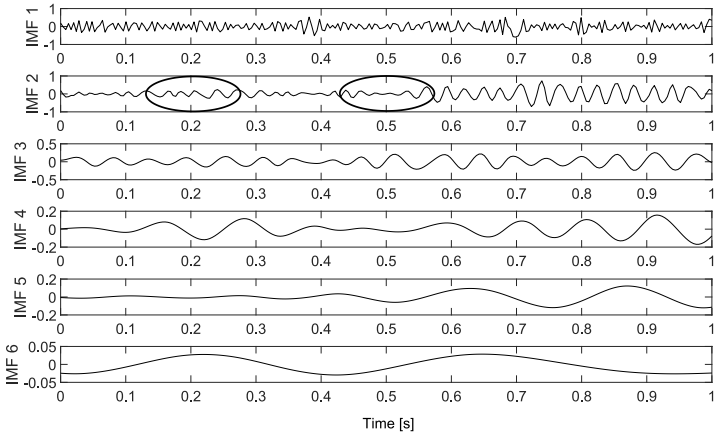

Figure 4.7: IMFs of y_s for SD-1 using standard EMD

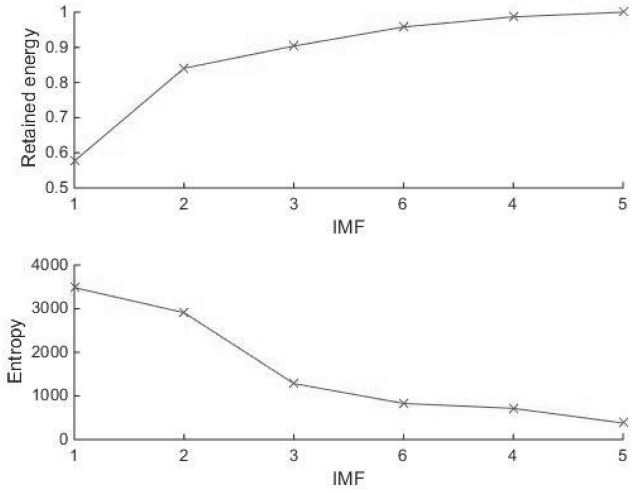

Figure 4.8: Retained energy and entropy of $\boldsymbol{y}(t_k)$ for SD-1 using standard EMD

A comparison of the original $\boldsymbol{y}(t_k)$ and reconstructed $\tilde{\boldsymbol{y}}(t_k)$ signals is presented in Fig. 4.9. The resulting brain mapping for each method is presented in Fig 4.10.

Relative error measure is used for evaluation. For the above example the relative errors based on (4.7) are as follows:

$$
\begin{aligned}
e_s &= 1.3284 \\
e_{EMD} &= 1.2942 \\
e_W &= 1.3106 \\
e_{WP} &= 1.2007
\end{aligned}
$$

showing that the best result is obtained for the brain mapping (using MSP) computed from the reconstructed neural activity using entropy-based selection of IMFs. An analysis based on 30 trials for each noise condition is showed in Fig. 4.11. As showed in Fig. 4.11, the best results are achieved by the proposed method of EMD decomposition with automatic selection of relevant IMFs based on the entropy measure (EMD-entropy). Therefore, for SD-2 and the Real Database, the comparison is performed only for the EEG data with and without the EMD stage. An example of the signal in one channel is presented in Fig. 4.12 and the resulting IMFs for SD-2 using standard EMD is presented in Fig. 4.13.

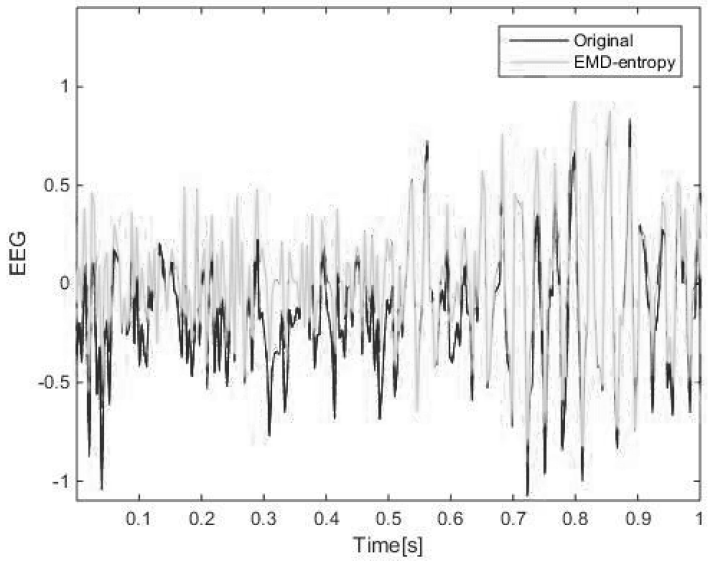

Figure 4.9: Comparison of simulated $\boldsymbol{y}(t_k)$ and optimally reconstructed $\tilde{\boldsymbol{y}}(t_k)$ signals for SD-1 by using standard EMD for one channel

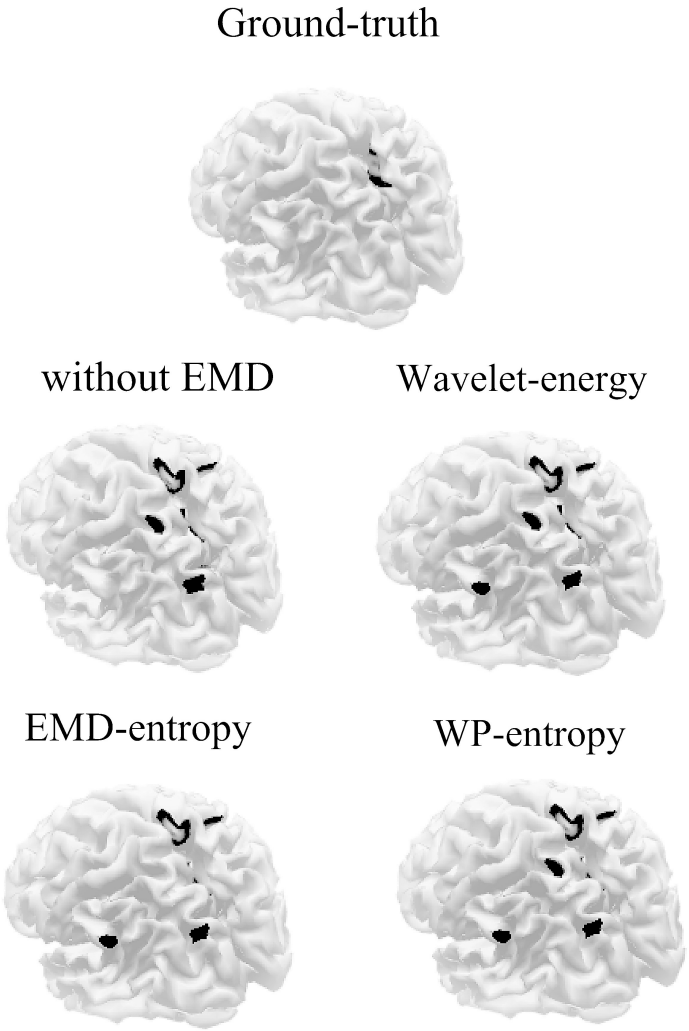

Figure 4.10: Comparison of brain mapping obtained for simulated $\boldsymbol{x}(t_k)$, estimated without EMD $\widehat{\boldsymbol{x}}(t_k)$ and optimally reconstructed $\tilde{\boldsymbol{x}}(t_k)$ neural activity for SD-1

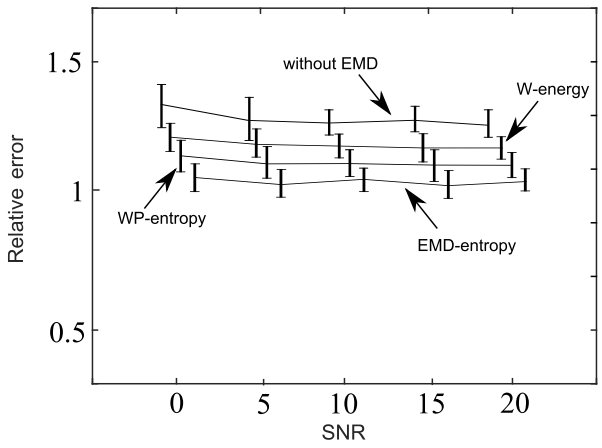

Figure 4.11: Relative error comparison for SD-1 under several noise conditions

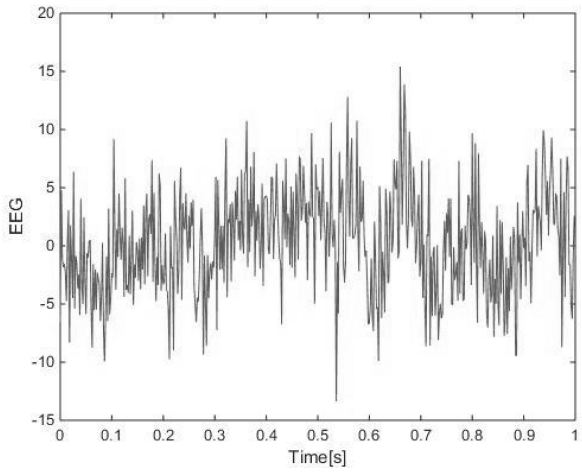

Figure 4.12: Example of one channel of simulated EEG for SD-2

The retained energy and entropy for each IMF are presented in Fig. 4.14. In this example, the threshold is $\tau_e = -1.4239 \times 10^6$ and then the EEG $\tilde{\boldsymbol{y}}(t_k)$ is reconstructed by using the IMF_3, IMF_2, IMF_6 and IMF_5.

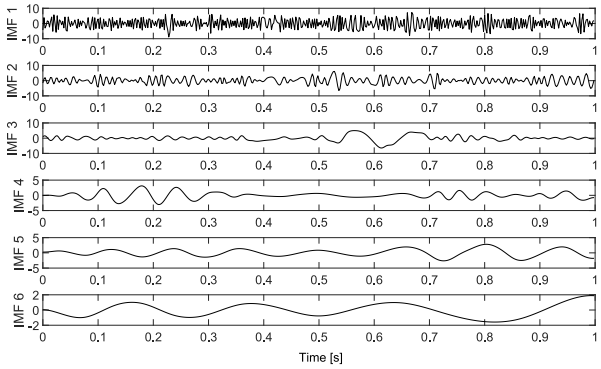

Figure 4.13: IMFs of $\boldsymbol{y}(t_k)$ for SD-2 using standard EMD

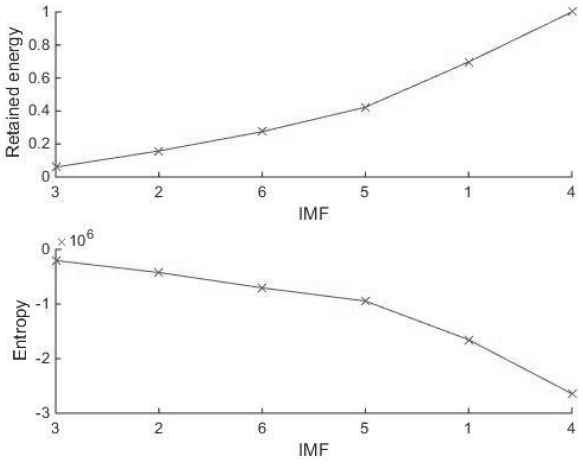

Figure 4.14: Retained energy and entropy of $\boldsymbol{y}(t_k)$ for SD-2 using standard EMD

A comparison of the original and reconstructed signals is showed in Fig. 4.15. The resulting brain mapping for each method applied in SD-2 is presented in Fig. 4.16. Relative error measure is used for evaluation. For the above example, the relative errors are as follows:

$$e_s = 1.3284$$
$$e_r = 1.2942$$

A comparison in terms of the relative error for 30 trials of the SD-2 is showed in Fig. 4.17.

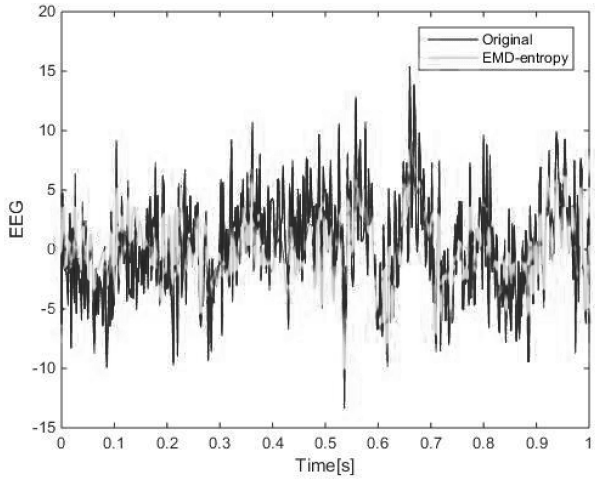

Figure 4.15: Comparison of simulated $\boldsymbol{y}(t_k)$ and optimally reconstructed $\tilde{\boldsymbol{y}}(t_k)$ signals for SD-2 by using standard EMD for one channel

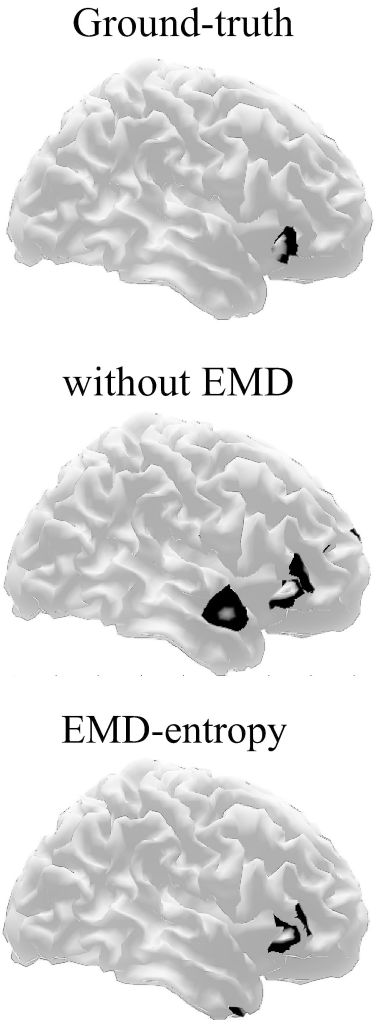

Figure 4.16: Comparison of brain mapping obtained for simulated $\boldsymbol{x}(t_k)$, estimated without EMD $\widehat{\boldsymbol{x}}(t_k)$ and optimally reconstructed $\tilde{\boldsymbol{x}}(t_k)$ neural activity for SD-1

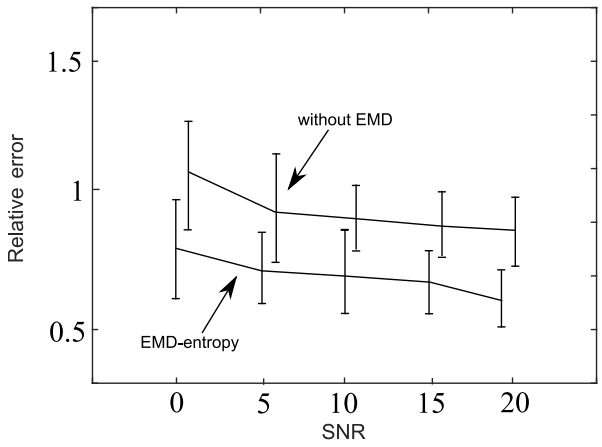

Figure 4.17: Comparison of relative error measure in reconstruction for SD-2 under several noise conditions

From the above, it can be seen an improvement of the source localization in terms of the relative error. This improvement is encouraging for further investigation since during epilepsy surgery the brain area where epileptic seizures begin is removed.

2. **Real Data Base.** An example of the EEG from the RD is presented in Fig. 4.18.

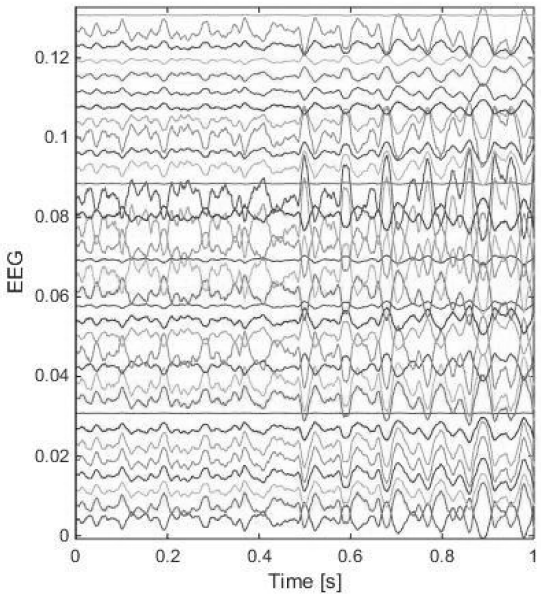

Figure 4.18: EEG from RD

For the real database a comparison of the original and reconstructed signal is presented in Fig. 4.19. The reconstructed signal is the sum of an optimal selection of the IMFs 4, 3 and 5.

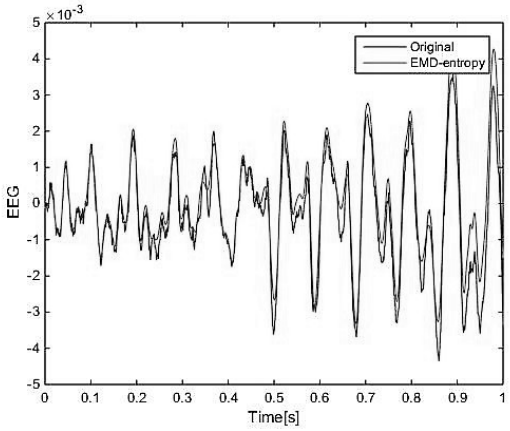

Figure 4.19: Comparison of real EEG signal and optimally reconstructed signal by using standard EMD for one channel

The resulting IMFs using standard EMD are presented in Fig. 4.20

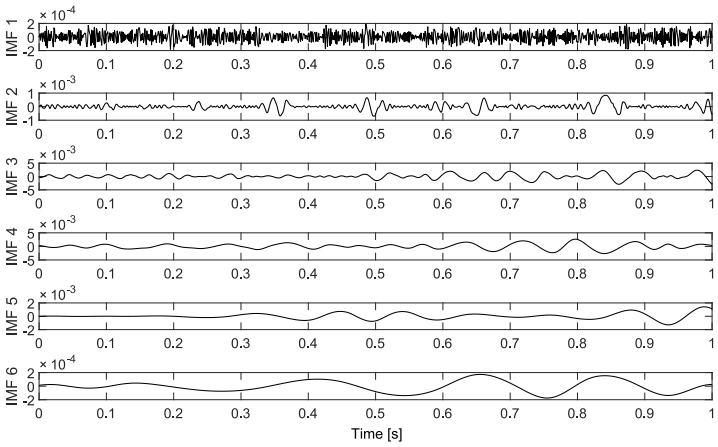

Figure 4.20: IMFs of real database using standard EMD

An example of the retained energy and entropy for each IMF is presented in Fig. 4.21. It can be seen that the IMFs are ordered according to the entropy values. In this case, the IMFs 4, 3 and 5 are used to reconstruct the signal since they are over the defined entropy threshold. The resulting brain mapping for each method is presented in Fig. 4.22.

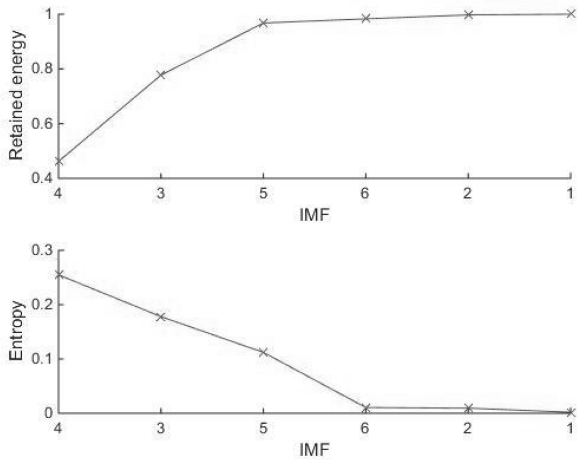

Figure 4.21: Retained energy and entropy of real database using standard EMD

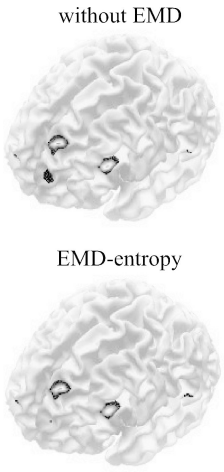

Figure 4.22: Comparison of brain mapping obtained for real database $\widehat{\boldsymbol{x}}(t_k)$ and optimal reconstructed $\tilde{\boldsymbol{x}}(t_k)$ neural activity

4.3.3 Automatic IMF selection: Spectral entropy - MEMD

4.3.3.1 Hilbert-Huang Spectral Entropy

Spectral entropy can be defined as a measure of the amount of disorder and this definition is based on the spectrum of a signal. The *Hilbert-Huang Epectral Entropy* (HHSE), for non-stationary signals, is calculated from Hilbert spectrum following these steps [74]:

1. The signal $\boldsymbol{x}(t)$ is decomposed into a series of IMFs (IMF_j).
2. The hilbert transform is applied to IMF_j $(1 \leq j \leq n)$ to obtain Y_{IMF_j}
3. The analytical signal is calculated for each IMF_j:

$$\boldsymbol{Z}_{IMF_j}(t) = \boldsymbol{IMF}_j(t) + i\boldsymbol{Y}_{IMF_j}(t) = \boldsymbol{a}_j(t)e^{i\theta_j(t)} \tag{4.11}$$

where

$$\boldsymbol{a}_j(t) = [\boldsymbol{IMF}_j^2(t) + \boldsymbol{Y}_{IMF_j}^2(t)]^{\frac{1}{2}} \tag{4.12}$$

and

$$\boldsymbol{\theta}_j(t) = \arctan(\frac{\boldsymbol{Y}_{IMF_j}}{\boldsymbol{IMF}_j(t)}) \tag{4.13}$$

4. The instantaneous frequency is calculated for IMF_j $(1 \leq j \leq n)$:

$$\omega_j(t) = \frac{d\theta_j(t)}{dt}, \tag{4.14}$$

The time series is expressed as:

$$\boldsymbol{x}(t) = \sum_{j=1}^{n} \boldsymbol{a}_j(t) exp(i \int \boldsymbol{\omega}_j dt) \tag{4.15}$$

The equation 4.15 represents, as function on time, the amplitude and the instantaneous frequency, therefore, this equation corresponds to the Hilbert Transform $\boldsymbol{H(\omega, t)}$. The Hilbert spectrum is the energy-time-frequency distribution over the signal $\boldsymbol{x}(t)$ and HHSE is calculated using the *frequency marginal* by integrating the Hilbert spectrum over the time-axis.

4.3.3.2 Experimental Setup

Studies in neuroscience have set five frequency bands, namely: delta-band (0-4 Hz), theta-band (4-8 Hz), Alpha-band (8-14 Hz), beta-band (14-30 Hz) and gamma-band (30-150Hz) [47]. In this work were proposed two simulated scenarios for the brain activity:

1. Three sources were randomly located in delta, alpha and beta band, respectively.
2. Five sources were randomly located in delta, theta, alpha, beta and gamma band, respectively.

They were also randomly located in different areas in the brain. The activity in each source was simulated using the following expression:

$$x_i(t_k) = e^{-\frac{1}{2}\left(\frac{t_k - c_i}{\sigma}\right)^2} \sin\left(2\pi f_i t_k\right), \tag{4.16}$$

c_i being the center of the windowed signal in seconds (1, 3 and 5 seconds for three sources and 1, 2, 3, 4 and 5 seconds for five sources), the frequency of the signal (f_i) was chosen randomly within of the ranges according with the frequency bands mentioned in [47] and $\sigma = 0.2$. In this work were simulated 30 trials for Signal-to-Noise-Ratio (SNR) of 20dB, 10dB, 0dB and -5dB using the model of generation (2.1).

After applying the HHSE to each trial and each noise level and by analyzing every IMF, the lowest computed spectral entropy values were associated to the frequency bands where the active sources were located. For this reason, the subset of IMFs whose entropy was under a threshold τ_e were chosen to brain activity reconstruction.

The proposed entropy function is the following:

$$e_j = -\sum_{k} \|\boldsymbol{IMF}_j(t)\|_2^2 \log(\|\boldsymbol{IMF}_j(t)\|_2^2) \tag{4.17}$$

It is applied over $\boldsymbol{IMF}_j(t)$ where e_j is the entropy of each IMF, and $\boldsymbol{e} = [e_1 \ldots e_N]$. The estimated EEG signal $\tilde{\boldsymbol{y}}(t)$, from IMFs with lowest spectral entropy (chosen automatically), is rebuilt according to the measured entropy e_i.

$$\tilde{\boldsymbol{y}}(t) = \sum_{i \in O} \boldsymbol{IMF}_j(t) \tag{4.18}$$

Access to a standard EEG database is important because it is necessary to know the underlying source activity to evaluate the methods for solving the inverse problem. We used a model with $n = 8196$ sources and 32 electrodes for simulation, as described by ([16]).

4.3.3.3 Results

After analyzing all trials with four noise levels, it could be found that the most suitable threshold to choose the relevant IMFs for locating the active sources (using MSP), was the IMFs with lowest spectral entropy and the chosen IMFs were those whose sum did not exceed 40 percent of the normalized HHSE for all IMFs. Two simulations were carried out under controlled conditions to show the results of this work, especially with respect to the location of the active sources, which were located for a clear visualization.

The first one was simulated for three active sources with $f_1 = 2Hz$, $f_2 = 9Hz$ and $f_3 = 22Hz$, the SNR was of $20dB$. In fig. 4.23 are showed three of the six IMFs chosen by entropy cost function; the simulated EEG fig. (4.23A), IMF2 Fig. (4.23B) associated to frequency beta-band ($f_3 = 22Hz$), IMF5 fig. (4.23C) associated to frequency alpha-band ($f_2 = 9Hz$) and IMF8 fig. (4.23D) associated to frequency delta-band ($f_1 = 2Hz$).

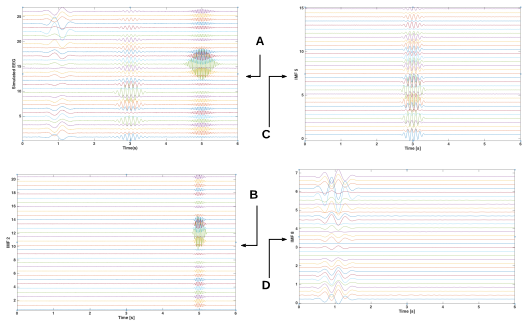

Figure 4.23: Selected IMFs for 3 sources with SNR 20dB

Each IMF used to locate the active source can be seen in fig. 4.24 whose sum allows obtaining the full location for the three active sources fig. 4.24B. The Wasserstein

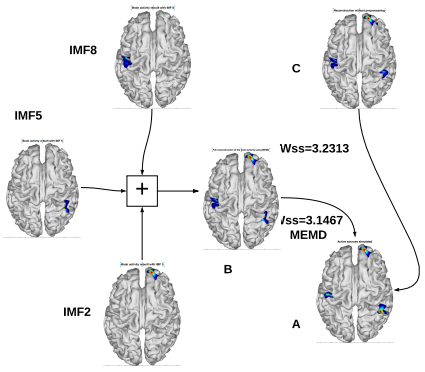

Figure 4.24: Wasserstein metric with and without MEMD for 3 active sources located with SNR of 20dB

metric for this estimation was the 3.1467 and the location without MEMD was 3.2313 fig. 4.24C, this measurements compared with the ground truth fig. 4.24A.

The second simulation was done for 5 sources with $f_1 = 1.5Hz$, $f_2 = 4Hz$, $f_3 = 9Hz$, $f_4 = 20Hz$ and $f_5 = 45Hz$, the SNR was of $-5dB$. The high level of noise can be seen in fig. 4.25A and the another figures are showed 5 of the 6 IMFs chosen. The advantage by using the MEMD is to be able to separate the activity in different bands of frequency e.g., in fig. 4.25B corresponds to gamma-band ($f_5 = 45Hz$) and was decomposed in the IMF2 with some noise. In the IMF4 (fig. 4.25C) was located the frequency associated to beta-band ($f_4 = 20Hz$) and the same way, it can be seen in fig. 4.25D the IMF5 with the frequency in alpha-band ($f_3 = 9Hz$), in fig. 4.25E the IMF7 with the frequency in theta-band ($f_2 = 4Hz$) and in fig. 4.25F the IMF9 with the frequency in delta-band ($f_1 = 1.5Hz$).

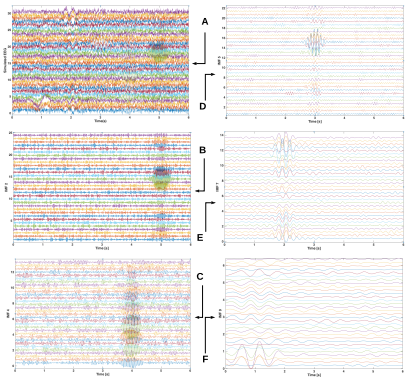

Figure 4.25: Selected IMFs for 5 sources with SNR -5dB

In the fig. 4.26 is presented that the Wesserstien metric for MSP with MEMD (fig. 4.26B) was lower than the metric for MSP without MEMD (fig. 4.26C), compared with the ground truth fig. 4.26A.

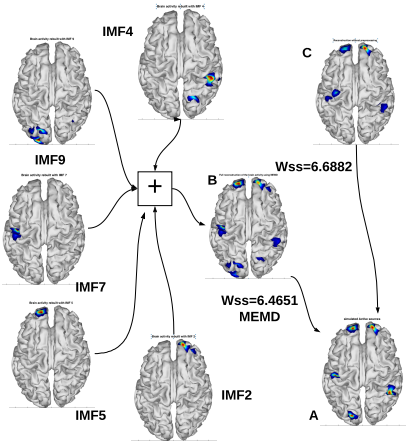

Figure 4.26: Wasserstein metric with and without MEMD for 5 active sources located with SNR of -5dB

4.4 Discussion

For the regularization parameters the method GA-GCV reaches a similar performance as the standard GCV in term of the results of the relative error, however the reduction of the computational load from approximately a rate of $112s$ per $1s$ of EEG to a $13s$ per $1s$ of EEG is an representative improvement. Besides, the methods were performed over simulated and real EEG dataset, where the proposed methods overcome the different levels of signal noise ratio even when the noise added to the signals was the same amplitude than the EEG signals and considering that they used the GA-GCV for the regularized parameters. The method with the non-linear constraint with GA NLO_{AG} and with GCV NLO_{GCV} presented good performances in terms of relative error.

The novel constraint to solve the inverse problem for EEG source localization was presented, the method was based on frequency constraints and was addressed to three data-driven methods. The first was based on Multi-signal Wavelet Packed (MWP), the second used Empirical Mode Decomposition (EMD) (with some variants) and finally, Multivariate Empirical Mode Decomposition (MEMD). All of them improved the accuracy (according to the Wasserstein metric (Wm)) the brain activity reconstruction, compared with the reconstruction using raw data.

The most relevant feature by analyzing the decomposed EEG signals was the entropy and the methods showed good results. The brain activity reconstruction using MWP and EMD, an entropy entropy cost function, based on Shannon's entropy, was implemented to develop an automatic method to identify those frequency bands on the threshold the entropy criteria.

The MWP step can be used in applications to choose relevant information by applying the entropy based cost function, and then, this information can be used to rebuild the neural activity located in specific frequency bands. Besides, brain mapping with frequency-spatio-temporal constraints into the dynamic inverse problem solution. This method showed that can efficiently select the relevant frequency bands where the activity is spatially and temporal located, and hence, the brain activity reconstruction can be done for each frequency band.

In this section we highlight some aspects that allow us to show the usefulness of the methodology proposed. The decomposition using IMFs allows us to reconstruct the neuronal activity using only the information that is considered relevant for this application. According to [18] previous works, the EMD does not have a good performance in decomposing and reconstructing the signals with low frequency because of the problem of mode mixing. In Figures 4.7, 4.13 and 4.20 is possible to observe this phenomena. Some methodologies such as the masking signal [61] or Ensamble Empirical Mode Decomposition (EEMD) have been proposed to avoid this problem [60]. The mode mixing does not disappear completely, however the technique is very interesting when it is compared with other strategies quite common for this type of application, for example with Discrete Wavelet Transform (DWT) is necessary to consider four factors affecting the performance in epileptic focus localization: the mother wavelet, the level of decomposition, frequency bands, and features [75]. Based on the above, we have proposed a new and simple methodology based on an entropy function that allows us to select the IMFs regardless of the mode mixing problem. The threshold value proposed in (4.6) was obtained after several tests with the values of entropy and retained energy in each IMF. The first validation using simulated databases allowed us to calculate the relative error and to affirm that the technique presented provides an accurate detection of sources associated to epileptic seizures.

In Figures 4.10 and 4.16 is possible to observe the desired mapping (ground-truth) and the values obtained without EMD and with the proposed method (EMD-entropy). In both cases, the relative error is lower with our method. In the first case, the EEG is reconstructed by using the IMF_1 and IMF_2 and in the second case we used the IMF_3, IMF_2, IMF_6 and IMF_5. The IMFs are selected automatically, and depending of the EEG the number of IMFs could change, but in either case the sources are located exactly. In both cases, the epileptic seizure appears at time $t_k = 0.5s$ and although time localization was not one of the purposes of this paper, it can be observed in the Hilbert spectrum that the instantaneous frequencies associated with each IMF have a change in their behavior at exactly this time, therefore an additional analysis of the instantaneous frequency could be performed in order to automatically detect the onset of an epileptic activity.

A method based on data-driven analysis, for improving the accuracy for EEG source localization (ESL), was evaluated. The MEMD was used in order to decompose the EEG signal in its main modes and separate the noisy components in order to locate the active sources with a minimum noise. It could also be seen that the EEG signal was decomposed in IMFs within different frequency bands and to each IMF was associated a

specific spectral entropy value. Those IMFs with incorporated frequency band or source activity allows reconstructing the brain activity of that source. The cost function of entropy was proposed for choosing the IMFs with lowest spectral entropy (calculated by using HHSE) and up to a maximum of 40 percent, with this cost function, all the active sources were located. The performance of MSP with MEMD, according to the Wesserstein metric, was better under SNR of -5db while for SNR of 20dB the performance of MSP was better without MEMD. In both cases, the method for choosing the IMFs took in account additional IMFs, because of the mode splitting generated by the MEMD method.

Chapter 5

Final Remarks

5.1 Conclusions

The proposed dynamic forward model allows simulating sparse source activity, where a specific brain area could have a normal behavior and, at the same time, another brain area could have a pathological behavior. An example of this behaviour could be focal epilepsy seizures. Additionally, this model allows considering that the temporal evolution of the activity is spatially non-homogeneous. This assumption permits to generate EEG signals within time segments where different kinds of brain activity are propagated into a different time windows. Under these conditions, the simulated EEG signals could be useful to test solutions to the inverse problem with sparseness constraints and they could be improve the reconstruction to spatially focal current sources.

When the visual, auditory or somatosensory stimuli are generated by external triggers, they can evoke brain activities in small cortical areas. These spatially focal activities could be considered as specialized area. The proposed dynamic model can generate source activity located in Brodmann areas; in this way, the solutions to the inverse problem could be focused to reconstruct the brain activity for specialized applications.

A dynamical inverse problem solution with frequency and spatio-temporal constraints were presented, it allows estimating the source activity with high spatial accuracy, according to the Wasserstein metric and the solution is estimated into a specific frequency band. The frequency constraint is independent of the spatio-temporal constraints, it is considered a data-driven method. Two methods were proposed, Multi-signal Wavelet Packed (MWP) and Empirical Mode Decomposition (EMD single or multivariate) to solve the inverse problem using MSP and IRA-L2. The solution to the inverse problem with frequency constraints based on MWP decomposition improved the source localization according to the Wasserstein metric and compared with the solution based on raw data; however, the temporal reconstruction loses resolution because in the level of signal decomposition does not have the complete temporal information. To reach an approximate estimation over the time, it is necessary to reconstruct the signal using

all the levels of decomposition. The results were improved using EMD and MEMD, but without a significant difference, the difference between these methods was the high dependence that WMP has for the wavelet mother and the loss of temporal resolution of the signal; instead of that, the EMD and MEMD only depends the data and the temporal reconstruction of the signal can be done from any selected IMF.

This work shows that adding a *priori* time-frequency information as input to the MSP source reconstruction algorithm makes it possible to obtain better solutions, even when information from only a small number of electrodes is used. MEMD should allow extraction of the main time-frequency information of sources that are hidden within the electrode data and then its used to obtain a good quality reconstruction, comparable to that obtained using the same MSP method with a high number of electrodes and without any prior information. Moreover, source activity is clearly separable in the MEMD-MSP solutions, resulting in an unmixing effect in the source space. The application of MEMD with other methods and the unmixed activity for brain connectivity will be studied in the future. The presented method could be applied to brain-computer interface applications and studies of brain connectivity.

A novel constraint to solve the inverse problem for electroencephalographic source imaging is presented based on a multi-signal Wavelet-Packets decomposition with best tree selection of subspace decomposition. The method improves the selection of relevant information of the Multi-signal EEG decomposition into its frequency bands since an automatic method based on the entropy cost function is applied. It can be concluded that the proposed method has two inherent properties: automatic subspace selection based on relevant EEG sub-bands information by using an entropy based cost function, sub-band brain mapping based on a sub-band dynamic inverse problem solution. As shown in the results, the proposed method can efficiently select the relevant subspaces where the activity is spatially and temporal located, an therefore the associate neural activity for each sub-band can be mapped into the brain. Therefore, the proposed method can be used in applications where the relevant information can be found in specific sub-bands which are automatically selected by the entropy based cost function.

An additional property associated to the sub-bands decomposition is the reduction of columns (time samples) for each level of decomposition according to the down-sampling property, where the reconstructed activity is also down-sampled in time. Even when the time resolution is diminished by applying the successive projections on the adequate subspaces, the time resolution can be perfectly recovered. Therefore, the proposed method allow a sub-band analysis that can be useful for connectivity based methods where the information of interest is only in some frequency bands.

5.2 Academic discussion

5.2.1 Journals

- Andres Felipe Soler-Guevara, Pablo A. Munoz-Gutierrez, Maximiliano Bueno-Lopez, Eduardo Giraldo, and Marta Molinas, "Low-Density EEG for Neural Activity Reconstruction Using Multivariate Empirical Mode Decomposition", submitted to Frontiers in Neuroscience. doi: https://doi.org/10.1101/713610. 2019

- Maximiliano Bueno-Lopez, Pablo A. Munoz-Gutierrez, Eduardo Giraldo, and Marta Molinas, "Electroencephalographic Source Localization based on Enhanced Empirical Mode Decomposition," IAENG International Journal of Computer Science, vol. 46, no. 2, pp. 228-236, 2019. ISSN: 1819-9224.

- Muñoz-Gutiérrez PA, Giraldo E, Bueno-López M and Molinas M.; "Localization of Active Brain Sources From EEG Signals Using Empirical Mode Decomposition: A Comparative Study". Frontiers in Integrative Neuroscience. Vol:12, N.55. doi: 10.3389/fnint.2018.00055, 2018 ISSN:1662-5145.

5.2.2 Proceedings

- Muñoz-Gutiérrez PA, Giraldo E, Bueno-López M and Molinas M.; "Automatic Selection of Frequency Bands for Electroencephalographic Source Localization". 9th International IEEE EMBS Conference on Neural Engineering, San Francisco, USA. March 20-23, 2019.

- Andrés Felipe Soler Guevara, Pablo Andrés Muñoz Gutierrez, Eduardo Giraldo, "Regularized State Observers for Source Activity Estimation" 2018 International Conference on Brain Informatics & Health, December 7-9, 2018, Arlington, Texas, USA, Lecture Notes in Computer Science, ISSN: 0302-9743.

- Maximiliano Bueno-Lopez, Pablo Andres Muñoz Gutierrez, Eduardo Giraldo, and Marta Molinas, "Analysis of Epileptic Activity based on Brain Mapping of EEG adaptive time-frequency decomposition", 2018 International Conference on Brain Informatics & Health, December 7-9, 2018, Arlington, Texas, USA, Lecture Notes in Computer Science, ISSN: 0302-9743.

- Pablo Andrés Muñoz Gutierrez, Juan David Martinez Vargas, Sergio García-Vega, Eduardo Giraldo, German Castellanos-Dominguez, "EEG based brain mapping by using Frequency-Spatio-Temporal constraints" 2018 International Conference on Brain Informatics & Health, December 7-9, 2018, Arlington, Texas, USA, Lecture Notes in Computer Science, ISSN: 0302-9743.

- Juan David Martinez Vargas, D.A. Nieto-Mora, Pablo Andrés Muñoz Gutierrez, Y.R. Céspedes-Villar, Eduardo Giraldo, German Castellanos-Dominguez, "Assessment of Source Connectivity for Emotional States Discrimination" 2018 International Conference on Brain Informatics & Health, December 7-9, 2018, Arlington, Texas, USA, Lecture Notes in Computer Science, ISSN: 0302-9743.

- Maximiliano Bueno-Lopez, Pablo Andres Muñoz Gutierrez, Eduardo Giraldo, and Marta Molinas, "Localizing the Focal Origin of Epileptic Activity using EEG Brain Mapping based on Empirical Mode Decomposition", ITISE 2018 International Conference on Time Series and Forecasting. 19-21 September 2018, Granada (Spain). ISBN: 978-84-17293-57-4

- Pablo Andrés Muñoz Gutierrez, Juan David Martinez Vargas, Eduardo Giraldo, and German Castellanos, "Sub-band brain mapping based on a Multivariate Wavelet Packet Decomposition", ITISE 2018 International Conference on Time Series and Forecasting. 19-21 September 2018, Granada (Spain). ISBN: 978-84-17293-57-4

- Muñoz-Gutierrez, P.A.; Giraldo, E..; "Location of brain areas using ensemble Kalman filter and considering non-homogeneous and no linear dynamical model", IEEE 37th Central America and Panama Convention (CONCAPAN XXXVII), Managua, Nicaragua ,15-17 Nov. 2017. ISBN: 978-1-5386-3509-4 . PDF

- Muñoz-Gutierrez, P.A.; Giraldo, E..; "Non-homogeneous multichannel electroencephalographic dynamic forward modeling of epilepsy", VII Latin American Congress on Biomedical Engineering CLAIB 2016, IFMBE Proceedings, Vol.1, N.60, pp.141-144, 2017. ISSN:1680-0737. PDF

- Muñoz-Gutierrez, P.A.; Giraldo, E..; "Time-course reconstruction of neural activity for multiple simultaneous sources", VII Latin American Congress on Biomedical Engineering CLAIB 2016, IFMBE Proceedings, Vol.1, N.60, pp.353-356, 2017. ISSN:1680-0737. PDF

- Muñoz-Gutierrez, P.A.; Giraldo, E..; Castellanos-Dominguez, C.G.; "Iterative joint dynamic brain mapping and neural activity modeling from electroencephalographic signals", VII Latin American Congress on Biomedical Engineering CLAIB 2016, IFMBE Proceedings, Vol.1, N.60, pp.433-436, 2017. ISSN:1680-0737. PDF

- Muñoz-Gutierrez, P.A.; Giraldo, E..; "Ensemble Kalman filter for state estimation of brain activity by considering alarge scale nonlinear dynamical model", VII Latin American Congress on Biomedical Engineering CLAIB 2016, IFMBE Proceedings, Vol.1, N.60, pp.445-448, 2017. ISSN:1680-0737. PDF

5.3 Future works

It can also consider the possibility of analyzing the inter-connectivity among zones by using models of interrelation of brain zones that allow it to observe the influence that some regions have over others, and their possible temporal evolution.

The proposed dynamical forward model can generate source activity with different dynamics and different cortical areas. To solve the inverse problem with these features, it is necessary to estimate the parameters and hyper-parameters for each cortical area and an independent way. This is an interesting challenge for the high computational complexity.

Appendix A

State estimation using Ensemble Kalman Filter

The ensemble Kalman filter (EnKF) has been a data assimilation technique widely used in weather forecasting and its application in state estimation tasks with non-linear dynamical models has been successful.

Ensemble Kalman Filter (EnKF) for brain activity recosntruction. The state estimation of the brain activity $\boldsymbol{x}_k$ can be obtained by applying the EnKF in two stages [76]. First, the forecast stage, where an ensemble of q forecasted state estimates is computed

$$\boldsymbol{x}_k^{f_i} = \boldsymbol{f}\left(\boldsymbol{x}_{k-1}^{a_i}, \bar{\boldsymbol{x}}_{k-2}^{a}, \bar{\boldsymbol{x}}_{k-\tau}^{a}\right) + \boldsymbol{\omega}_k^i \tag{A.1}$$

being $i = 1, \ldots, q$, $\boldsymbol{\omega}_k^i \in \mathbb{R}^{n\times 1}$ is a zero mean random variable with normal distribution an covariance $\boldsymbol{\Omega}_k \in \mathbb{R}^{n\times n}$. The sample error covariance matrix computed from $\boldsymbol{\omega}_k^i$ converges to $\boldsymbol{\Omega}_k$ as $q \to \infty$. The forecasted measurement is given by

$$\boldsymbol{y}_k^{f_i} = \boldsymbol{M}\boldsymbol{x}_k^{f_i} \tag{A.2}$$

where f_i denotes the $i-$th forecast ensemble member. Then, the ensemble mean for states $\bar{\boldsymbol{x}}_k^f \in \mathbb{R}^{n\times 1}$ is defined by

$$\bar{\boldsymbol{x}}_k^f = \frac{1}{q}\sum_{i=1}^{q} \boldsymbol{x}_k^{f_i} \tag{A.3}$$

and the ensemble mean for measurements $\bar{\boldsymbol{y}}_k^f$ is defined by

$$\bar{\boldsymbol{y}}_k^f = \frac{1}{q}\sum_{i=1}^{q} \boldsymbol{y}_k^{f_i} \tag{A.4}$$

The ensemble error matrix around the ensemble mean is defined as

$$\boldsymbol{E}_k^f = \left[\begin{array}{ccc} \boldsymbol{x}_k^{f_1} - \bar{\boldsymbol{x}}_k^f & \cdots & \boldsymbol{x}_k^{f_q} - \bar{\boldsymbol{x}}_k^f \end{array}\right] \tag{A.5}$$

being $\boldsymbol{E}_k^f \in \mathbb{R}^{n\times q}$, and the ensemble output error

$$\boldsymbol{E}_{y_k}^f = \left[\begin{array}{ccc} \boldsymbol{y}_k^{f_1} - \bar{\boldsymbol{y}}_k^f & \cdots & \boldsymbol{y}_k^{f_q} - \bar{\boldsymbol{y}}_k^f \end{array} \right] \tag{A.6}$$

being $\boldsymbol{E}_{y_k}^f \in \mathbb{R}^{d\times q}$, and where the forecast covariances are approximated as

$$\begin{aligned} \boldsymbol{P}_k^f &= \frac{1}{q-1}\boldsymbol{E}_k^f \left(\boldsymbol{E}_k^f\right)^\top \\ \boldsymbol{P}_{xy_k}^f &= \frac{1}{q-1}\boldsymbol{E}_k^f \left(\boldsymbol{E}_{y_k}^f\right)^\top \\ \boldsymbol{P}_{yy_k}^f &= \frac{1}{q-1}\boldsymbol{E}_{y_k}^f \left(\boldsymbol{E}_{y_k}^f\right)^\top \end{aligned}$$

being $\boldsymbol{P}_k^f \in \mathbb{R}^{n\times n}$, $\boldsymbol{P}_{xy_k}^f \in \mathbb{R}^{n\times d}$ and $\boldsymbol{P}_{yy_k}^f \in \mathbb{R}^{d\times d}$.

The second stage is the analysis stage, where an ensemble of perturbed observations $\boldsymbol{y}_k^i$ is obtained as follows

$$\boldsymbol{y}_k^i = \boldsymbol{y}_k + \boldsymbol{\upsilon}_k^i \tag{A.7}$$

where $\boldsymbol{\upsilon}_k^i \in \mathbb{R}^{d\times 1}$ is a zero mean random variable with normal distribution an covariance $\boldsymbol{\Upsilon}_k \in \mathbb{R}^{d\times d}$. The sample error covariance matrix computed from $\boldsymbol{\upsilon}_k^i$ converges to $\boldsymbol{\Upsilon}_k$ as $q \to \infty$. Also, the EnKF gain matrix is approximated as

$$\boldsymbol{K}_k = \boldsymbol{P}_{xy_k}^f \left(\boldsymbol{P}_{yy_k}^f\right)^{-1} \tag{A.8}$$

where it is worth noting that $\left(\boldsymbol{P}_{yy_k}^f\right)^{-1}$ is an inverse of $d \times d$, being $d << n$.

Therefore, an ensemble of data assimilation cycles is obtained as follows:

$$\boldsymbol{x}_k^{a_i} = \boldsymbol{x}_k^{f_i} + \boldsymbol{K}_k \left(\boldsymbol{y}_k^i - \boldsymbol{M}\boldsymbol{x}_k^{f_i}\right) \tag{A.9}$$

where a_i denotes the $i-$th analysis ensemble member. And finally, the ensemble mean of the analysis stage is computed as

$$\bar{\boldsymbol{x}}_k^a = \frac{1}{q}\sum_{i=1}^{q} \boldsymbol{x}_k^{a_i} \tag{A.10}$$

where $\bar{\boldsymbol{x}}_k^a$ is the estimated brain activity at sample k.

In this work, EnKF was explored as a technique for EEG source localization and specifically to estimate active sources inside the brain. In fig.A.1a can be seen the simulation for three active sources. On the left side, it is presented the simulated EEG and, in front, it is presented the average brain activity, this is important because the sources are activated in different instants of time.

The result of state estimation using EnKF can be seen in fig. A.1b. The EEG is shown on the left side and the signals were reconstructed with less noise and the brain activity was rebuilt, at least visually, very close to the simulated active sources.

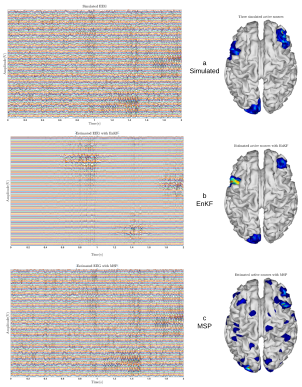

Figure A.1: State estimation using ensemble Kalman filter

In fig. A.1c is shown the estimated signals for EEG (on the left side) and the location of the active sources (on the right side) by using Multiple Sparse Piors (MSP). The temporal behavior is similar to the simulated EEG, but the reconstructed of the brain activity is unlike from the simulated.

Bibliography

[1] Matti Hämäläinen et al. "Interpreting measured magnetic fields of the brain: Estimates of current distributions." In: *Technical Report TKK-F-A559 HUT Finland* 32 (Dec. 1984).

[2] S. Baillet et al. "Electromagnetic brain mapping." In: *IEEE Signal Processing Magazine* 18.6 (Nov. 2001), pp. 14–30. ISSN: 1053-5888. DOI: 10.1109/79.962275.

[3] J. C. Mosher et al. "EEG and MEG: forward solutions for inverse methods." In: *IEEE Transactions on Biomedical Engineering* 46.3 (Mar. 1999), pp. 245–259. ISSN: 1558-2531. DOI: 10.1109/10.748978.

[4] ME BRANT. "Topographic mapping of brain electromagnetic signals: a review of current technology." en. In: *Am. J. Physiol Imaging.* 07 (July 1992), pp. 160–174.

[5] Matti Hämäläinen et al. "Magnetoencephalography: Theory, instrumentation, and applications to noninvasive studies of the working human brain." In: *Rev. Mod. Phys.* 65 (Apr. 1993), pp. 413–. DOI: 10.1103/RevModPhys.65.413.

[6] Munsif Ali Jatoi et al. "A survey of methods used for source localization using EEG signals." In: *Biomedical Signal Processing and Control* 11.1 (2014), pp. 42–52. ISSN: 17468108. DOI: 10.1016/j.bspc.2014.01.009. URL: http://dx.doi.org/10.1016/j.bspc.2014.01.009.

[7] M. Fukushima et al. "A State-Space Modeling Approach for Localization of Focal Current Sources From MEG." In: *IEEE Transactions on Biomedical Engineering* 59.6 (June 2012), pp. 1561–1571. ISSN: 0018-9294. DOI: 10.1109/TBME.2012.2189713.

[8] Camilo Lamus et al. "A spatiotemporal dynamic distributed solution to the MEG inverse problem." In: *NeuroImage* 63.2 (2012), pp. 894–909. ISSN: 10538119. DOI: 10.1016/j.neuroimage.2011.11.020. arXiv: 1511.05056.

[9] Roberta Grech et al. "Review on solving the inverse problem in EEG source analysis." In: *Journal of NeuroEngineering and Rehabilitation* 5.1 (2008), p. 25. ISSN: 1743-0003. DOI: 10.1186/1743-0003-5-25. URL: https://doi.org/10.1186/1743-0003-5-25.

[10] E. Pirondini et al. "Computationally Efficient Algorithms for Sparse, Dynamic Solutions to the EEG Source Localization Problem." In: *IEEE Transactions on Biomedical Engineering* 65.6 (June 2018), pp. 1359–1372. ISSN: 0018-9294. DOI: 10.1109/TBME.2017.2739824.

[11] E. Giraldo-Suárez et al. "Neural Activity Estimation from EEG Using an Iterative Dynamic Inverse Problem Solution." In: *Artificial Computation in Biology and Medicine*. Ed. by José Manuel Ferrández Vicente et al. Cham: Springer International Publishing, 2015, pp. 388–397. ISBN: 978-3-319-18914-7.

[12] J. I. Padilla-Buritica et al. "Weighted Filtering for Neural Activity Reconstruction Under Time Varying Constraints." In: *Artificial Computation in Biology and Medicine*. Ed. by José Manuel Ferrández Vicente et al. Cham: Springer International Publishing, 2015, pp. 377–387. ISBN: 978-3-319-18914-7.

[13] J. D. Martínez-Vargas et al. "Estimation of M/EEG Non-stationary Brain Activity Using Spatio-temporal Sparse Constraints." In: *Artificial Computation in Biology and Medicine*. Ed. by José Manuel Ferrández Vicente et al. Cham: Springer International Publishing, 2015, pp. 429–438. ISBN: 978-3-319-18914-7.

[14] Sebastián Castaño-Candamil et al. "Solving the EEG inverse problem based on space–time–frequency structured sparsity constraints." In: *NeuroImage* 118 (2015), pp. 598–612. ISSN: 1053-8119. DOI: https://doi.org/10.1016/j.neuroimage.2015.05.052. URL: http://www.sciencedirect.com/science/article/pii/S1053811915004346.

[15] Karl Friston et al. "Multiple sparse priors for the M/EEG inverse problem." In: *NeuroImage* 39.3 (2008), pp. 1104–1120.

[16] E. Giraldo-Suarez et al. "Reconstruction of Neural Activity from EEG Data Using Dynamic Spatiotemporal Constraints." In: *International Journal of Neural Systems* 26.07 (2016). PMID: 27354190, p. 1650026. DOI: 10.1142/S012906571650026X. eprint: https://www.worldscientific.com/doi/pdf/10.1142/S012906571650026X. URL: https://www.worldscientific.com/doi/abs/10.1142/S012906571650026X.

[17] Makoto Fukushima et al. "MEG source reconstruction based on identification of directed source interactions on whole-brain anatomical networks." In: *NeuroImage* 105 (2015), pp. 408–427. ISSN: 10959572. DOI: 10.1016/j.neuroimage.2014.09.066.

[18] M. Bueno-López et al. "Analysis of neural activity from EEG data based on EMD frequency bands." In: *2017 24th IEEE International Conference on Electronics, Circuits and Systems (ICECS)*. Dec. 2017, pp. 401–405. DOI: 10.1109/ICECS.2017.8292116.

[19] Mansoor Rezghi et al. "A new variant of L-curve for Tikhonov regularization." In: *Journal of Computational and Applied Mathematics* 231.2 (2009), pp. 914–924. ISSN: 0377-0427. DOI: https://doi.org/10.1016/j.cam.2009.05.016. URL: http://www.sciencedirect.com/science/article/pii/S0377042709003215.

[20] Andreas Galka et al. "A solution to the dynamical inverse problem of EEG generation using spatiotemporal Kalman filtering." In: *NeuroImage* 23.2 (2004), pp. 435–453. ISSN: 10538119. DOI: 10.1016/j.neuroimage.2004.02.022.

[21] J. D. López et al. "SINGLE MEG/EEG SOURCE RECONSTRUCTION WITH MULTIPLE SPARSE PRIORS AND VARIABLE PATCHES." en. In: *DYNA* 79 (Aug. 2012), pp. 136–144. ISSN: 0012-7353. URL: http://www.scielo.org.co/scielo.php?script=sci_arttext&pid=S0012-73532012000400018&nrm=iso.

[22] P. Munoz et al. "Time-course reconstruction of neural activity for multiples simultaneous source." In: *IFMBE Proceedings CLAIB 2016*. Vol. 60. Bucaramanga, Colombia: Springer, Oct. 2016, pp. iv/485–iv/488.

[23] J. W. Kim et al. "Compact dynamical model of brain activity." In: *Phys. Rev. E* 75 (3 Mar. 2007), p. 031907. DOI: 10.1103/PhysRevE.75.031907. URL: https://link.aps.org/doi/10.1103/PhysRevE.75.031907.

[24] Pablo Andrés Muñoz-gutiérrez et al. "Localization of Active Brain Sources From EEG Signals Using Empirical Mode Decomposition : A Comparative Study." In: 12.November (2018), pp. 1–14. DOI: 10.3389/fnint.2018.00055.

[25] Maximiliano López et al. "Electroencephalographic Source Localization based on Enhanced Empirical Mode Decomposition." In: *IAENG International Journal of Computer Science* 46 (Apr. 2019), pp. 228–236.

[26] Mussarat Yasmin et al. "Brain image reconstruction: A short survey." In: *World Applied Sciences Journal* 19.1 (2012), pp. 52–62. ISSN: 18184952. DOI: 10.5829/idosi.wasj.2012.19.01.486.

[27] Saman Sarraf et al. "ADVANCES IN FUNCTIONAL BRAIN IMAGING: A COMPREHENSIVE SURVEY FOR ENGINEERS AND PHYSICAL SCIENTISTS." In: *International Journal of Advanced Research* 4 (Aug. 2016), pp. 640–660.

[28] Hans Hallez et al. "Review on solving the forward problem in EEG source analysis." In: *Journal of NeuroEngineering and Rehabilitation* 4 (2007). ISSN: 17430003. DOI: 10.1186/1743-0003-4-46.

[29] Okito Yamashita. "Dynamical EEG Inverse Problem and Causality Analysis of fMRI Data Okito Yamashita." PhD thesis. Japan, 2003.

[30] Anders M. Dale et al. "Improved Localizadon of Cortical Activity by Combining EEG and MEG with MRI Cortical Surface Reconstruction: A Linear Approach." In: *Journal of Cognitive Neuroscience* 5.2 (1993). PMID: 23972151, pp. 162–176. DOI: 10.1162/jocn.1993.5.2.162. eprint: https://doi.org/10.1162/jocn.1993.5.2.162. URL: https://doi.org/10.1162/jocn.1993.5.2.162.

[31] Alexandre Gramfort et al. "Time-Frequency Mixed-Norm Estimates : Sparse M / EEG imaging with non-stationary source activations." In: *Neuroimage* 70 (2013), pp. 410–422.

[32] S. Baillet et al. "A Bayesian approach to introducing anatomo-functional priors in the EEG/MEG inverse problem." In: *IEEE Transactions on Biomedical Engineering* 44.5 (May 1997), pp. 374–385. ISSN: 1558-2531. DOI: 10.1109/10.568913.

[33] M. S. Hämäläinen et al. "Interpreting magnetic fields of the brain: minimum norm estimates." In: *Medical & Biological Engineering & Computing* 32.1 (Jan. 1994), pp. 35–42. ISSN: 1741-0444. DOI: 10.1007/BF02512476. URL: https://doi.org/10.1007/BF02512476.

[34] Roberto Domingo Pascual-Marqui. "Review of Methods for Solving the EEG Inverse Problem." In: *International Journal of Bioelectromagnetism* 1.1 (1999), pp. 75–86. URL: http://www.tut.fi/ijbem.

[35] Mayrim Vega-hern et al. "Penalized least squares methods for solving the EEG inverse problem." In: *Statistica Sinica* 18.4 (2008), pp. 1535–1551. ISSN: 10170405. DOI: 10.2307/24308568.

[36] Sunao Iwaki et al. "Weighted minimum-norm source estimation of magnetoencephalography utilizing the temporal information of the measured data." In: *Journal of Applied Physics* 83 (June 1998), pp. 6441–6443. DOI: 10.1063/1.367732.

[37] Okito Yamashita et al. "Recursive Penalized Least Squares Solution for Dynamical Inverse Problems of EEG Generation." In: *Human Brain Mapping* 21.4 (2004), pp. 221–235. ISSN: 10659471. DOI: 10.1002/hbm.20000.

[38] I.F. Gorodnitsky et al. "Sparse Signal Reconstruction from Limited Data Using FOCUSS: A Re-weighted Minimum Norm Algorithm." In: *Trans. Sig. Proc.* 45.3 (Mar. 1997), pp. 600–616. ISSN: 1053-587X. DOI: 10.1109/78.558475. URL: https://doi.org/10.1109/78.558475.

[39] Christophe Phillips et al. "Anatomically Informed Basis Functions for EEG Source Localization: Combining Functional and Anatomical Constraints." In: *NeuroImage* 16.3, Part A (2002), pp. 678–695. ISSN: 1053-8119. DOI: https://doi.org/10.1006/nimg.2002.1143. URL: http://www.sciencedirect.com/science/article/pii/S1053811902911432.

[40] Christophe Phillips et al. "Systematic Regularization of Linear Inverse Solutions of the EEG Source Localization Problem." In: *NeuroImage* 17.1 (2002), pp. 287–301. ISSN: 1053-8119. DOI: https://doi.org/10.1006/nimg.2002.1175. URL: http://www.sciencedirect.com/science/article/pii/S1053811902911754.

[41] Nelson J. Trujillo-Barreto et al. "Bayesian M/EEG source reconstruction with spatio-temporal priors." In: *NeuroImage* 39.1 (2008), pp. 318–335. ISSN: 1053-8119. DOI: https://doi.org/10.1016/j.neuroimage.2007.07.062. URL: http://www.sciencedirect.com/science/article/pii/S1053811907006921.

[42] Andrés Felipe Soler. "Design of regularized state observer for estimation in large scale systems: source activity reconstruction from EEG signals." MA thesis. Colombia: Universidad Tecnológica de Pereira, 2018.

[43] U. Schmitt et al. "Numerical aspects of spatio-temporal current density reconstruction from EEG-/MEG-data." In: *IEEE Transactions on Medical Imaging* 20.4 (Apr. 2001), pp. 314–324. ISSN: 1558-254X. DOI: 10.1109/42.921480.

[44] M. J. Barton* et al. "Evaluating the Performance of Kalman-Filter-Based EEG Source Localization." In: *IEEE Transactions on Biomedical Engineering* 56.1 (Jan. 2009), pp. 122–136. ISSN: 1558-2531. DOI: 10.1109/TBME.2008.2006022.

[45] Graham C. Goodwin et al. *Adaptive Filtering Prediction and Control*. 2nd. Mineola, NY, USA: Dover Publications, Inc, 2009. ISBN: 978-0-486-46932-4.

[46] Eduardo Giraldo-Suárez et al. "Dynamic Inverse Problem Solution Using a Kalman Filter Smoother for Neuronal Activity Estimation." In: *Tecno Lógicas* 0.27 (2011), pp. 33–51. ISSN: 2256-5337.

[47] Seth B. Agyei et al. "Longitudinal study of preterm and full-term infants: High-density EEG analyses of cortical activity in response to visual motion." In: *Neuropsychologia* 84 (2016), pp. 89–104. ISSN: 0028-3932. DOI: https://doi.org/10.1016/j.neuropsychologia.2016.02.001. URL: http://www.sciencedirect.com/science/article/pii/S0028393216300379.

[48] Antonio Fernandez Guerrero et al. "Brain dynamics during the sleep onset transition: An EEG source localization study." In: *Neurobiology of Sleep and Circadian Rhythms* 6 (2019), pp. 24–34. ISSN: 2451-9944. DOI: https://doi.org/10.1016/j.nbscr.2018.11.001. URL: http://www.sciencedirect.com/science/article/pii/S2451994418300178.

[49] Alessia Bersagliere et al. "Mapping Slow Waves by EEG Topography and Source Localization: Effects of Sleep Deprivation." In: *Brain Topography* 31.2 (2018), pp. 257–269. ISSN: 15736792. DOI: 10.1007/s10548-017-0595-6. URL: http://dx.doi.org/10.1007/s10548-017-0595-6.

[50] Grzegorz M. Wojcik et al. "Mapping the Human Brain in Frequency Band Analysis of Brain Cortex Electroencephalographic Activity for Selected Psychiatric Disorders." In: *Frontiers in Neuroinformatics* 12 (2018), p. 73. ISSN: 1662-5196. DOI: 10.3389/fninf.2018.00073. URL: https://www.frontiersin.org/article/10.3389/fninf.2018.00073.

[51] Stefan Haufe et al. "A Simulation Framework for Benchmarking EEG-Based Brain Connectivity Estimation Methodologies." In: *Brain Topography* (June 2016). ISSN: 1573-6792. DOI: 10.1007/s10548-016-0498-y. URL: https://doi.org/10.1007/s10548-016-0498-y.

[52] Richard Henson et al. "A Parametric Empirical Bayesian Framework for the EEG/MEG Inverse Problem: Generative Models for Multi-Subject and Multi-Modal Integration." In: *Frontiers in Human Neuroscience* 5.76 (2011), pp. 1–16.

[53] Norden E. Huang et al. "The empirical mode decomposition and the Hilbert spectrum for nonlinear and non-stationary time series analysis." In: *Proceedings of the Royal Society of London A: Mathematical, Physical and Engineering Sciences* 454.1971 (1998), pp. 903–995. ISSN: 1364-5021. DOI: 10.1098/rspa.1998.0193.

[54] M. Bueno-Lopez et al. "Understanding Instantaneous frequency detection: A discussion of Hilbert-Huang Transform versus Wavelet Transform." In: *International Work-Conference on Time Series Analysis-ITISE*. Vol. 1. Granada, Spain: University of Granada, Sept. 2017, pp. 474–486.

[55] D. P. Mandic et al. "Empirical Mode Decomposition-Based Time-Frequency Analysis of Multivariate Signals: The Power of Adaptive Data Analysis." In: *IEEE Signal Processing Magazine* 30.6 (Nov. 2013), pp. 74–86. ISSN: 1053-5888.

[56] Maximiliano López et al. “Electroencephalographic Source Localization based on Enhanced Empirical Mode Decomposition.” In: *IAENG International Journal of Computer Science* 46 (Apr. 2019), pp. 228–236.

[57] D. Xu et al. “Optimization in Quaternion Dynamic Systems: Gradient, Hessian, and Learning Algorithms.” In: *IEEE Transactions on Neural Networks and Learning Systems* 27.2 (Feb. 2016), pp. 249–261. ISSN: 2162-237X.

[58] Thomas Y. Hou et al. “Data-driven time-frequency analysis.” In: *Applied and Computational Harmonic Analysis* 35.2 (Sept. 2013), pp. 284–308.

[59] B. Boashash. “Estimating and interpreting the instantaneous frequency of a signal. Part 1: Fundamentals.” In: *Proceedings of the IEEE* 80.4 (Apr. 1992), pp. 520–538. ISSN: 0018-9219.

[60] Zhaohua Wu et al. “Ensemble Empirical Mode Decomposition: A noise-assisted data analysis method.” In: *Advances in Adaptive Data Analysis* 1.1 (2009), pp. 1–41.

[61] R. Deering et al. “The use of a masking signal to improve empirical mode decomposition.” In: *Proceedings. (ICASSP ’05). IEEE International Conference on Acoustics, Speech, and Signal Processing, 2005.* Vol. 4. Mar. 2005, pp. iv/485–iv/488.

[62] Olav Fosso et al. “EMD Mode Mixing Separation of Signals with Close Spectral Proximity in Smart Grids.” In: *IEEE PES ISGT Europe 2018 - 8th IEEE PES Innovative Smart Grid Technologies*. Oct. 2018. DOI: inpress.

[63] G. Rilling et al. “One or Two Frequencies? The Empirical Mode Decomposition Answers.” In: *IEEE Transactions on Signal Processing* 56.1 (Jan. 2008), pp. 85–95. ISSN: 1053-587X. DOI: 10.1109/TSP.2007.906771.

[64] N. Rehman et al. “Multivariate empirical mode decomposition.” In: *Proceedings of the Royal Society A: Mathematical, Physical and Engineering Sciences* 466.2117 (2010), pp. 1291–1302. ISSN: 14712946. DOI: 10.1098/rspa.2009.0502.

[65] Danilo P. Mandic et al. “Empirical mode decomposition-based time-frequency analysis of multivariate signals: The power of adaptive data analysis.” In: *IEEE Signal Processing Magazine* 30.6 (2013), pp. 74–86. ISSN: 10535888. DOI: 10.1109/MSP.2013.2267931.

[66] R N Henson et al. “Electrophysiological and Haemodynamic Correlates of Face Perception , Recognition and Priming.” In: *Cereb. Cortex* 13 (2003), pp. 793–805.

[67] Karl Friston et al. “Bayesian estimation of evoked and induced responses.” In: *Human Brain Mapping* 27.9 (2006), pp. 722–735. ISSN: 10659471. DOI: 10.1002/hbm.20214.

[68] R. N. Henson et al. “Population-level inferences for distributed MEG source localization under multiple constraints: Application to face-evoked fields.” In: *NeuroImage* 38.3 (2007), pp. 422–438. ISSN: 10538119. DOI: 10.1016/j.neuroimage.2007.07.026.

[69] R. N. Henson et al. "Selecting forward models for MEG source-reconstruction using model-evidence." In: *NeuroImage* 46.1 (2009), pp. 168–176. ISSN: 10538119. DOI: 10.1016/j.neuroimage.2009.01.062. URL: http://dx.doi.org/10.1016/j.neuroimage.2009.01.062.

[70] Daniel G. Wakeman et al. "A multi-subject, multi-modal human neuroimaging dataset." In: *Scientific Data* 2 (Jan. 2015). Data Descriptor, pp. 150001–150016. URL: https://doi.org/10.1038/sdata.2015.1.

[71] Yossi Rubner et al. "The Earth Mover's Distance as a Metric for Image Retrieval." In: *International Journal of Computer Vision* 40.2 (Nov. 2000), pp. 99–121. ISSN: 1573-1405. DOI: 10.1023/A:1026543900054. URL: https://doi.org/10.1023/A:1026543900054.

[72] Stefan Haufe et al. "Combining sparsity and rotational invariance in EEG/MEG source reconstruction." In: *NeuroImage* 42.2 (2008), pp. 726–738. ISSN: 1053-8119. DOI: https://doi.org/10.1016/j.neuroimage.2008.04.246. URL: http://www.sciencedirect.com/science/article/pii/S1053811908005144.

[73] Jeffrey C. Lagarias et al. "Convergence Properties of the Nelder-Mead Simplex Method in Low Dimensions." In: *SIAM Journal on Optimization* 9 (1998), pp. 112–147.

[74] Anne Humeau-Heurtier et al. "Refined Multiscale Hilbert-Huang Spectral Entropy and Its Application to Central and Peripheral Cardiovascular Data." In: *IEEE Transactions on Biomedical Engineering* 63.11 (2016), pp. 2405–2415. ISSN: 15582531. DOI: 10.1109/TBME.2016.2533665.

[75] D. Chen et al. "Epileptic Focus Localization Using Discrete Wavelet Transform Based on Interictal Intracranial EEG." In: *IEEE Transactions on Neural Systems and Rehabilitation Engineering* 25.5 (May 2017), pp. 413–425. ISSN: 1534-4320.

[76] S. Gillijns et al. "What is the ensemble Kalman filter and how well does it work?" In: *2006 American Control Conference*. June 2006, pp. 1–6. DOI: 10.1109/ACC.2006.1657419.